ABSTRACT

Title of Thesis:	THE ROLE OF WATER AND STRAIN RATE IN THE DEFORMATION OF LIMESTONE
	William Martin Kibikas (Master of Science), 2017
Thesis Directed By:	Associate Professor Wen-lu Zhu Department of Geology

Fluids are pervasive throughout the Earth's crust. Fluid-rock interaction can significantly alter the mechanical and petrophysical properties of host rocks. This study focuses on the role of fluids in weakening porous carbonate rocks. High solubility of calcite can cause chemically-induced weakening and lead to time-dependent deformation in carbonate rocks. To quantify the effect of hydro-chemo-mechanical coupling on the deformation behavior and failure mode of carbonate rocks, limestone was deformed under both dry and water-saturated conditions. To elucidate the deformation mechanisms, the deformation experiments were conducted at different strain rates. The experimental data shows that while the shear strengths of water-saturated limestone increase with increasing strain rate, the effect of strain rate on the dry samples is negligible. Quantitative microstructural analyses reveal that the grain-scale damage is primarily in forms of stress-induced microcracking and mechanical twinning under both dry and wet conditions. However, with the presence

of water, the extent of intergranular pressure solution increases with increasing confinements. The positive correlation between the extent of intergranular pressure solution and the magnitude of weakening suggests that intergranular pressure solution exerts important controls in time-dependent deformation of carbonate rocks.

THE ROLE OF WATER AND STRAIN RATE IN THE DEFORMATION OF LIMESTONE

by

William Martin Kibikas

Thesis submitted to the Faculty of the Graduate School of the
University of Maryland, College Park, in partial fulfillment
of the requirements for the degree of
Masters of Science
2017

Advisory Committee:
Associate Professor Wen-lu Zhu, Chair
Assistant Professor Vedran Lekic (University of Maryland)
Professor Philip Candela (University of Maryland)

Table of Contents

List of Tables

List of Figures

Figure A.3: Image of Nikon Eclipse LV100n POL petrographic microscope used in this study.

Figure A.4: Total microcracks oriented perpendicular (⊥) to σ_1 and parallel (||) to σ_1. Microcrack incidents are recorded as per mm (mm^{-1}). 1) Undeformed; 2) Hydrostatic; 3) 10 MPa, Dry, $1.5x10^{-5}$ s^{-1}; 4) 30 MPa, Dry, $1.5x10^{-5}$ s^{-1}; 5) 50 MPa, Dry, $1.5x10^{-5}$ s^{-1}; 6) Undeformed; 7) Hydrostatic; 8) 30 MPa, Dry, $1.5x10^{-6}$ s^{-1}; 9) 50 MPa, Dry, $1.5x10^{-6}$ s^{-1}; 10) Undeformed; 11) 10 MPa, Wet, $1.5x10^{-4}$ s^{-1}; 12) 10 MPa, Wet, $1.5x10^{-5}$ s^{-1}; 13) 10 MPa, Wet, $1.5x10^{-6}$ s^{-1}; 14) Undeformed; 15) 30 MPa, Wet, $1.5x10^{-4}$ s^{-1}; 16) 30 MPa, Wet, $1.5x10^{-5}$ s^{-1}; 17) 30 MPa, Wet, $1.5x10^{-6}$ s^{-1}.

Figure A.5: Total grain-grain contacts oriented perpendicular (⊥) to σ1 and parallel (||) to σ_1. Contact incidents are recorded as per mm (mm^{-1}). 1) Undeformed; 2) Hydrostatic; 3) 10 MPa, Dry, $1.5x10^{-5}$ s^{-1}; 4) 30 MPa, Dry, $1.5x10^{-5}$ s^{-1}; 5) 50 MPa, Dry, $1.5x10^{-5}$ s^{-1}; 6) Undeformed; 7) Hydrostatic; 8) 30 MPa, Dry, $1.5x10^{-6}$ s^{-1}; 9) 50 MPa, Dry, $1.5x10^{-6}$ s^{-1}; 10) Undeformed; 11) 10 MPa, Wet, $1.5x10^{-4}$ s^{-1}; 12) 10 MPa, Wet, $1.5x10^{-5}$ s^{-1}; 13) 10 MPa, Wet, $1.5x10^{-6}$ s^{-1}; 14) Undeformed; 15) 30 MPa, Wet, $1.5x10^{-4}$ s^{-1}; 16) 30 MPa, Wet, $1.5x10^{-5}$ s^{-1}; 17) 30 MPa, Wet, $1.5x10^{-6}$ s^{-1}.

Figure A.6: Total pressure solution indentations oriented perpendicular (⊥) to σ1 and parallel (||) to σ_1. Contact incidents are recorded as per mm (mm^{-1}). 1) Undeformed; 2) Hydrostatic; 3) 10 MPa, Dry, $1.5x10^{-5}$ s^{-1}; 4) 30 MPa, Dry, $1.5x10^{-5}$ s^{-1}; 5) 50 MPa, Dry, $1.5x10^{-5}$ s^{-1}; 6) Undeformed; 7) Hydrostatic; 8) 30 MPa, Dry, $1.5x10^{-6}$ s^{-1}; 9) 50 MPa, Dry, $1.5x10^{-6}$ s^{-1}; 10) Undeformed; 11)

Table of Abbreviations

Symbol	Definition
P_E	Effective pressure
P_T	Total pressure
P_P, σ_P	Pore pressure
σ_E	Effective mean stress
σ_T	Total stress
E	Young's modulus
$\sigma_{1,2,3}$	Maximum (1), intermediate (2) and minimum (3) principal stresses
$\varepsilon_{1,2,3}$	Axial (1) and radial (2,3) strains
ν	Poisson's ratio
μ	Coefficient of internal friction
τ	Shear stress
β	Dilatancy factor
ε_v	Volumetric strain
γ	Plastic shear strain
h/E	Hardening modulus
N	Normalcy factor
σ_{ds}	Differential stress
K	Bulk modulus
B	Bulk compressibility
$\dot{\varepsilon}$	Strain rate (change in strain over time)
P^*	Grain-crushing pressure
C^*	Shear-enhanced compaction
C'	Shear-enhanced dilation
$C^{*\prime}$	Transition from shear-enhanced compaction to dilatation
II	Parallel to σ_1
$\perp$	Perpendicular to σ_1
P_L^{II}	Cracks oriented parallel to the maximum principal stress
$P_L^{\perp}$	Cracks oriented perpendicular to the maximum principal stress
C	Total grain-contact incidents
PS	Incidents of pressure solution indentation
σ_{sd}	Standard deviation
N_T	Number of variables measured
x_i	Individual measurements
m_P	Mean porosity
S_V	Total crack surface area in a given volume measured

Chapter 1: Introduction

1.1: Motivation

Carbonate rocks are a major component of the upper crust. Their mechanical behavior during interaction with fluids is critical to a number of energy and environmental applications. They are known to host 60% of recoverable petroleum resources (e.g. *Roehl and Choquette, 2012*) and large amounts of accessible freshwater (e.g. *LaMoreaux et al., 1984*). Carbonate reservoirs are also one of the largest potential sources of geothermal energy generation (e.g. *Goldscheider et al., 2010*). Additionally, carbonate rocks are seen as a potential sink for carbon dioxide through geologic sequestration (*Parry, 2007*; *Benson and Cole, 2008*). Thus it is important to understand their deformation response at various mechanical and chemical conditions.

Fluids play an important role in the elastic and inelastic behavior of carbonate rocks through mechanical effects such as changes in the effective stress applied to the rock (*Baud et al., 2000b*) or chemical effects such as mineral alteration (*Wintsch et al., 1995*) and stress corrosion processes such as enhanced subcritical cracking and pressure solution (*Atkinson and Meredith, 1981*; *Rutter, 1986*). Generally, mechanical effects of rock-fluid interaction play a greater role in controlling the hydromechanical stress response of a rock (*Teufel et al., 1991*). However, the chemical effects of fluids cannot be discounted for certain minerals that are more chemically active (*Grgic and Giraud, 2014*).

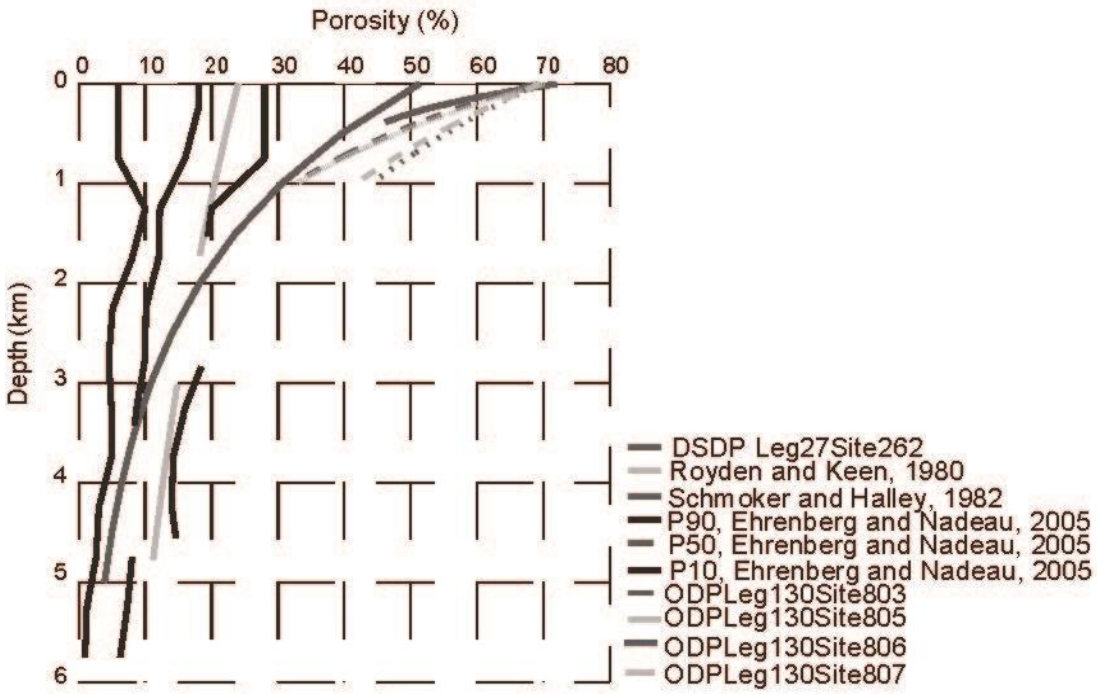

Figure 1.1: Compaction observed in different carbonate reservoirs. It can be seen that the initial porosity can vary significantly at shallow depths. Additionally, the compaction trends vary noticeably, with some following a quasi-linear trend of porosity loss with depth, while others experience an exponential decrease in porosity with increase in depth. Curves for DSDP leg 27 from *Hamilton (1976)*, and for ODP Leg 130 from *Bassinot et al. (1993)*. Image adapted from *Croizé et al. (2013)*.

Various field and laboratory observations have demonstrated that fluid chemistry has a significant effect on porous carbonate response to deformation (*Croizé et al., 2013*). While other porous rocks tend to follow a exponential trend of increasing compaction and porosity reduction with greater depth, carbonate rocks display a wide variety of compaction trends and behavior. Porous carbonate rocks have shown a strong sensitivity to pore fluid chemistry, which can significantly alter response to mechanical loading (*Rutter, 1974*; *Risnes et al., 2005*; *Lisabeth and Zhu, 2015*). Observations of fluid injection and removal from carbonate reservoirs indicate that their rock-fluid interaction introduces several mechanical and chemical weakening mechanisms. One example of this would be the Ekofisk chalk in the North Sea, where injection of water to increase hydrocarbon production and halt reservoir

compaction led to an unexpected increase of reservoir compaction and subsidence (*Teufel et al., 1991*). This compaction rate was observed to decrease over time (*Guilbot and Smith, 2002*), suggesting that the chemical dissolution was enhancing the deformation observed. The chemical and mechanical deformation appear to be highly coupled in carbonate rocks, such that enhanced deformation occurs when both processes occur simultaneously.

Reservoir stability over large time scales is an important consideration for any potential injection or extraction projects. Unexpected compaction of reservoirs can lead to severe financial and environmental consequences such as induced seismicity (*Simpson et al., 1988*; *Majer et al., 2007*), well failure (*Bruno, 1992; Fredrich et al., 2000)*, and surface subsidence (*De Waal and Smits, 1988*). A better understanding of the deformation of porous carbonate rocks under mechanical and chemical loading is needed.

1.2: Background

Although their mechanical behavior is qualitatively similar, porous carbonate rocks vary in a number of ways from other porous rocks. For instance, crystal plasticity such as mechanical twinning can be activated at low temperatures in carbonate rocks (*Turner et al., 1954*). They are also more sensitive to their chemical environment, as calcite is fairly soluble in the presence of water or carbon dioxide rich fluids (*Garrels and Christ, 1965*).

1.2.1: Porosity and Pore Pressure

The in-situ stress experienced by porous sedimentary rocks under hydrothermal conditions is affected by pore pressure. It is well understood for rocks that an increase in pore pressure lowers the effective pressure of a rock (*Terzaghi, 1936*) represented by the equation:

$$P_E = P_T - P_P \tag{1.1}$$

where the P_E is the effective pressure, P_T is the overburden pressure, and P_P is the pore pressure.

Stress is an analogous quantity to pressure, defines the traction applied for a given orientation. The law of effective stress can then be written as:

$$\sigma_E = \sigma_T - P_P \tag{1.2}$$

σ_E represents the effective stress, σ_T and P_P represent the total stress and pore pressure of the rock, respectively. As is the convention for rock mechanics, positive stress indicates compaction and negative stress indicates extension in this work.

Porosity has a number of effects on the behavior on carbonate rocks during deformation. The yielding strength of a rock (or effective mean stress where the behavior becomes inelastic) is inversely related to its initial porosity (*Byerlee, 1968*; *Hirth and Tullis, 1989*; *Wong et al., 1992*; *Wong et al., 1997*; *Vajdova et al., 2004*).

1.2.2: Elastic and Plastic Behavior

Porous carbonate rocks experience both elastic and plastic deformation under increasing mechanical load. Elastic deformation implies that all deformation that has occurred is recoverable. The elastic portion of strain is generally small compared to the inelastic strain of a rock during deformation. Elasticity of a rock can be

characterized by the elastic or Young's modulus (E) and the Poisson's ratio (v). Under conventional triaxial loading, with constant radial stress $\sigma_2 = \sigma_3$ (intermediate and minimum principal stresses respectively), the Young's modulus E is the slope of the differential stress-axial strain curve during the linear elastic portion of deformations where the incremental change in differential stress is divided by the incremental change of axial strain. It can be written as:

$$E = \frac{d(\sigma_1 - \sigma_3)}{d\varepsilon_1} \tag{1.3}$$

Poisson's ratio is the negative ratio of the change in transverse or radial strain ($d\varepsilon_3$) per the change in axial strain ($d\varepsilon_1$) during differential loading:

$$v = -\frac{d\varepsilon_3}{d\varepsilon_1} \tag{1.4}$$

It relates the axial and radial strains, defining the relationship between the material shortening and outward bulging.

The inelastic strain is the plastic or non-recoverable strain accumulated once a rock has reached its elastic limit. Mechanisms for plastic strain during rock deformation include but are not limited to Hertzian fracturing at grain boundaries, grain boundary rotation, and inelastic pore collapse (*Wong et al., 1997*, *Baud et al., 2000a*).

The model developed by *Rudnicki and Rice (1975)* outlined a number of constitutive inelastic properties that can be used to describe the inelastic behavior of a dilatant material. These variables are the coefficient of internal friction μ, the dilatancy factor β, and the hardening modulus $\frac{h}{E}$. The coefficient of internal friction is defined as:

$$\mu = \frac{d\tau}{d\sigma} \tag{1.5}$$

where τ is the shear stress and σ is the effective normal stress; it describes the frictional behavior along microcracks that occurs during plastic yielding. The dilatancy factor β is formally defined as:

$$\beta = \frac{d\varepsilon_V}{d\gamma} \tag{1.6}$$

and is the change in volumetric strain $d\varepsilon_V$ divided by the shear strain $d\gamma$ that occurs following the onset of inelastic deformation. It represents the tendency of a rock to dilate or increase in volume with increasing inelastic strain (see *Rummel, 1982*). The third quantity is the hardening modulus, defined as:

$$\frac{h}{E} = \frac{(\mu - \beta)^2}{18(1 - v)} - \frac{1}{36}(\beta + \mu + 3N)^2 \tag{1.7}$$

where N relates the load geometry of the material, which for axisymmetric loading is $\frac{1}{\sqrt{3}}$, and the other variables are defined above. The hardening modulus is the amount of hardening the sample exhibits post-yield.

1.2.3: Brittle-Ductile Deformation

The inelastic deformation of a porous carbonate rock can be described as either brittle or ductile (*Byerlee, 1968*; *Rutter, 1986*). Brittle deformation in rocks is predominantly controlled by the opening of microcracks oriented subparallel to the greatest principal stress (*Brace et al., 1966*; *Byerlee, 1968*; *Fredrich et al., 1989*), which results in dilation or an overall increase in volume. At higher confining pressures, the opening of microcracks is suppressed and ductile deformation occurs

(*Paterson and Wong, 2005*). Ductile deformation occurs through intracrystalline plasticity, inelastic pore collapse, and distributed micro-cracking (*Rutter, 1986; Fredrich et al., 1989*; *Paterson and Wong, 2005*), and results in compaction or an overall decrease in volume. Brittle and ductile behaviors are not mutually exclusive, and a transitional behavior exists where compaction occurs initially before dilatancy and volumetric increase occurs (*Wong et al., 1997*). This behavior is referred to as semibrittle (*Rutter, 1986*; *Evans et al., 1990*; *Nicolas et al., 2016*) and will be encountered in in this study.

The transition from brittle dilatant behavior to ductile compactive behavior is sensitive to changes in porosity, chemical environment, and temperature (*Heard, 1960*; *Fredrich et al., 1989*; *Hirth and Tullis, 1994*; *Wong and Baud, 2012*). Previous research with limestones (*Rutter, 1972*, *Rutter, 1974*; *Yale and Crawford, 1998*; *Vajdova et al., 2004, 2012*; *Baud et al., 2009*) has found that initial porosity is also inversely related to the transition from brittle to ductile behavior. For carbonate rocks, this transition from brittle to ductile behavior requires significantly lower confining pressures and temperatures, since carbonate minerals such as calcite require lower shear stresses than other common crustal minerals (such as quartz or feldspar) to induce crystal plasticity (*Barber and Wenk, 1979*). Whether dilatancy or compaction occurs is important for predictions of the stability of a porous carbonate rocks at a given condition (*Wong and Baud, 1999*).

1.2.4: Fluid-Induced Mechanical Weakening

The presence of aqueous fluids generally lowers the overall strength of a rock compared to dry materials (*Griggs, 1967*; *Carter et al., 1990*; *Wong, 2000*). This

weakening is attributed to either mechanical effects such as pore pressure increase and resulting embrittlement (*Paterson and Wong, 2005*) or chemical effects such as enhanced sub-critical cracking and intergranular pressure solution (*Rutter, 1983*; *Atkinson and Meredith, 1987*; *Brantut et al., 2014b*). These mechanical and chemical effects are strongly coupled during porous rock deformation, such that the dominant mechanism of deformation is sensitive to the individual mineral solubility (*Risnes et al., 2005*; *Liteanu et al., 2012*; *David et al., 2015*). The chemical effects of fluid-rock interaction can play a significant role in the behavior of carbonate rocks. Carbonate minerals are sensitive to the pH, salinity, and CO_2 content of a fluid. They have relatively fast reaction rates when in the presence of fluids (*Plummer et al., 1978, Plummer and Busenberg, 1982*; *Sjöberg and Rickard, 1983*; *Pokrovsky et al., 2005*). This implies that the chemistry of the aqueous fluid interacting with the rock may contribute to the deformation behavior. The most common carbonate mineral is calcite, and it is the main component of limestone in this study. The fluid/rock reactions occurring at the surface of calcite can be written as:

$$CaCO_3 + 2H^+ \leftrightarrow Ca^{2+} + H_2CO_3 \quad (1.8)$$

$$CaCO_3 + H_2CO_3 \leftrightarrow Ca^{2+} + 2HCO_3^- \quad (1.9)$$

$$CaCO_3 \leftrightarrow Ca^{2+} + CO_3^{2-} \quad (1.10)$$

The equations for calcite dissolution in a saturated environment are taken from *Plummer et al. (1978)*. This study focuses on the dissolution of calcite, but these formulae can be applied to other carbonate species (see *Pokrovsky et al., 2002*).

The dissolution of calcite in a chemically active environment is primarily driven by the H^+ content (pH) of the fluid (Equation 1.8), the temperature during reaction, and the calcite surface area able to react. The dissolution of calcite acts as a buffer for the fluid, decreasing the hydrogen ion content as the fluid approaches equilibrium with the reacting calcite surface. As hydrogen content of a reacting fluid increases, both the degree and rate of calcite dissolution increase (*Plummer et al., 1978*). The average fluid pH will rise and the rate of dissolution will decrease. Most sedimentary rocks in the crust have pore fluids with pH values in the range of 5-9 (*Hanor, 1994*). At a neutral pH, the dominant chemical reaction occurring in calcite-rich rock is Equation 1.9, and the dissolution of calcite is fairly low, limited more by available calcite surface area rather than the rate of chemical reaction (*Plummer et al., 1978*).Therefore the effect of chemical solubility on the behavior of carbonate rocks is strictly time-dependent, and likely decreases as the fluid approaches chemical equilibrium with the reacting calcite surface (*Zhang and Spiers, 2005*). However, if deformation is not solely dependent on the chemical potential of the reacting pore fluid, then the chemical effect of a reacting fluid on the deformation response of carbonate rocks can be significant (*Rutter, 1972*; *1983*; *Risnes et al., 2005; Carpenter et al. 2016*).

1.2.5: Deformation Micromechanisms

The primary mechanisms for deformation in porous carbonate rocks are microcracking, mechanical twinning, and pressure-enhanced dissolution (*Fredrich et al., 1989*; *Vajdova et al., 2004*; *Lisabeth and Zhu, 2015*; *Nicolas et al., 2016*). It is important to note that these mechanisms are not mutually exclusive, and can occur simultaneously during deformation in carbonate rocks (*Liteanu et al., 2012*).

Subcritical Cracking

Subcritical cracking occurs when cracks propagate slower than the speed of sound and below the nominal failure stress (*Atkinson, 1984*). Continued crack growth during deformation can eventually lead to crack coalescence and macroscopic failure. Subcritical crack growth occurs progressively during deformation, with a preferred orientation to crack growth occurring in the brittle deformation regime. Under ductile deformation conditions, no preferred crack orientation is generally exhibited. In porous carbonate rocks, microcracks display a preferential orientation parallel to the maximum compressive stress. With increasing confinement, the anisotropy of crack orientation decreases (*Wu et al., 2000*).

Stress corrosion cracking (SCC) is subcritical crack growth that is enhanced by the presence of chemically active fluids (*Atkinson and Meredith, 1981*; *Brantut et al., 2013, 2014b*). The presence of fluids is known to reduce the stress required to nucleate and propagate subcritical cracks (*Røyne et al., 2011*). *Atkinson (1984)* suggested that the increased chemical potential at crack tips due to elastic stress concentration may lead to enhanced crack tip dissolution and thus drive crack propagation. However, this process is highly sensitive to the fluid chemistry, as the

pH, water activity, and presence of salts can significantly affect dissolution and therefore subcritical crack growth. This suggests that the effect of fluids on crack propagation should decrease as the pore fluid continues to reach chemical equilibrium in carbonate rocks.

Mechanical Twinning

Intracrystalline plasticity can occur at low temperatures and pressures in carbonate rocks, with the most common form being crystal twinning (*Barber and Wenk, 1979*; *Rowe and Rutter, 1990*; *Burkhard, 1993*). Twinning occurs easily in carbonate minerals because only low shear stresses are needed to facilitate intracrystalline plasticity (see Figure 1.2) (*Turner et al., 1954*). Due to the ease of nucleating twins, they serve as a means of accommodating inelastic strain in carbonate rocks at conditions that cannot induce crystal plasticity in other porous rocks. However, the role fluids play in twin nucleation and propagation observed in carbonate rocks is still not well understood, and needs to be further constrained.

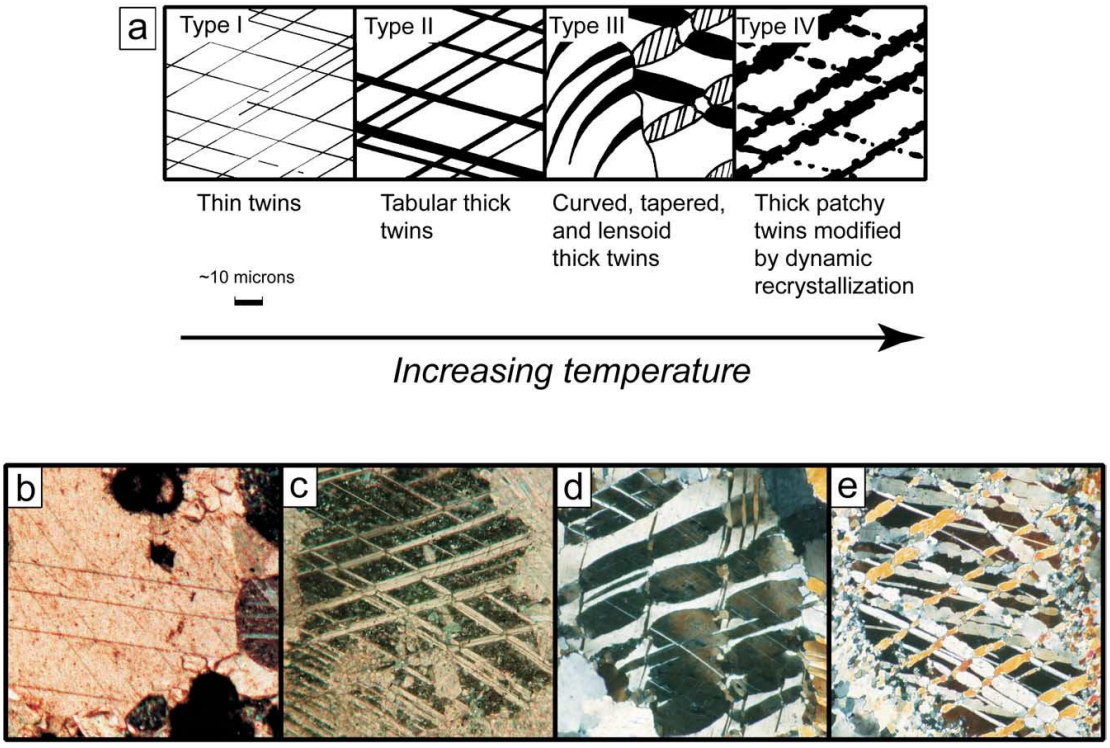

Figure 1.2: Schematic of evolution in calcite twin morphology at higher temperatures, adapted from *Burkhard (1993)* method of classification. a) Shows the different classifications of twin morphology and how they develop with increasing temperature. b-e) Natural examples of the twin types found in several marbles and thrust faults. Images taken from *Ferrill et al. (2004)*.

Intergranular Pressure Solution

Intergranular pressure solution (IPS) is a process that involves the dissolution and re-precipitation of minerals at grain boundaries under applied normal stress (*Rutter and Elliot, 1976*; *Rutter, 1983*; *Zhang and Spiers, 2005, 2010*). In a chemically active environment, stress applied to grain boundaries in contact with one another creates a heightened dissolution at the stressed contact. This leads to three serial processes: a removal by dissolution of the grains in contact, followed by a diffusion away from the higher stress regions and re-precipitation at lower stress regions (*Rutter, 1976*; *Tada et al., 1987*). The rate of pressure solution is controlled

by the slowest of the three processes, i.e. dissolution, diffusion, or re-precipitation. Dissolution, diffusion and re-precipitation are driven by the chemical potential gradient existing between the liquid at the stressed grain contact and that in the pore space (*Croizé et al., 2010*).

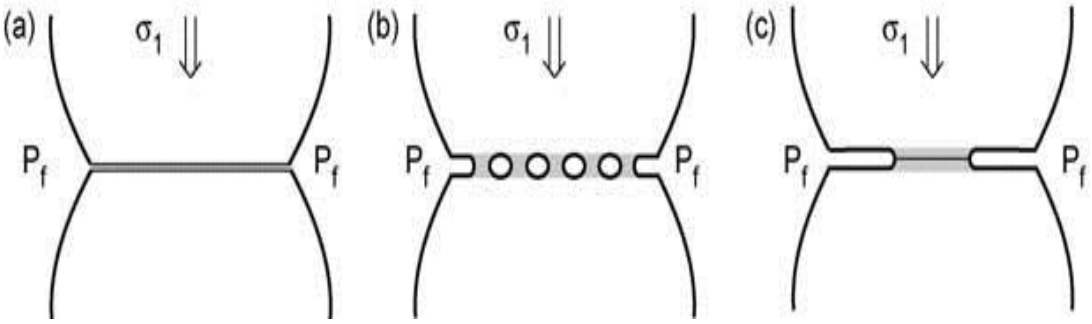

Figure 1.3: Three proposed mechanisms of intergranular pressure solution. a) Thin-film model; b) Channel-island model; c) Free-faced plastic deformation model. Image from *Le Guen et al. (2007).*

Three primary models have been proposed for pressure solution at grain boundaries: the “thin-film" model (*Weyl, 1959*; *Rutter and Elliot, 1976*; *Rutter, 1983*) (Figure 1.3a), the “channel-island" model (*Spiers et al., 1990*; *Lehner, 1995*) (Figure 1.3b), and the “free-face plastic deformation" model (*Tada et al., 1987*) (Figure 1.3c). The “thin-film" model proposes that a thin film of fluid lies between the entire grain contact surface under stress. The fluid allows for the diffusion of material throughout the entire grain contact away from the area under stress. The “channel-island" model proposes that the grain contact is a series of separate islands where heightened stress concentrations promote dissolution and where the gaps or channels allow for diffusion between and away from the contact surface. The “free-face plastic deformation" model proposes a continuous grain boundary without a fluid film. Dissolution of the grain contact in the pore fluid causes undercutting of the contact zone until a threshold diameter is reached and the contact collapses either by plastic

flow or brittle failure. It is worth noting that these models are not mutually exclusive and may all be occurring simultaneously during deformation (*Le Guen et al., 2007*; *Liteanu et al., 2012*).

Given the high solubility of carbonate minerals and common occurrence of fluids in the upper crust, pressure solution is considered a significant compaction mechanism in porous carbonate rocks (*Wanless, 1979*; *Rutter, 1983*; *Hellmann et al., 2002*). Various microstructures observed in carbonate rocks such as sutured grain contacts, truncated grains, and stylolites have been attributed to pressure solution processes (*Wanless, 1979*). In addition, the grain boundary dissolution that occurs through pressure solution indentation is not dependent on the saturation state of the reacting fluid, and will continue even as calcite solubility decreases (*Zhang and Spiers, 2005*).

1.2.6: Time-Dependent Compaction

Strain rate is a measure of the rate of differential mechanical loading. In nature, strain rates as low as 10^{-14} s^{-1} (associated with tectonic loading) and as fast as 10^{3} s^{-1} (during earthquakes) can be observed. At rapid strain rates and nominally dry conditions, rock strength is essentially time-independent (*Paterson and Wong, 2005*). However, fluids are ubiquitous throughout the upper crust, and most regional strain rates are quite slow. At these conditions, which are common for porous carbonate rocks, deformation behavior can be time-dependent (i.e. the rate of loading affects the compaction) (*Rutter 1972*; *Croizé et al., 2013*; *Brantut et al., 2013, 2014a*).

Rock–fluid interaction plays a significant role in the time-dependent rock deformation of porous rocks. First, changes in permeability can cause a rapid increase

or decrease in the local effective stress by locally reducing or elevating the pore pressure, respectively (*Rutter, 1972*, *Brantut et al., 2014a*). Under rapid mechanical loading, the rock compacts or dilates more quickly than for slower loading, and a phenomenon called dilatancy softening or hardening can occur. In the case of compaction, the fluid may not be able to escape the pore spaces quickly enough and will raise the pore pressure, which lowers the effective pressure on the rock (see Equations 2.1 and 2.2). In contrast, rapid dilation can lead to an increase in the effective stress as the pore pressure is lowered (*Rutter, 1972*). This is particularly important for carbonate rocks, given the greater heterogeneity of their pore structure and permeability compared to other porous rocks.

Second, the kinetics of chemical reactions operate at different rates than the rate of mechanical loading (*Pokrovsky et al., 2005*). In most porous rocks, this is relatively insignificant because of their slow reaction kinetics (*Brantley, 2003*; *Brantut et al., 2014a*). However, carbonate minerals react over relatively short time scales, and this can lead to rapid deformation in conjunction with mechanical loading. SCC and IPS require both mechanical and chemical loading to occur (*Hellmann et al., 2002*; *Brantut et al., 2014a*; *Lisabeth and Zhu, 2015*). This coupled hydro-chemo-mechanical deformation in porous carbonate rocks implies chemical deformation influences the rate of mechanical deformation. However, the rate of chemical deformation is more difficult to predict since local stress concentrations, pore fluid, temperature, grain size, and pore geometry each affect the observed loading response.

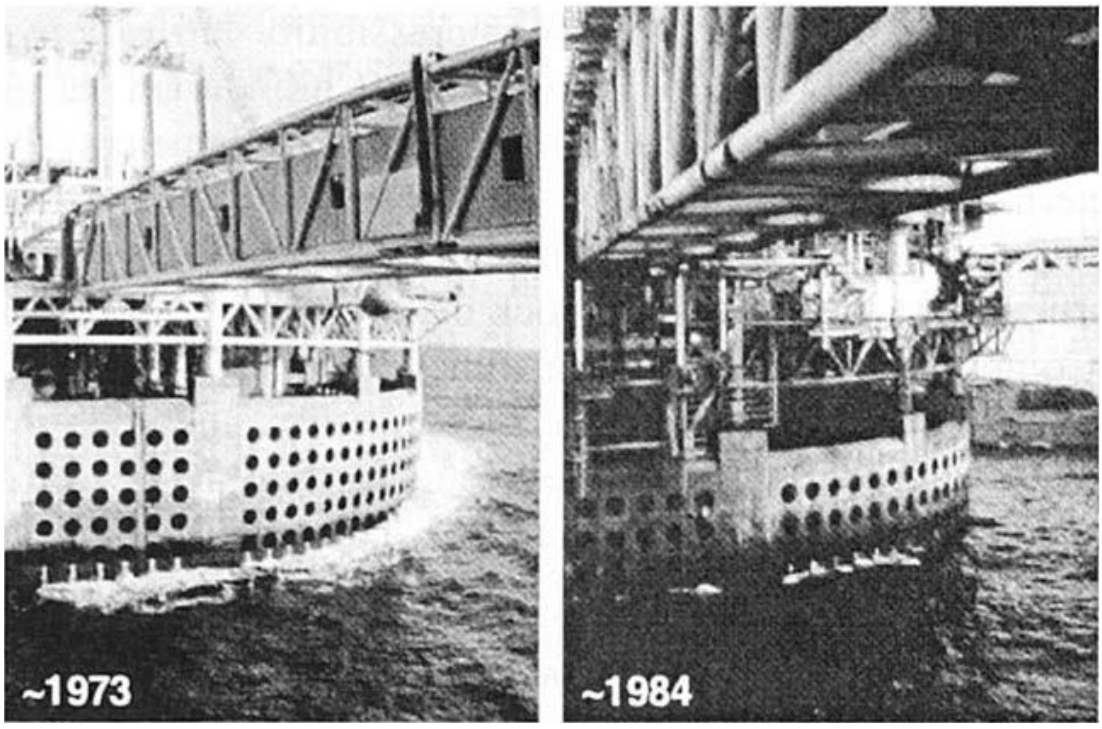

Figure 1.4: Photo showing reservoir compaction in of an offshore platform above the Ekofisk chalk. Water line provides a good indicator for the overall subsidence over the 10 year period of seawater injection. Photo taken from *Nagel (2001)*.

This coupled hydro-chemo-mechanical weakening in carbonate rocks can facilitate additional compaction in reservoir rock beyond deformation due to mechanical load (*Croizé et al., 2013*). One example is that of the Ekofisk oil field in the North Sea, where seawater was injected into a porous chalk formation in order to halt reservoir compaction and increase hydrocarbon production by increasing the in-situ pore pressure (*Teufel et al., 1991*). Following seawater injection, the reservoir compacted an additional 10 meters. This suggests that the compaction in Ekofisk chalk was not only controlled by the pore pressure, but also the chemical environment (*Teufel et al., 1991*; *Risnes, 2001*). Experimental evidence also supports this enhanced weakening in porous carbonate rocks (*Hellmann et al., 2002*; *Liteanu et al., 2012, 2013*; *Lisabeth and Zhu, 2015*). *Hellmann et al. (2002)* found that strain rates

increased dramatically in chalk samples saturated with saline water instead of pure water. *Le Guen et al. (2007)* found that in limestone and calcite-cemented sandstone, deformation in the presence of water and supercritical CO_2 caused an increase in the strain rate immediately following fluid injection. It was also seen that deformation in a chemically active environment was primarily accommodated by dissolution-assisted compaction in porous carbonate rocks, with pore collapse observed dominantly at the points of fluid injection (*Le Guen et al., 2007*). Recent work by *Lisabeth and Zhu (2015)* showed pore fluid equilibration with calcite in porous limestone can significantly affect the carbonate rock strength. This corroborates that the rate of calcite dissolution and pore fluid content has a strong impact on overall deformation behavior in porous carbonate rocks.

1.3: Research Aims

This work looks at the deformation mechanisms of limestone under different mechanical and chemical loading conditions. Since the rate of mechanical and chemical loading each have an effect on the observed deformation response, both are varied. For mechanical loading, confining pressure was varied and three different strain rates were applied ($1.5x10^{-4}$, $1.5x10^{-5}$ and $1.5x10^{-6}$ s^{-1}), while hydrostatic deformations are conducted at strain rates of $6x10^{-5}$ s^{-1} and $6x10^{-6}$ s^{-1}. For chemical loading, samples were saturated with deionized water (not in equilibrium with rock). This work will allow a systematic comparison of limestone deformation under various conditions and to quantify the role confining pressure, strain rate, and chemical solubility play.

Quantitative analysis of the microstructures of deformed limestone were conducted on thin sections prepared from deformed Indiana limestone samples. Microstructural analysis yields information on the specific role microcracking, calcite twinning, and pressure solution play in the deformation of limestone at different pressure, strain rate, and fluid conditions. These observations allow for a connection between the experimental observations and the physical micromechanisms accommodating carbonate rock deformation. Combining experimental observations with microstructural analysis allows for a quantification of limestone behavior at different conditions, and potential predictions of the role carbonate petrophysical properties play in deformation.

Chapter 2: Effect of Water, Confining Pressure, and Strain Rate on Mechanical Behavior of Limestone: Deformation Tests

2.1: Experiment Preparation

2.1.1: Indiana Limestone and Northern Israel Limestone

Indiana limestone is a calcium-carbonate rich rock of Mississippian age, composed of >98% calcite, with around 1% accessory minerals such as oxides minerals and clays (*Handbook, 1998*). The limestone is predominately composed of allochmechmical clasts between 200 and 2000 μm aligned subparallel to bedding (*Churcher et al., 1991*) (Figure 2.1). The pore spaces are partially filled with a sparry calcitic cement. Porosity is divided between large intergranular pore spaces surrounded by sparry cement, and smaller intragranular and intracrystalline pore spaces (*Vajdova et al., 2004*; *Zhu et al., 2010*). It is classified as an oolitic grainstone using the Dunham classification for carbonate rocks (*Dunham, 1962).* Blocks of Indiana limestone from Bedford, Indiana were cored perpendicular to bedding and ground into cylinders of length 50.8 mm and diameter 25.4 mm (2 inch by 1 inch).

Limestone samples from a reservoir in northern Israel of Jurassic age are also evaluated here. The high heat flux in this region has led to consideration of the sedimentary rocks there for potential geothermal energy production (*Shalev et al., 2013*). The limestone is dominated by a micrite matrix, with scattered fossiliferous grains. It is classified as a bioclastic wackestone according to the Dunham classification (*Dunham, 1962*)(Figure 2.1). Samples are cored perpendicular to

bedding and ground into cylinders of length 38.1 mm and diameter 18.4 mm (1.5 inch by 0.725 inch).

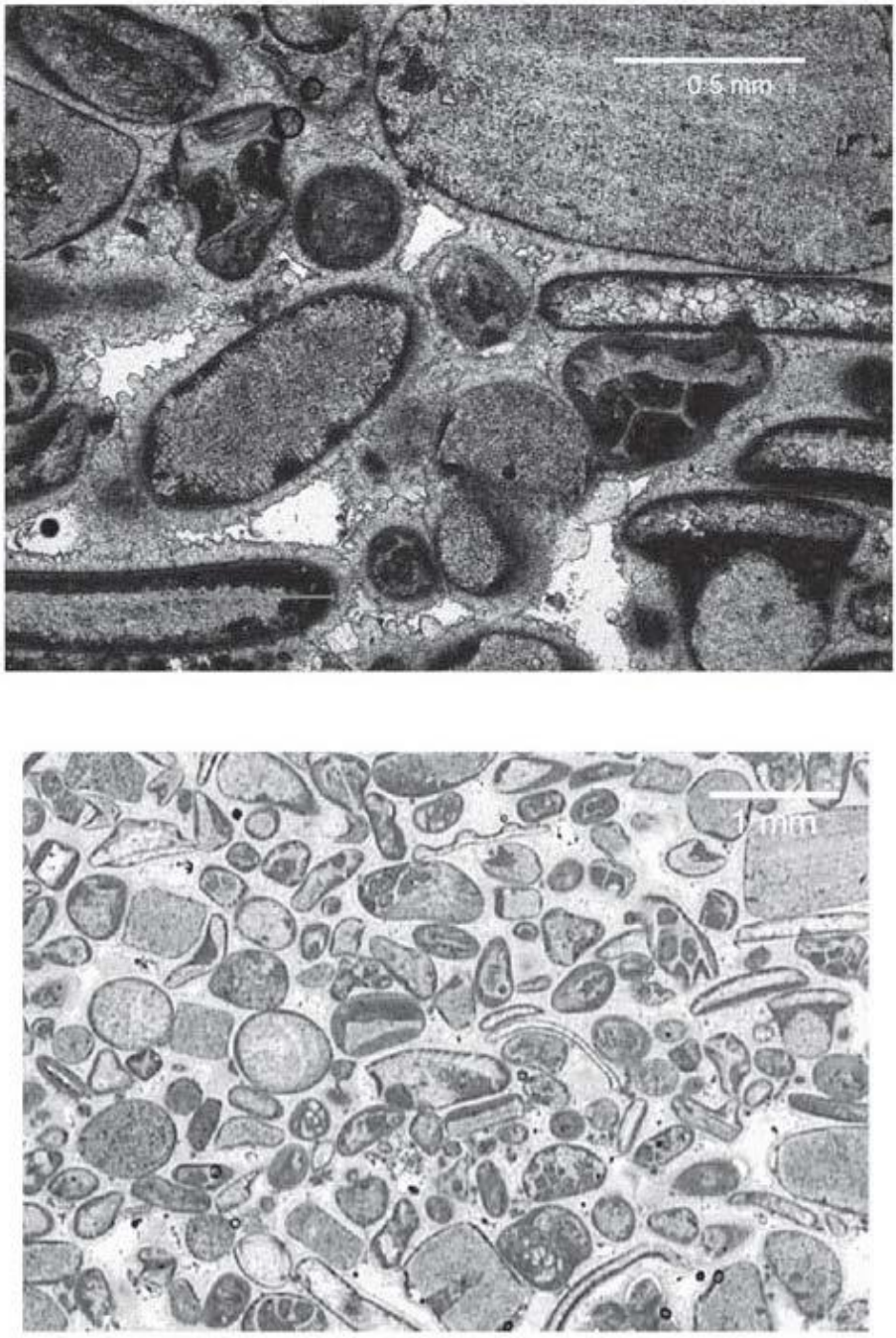

Figure 2.1: Micrographs of undeformed Indiana limestone. Grains are predominantly allochemical clasts >30 μm in diameter. Calcitic cement and large pore spaces can be seen between the individual subrounded grains in the top image. The bottom image shows little deformation occurring in the undeformed rock. Grain sizes and shapes show a wide distribution, though most grains are round or elliptical in shape. Images from *Zhu et al. (2010).*

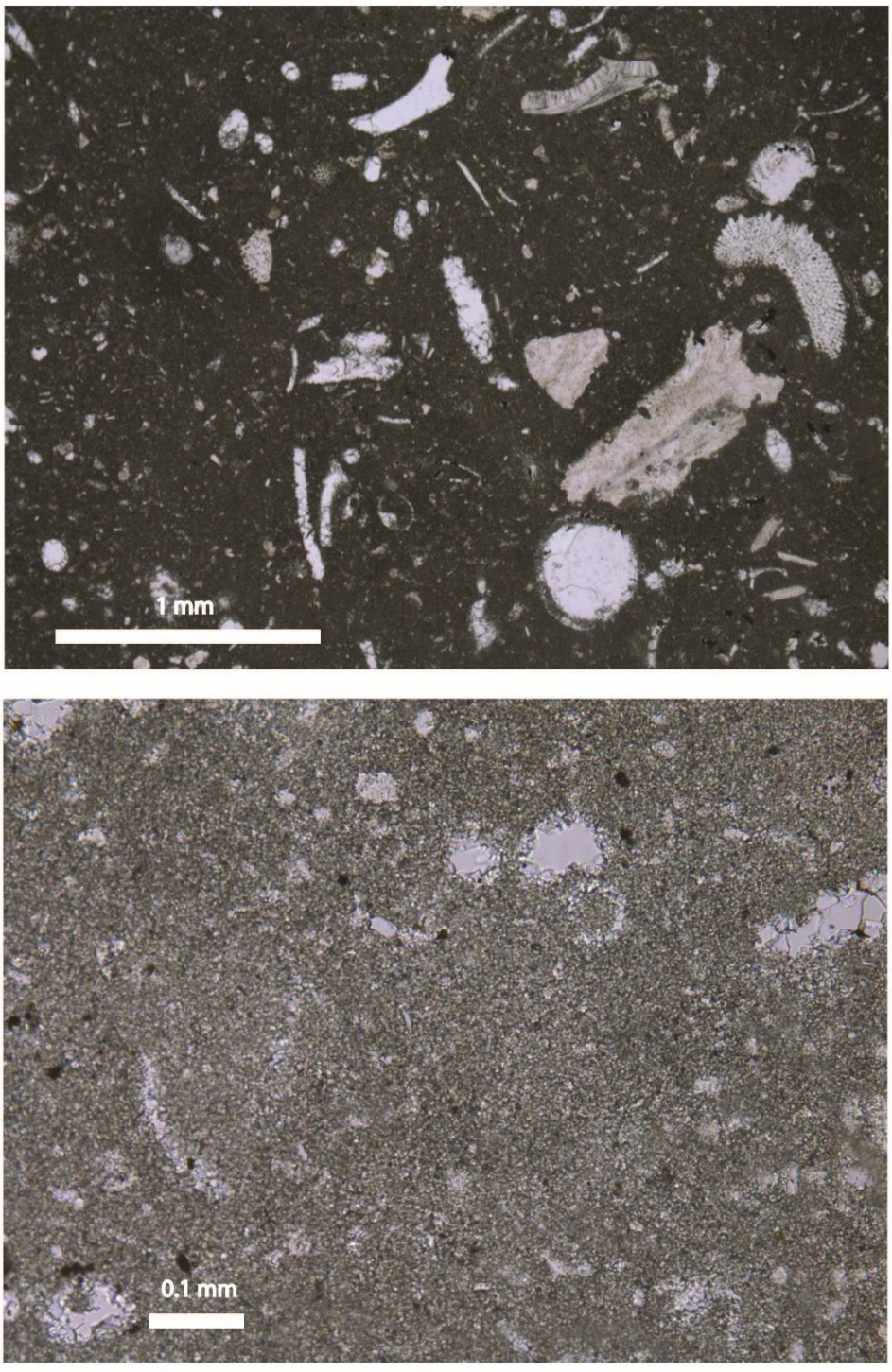

Figure 2.2: Micrographs of undeformed limestone from northern Israel. Top image (taken at 5X magnification) shows the rock is predominantly a fine grain carbonate matrix with larger angular fossils scattered throughout. Bottom image (taken at 20X magnification) shows that the carbonate matrix is extremely fine, with average grain diameters below the limit of resolution. Pore spaces dominantly are seen in micritic matrix.

2.1.2: Porosity Measurement

Initial porosity is an important parameter that controls the observed mode of failure of limestones (*Wong et al., 1997*). Porosity values of all samples were calculated using a comparison of the dry and water-saturated volumes and masses of each sample. Indiana limestone samples were found to have an average porosity 16.0%, similar to values found in *Lisabeth and Zhu (2015)* for Indiana limestone. Porosity was primarily divided between larger pore spaces between grains and smaller micropores located in the oolitic grains. The Israeli limestone was found to be less porous by comparison, with an average initial porosity of ~1.6%. Porosity of the Israeli limestone was primarily found in the micritic matrix, with relatively little occupying the fossiliferous grains.

2.1.3: Sample Jacketing and Preparation

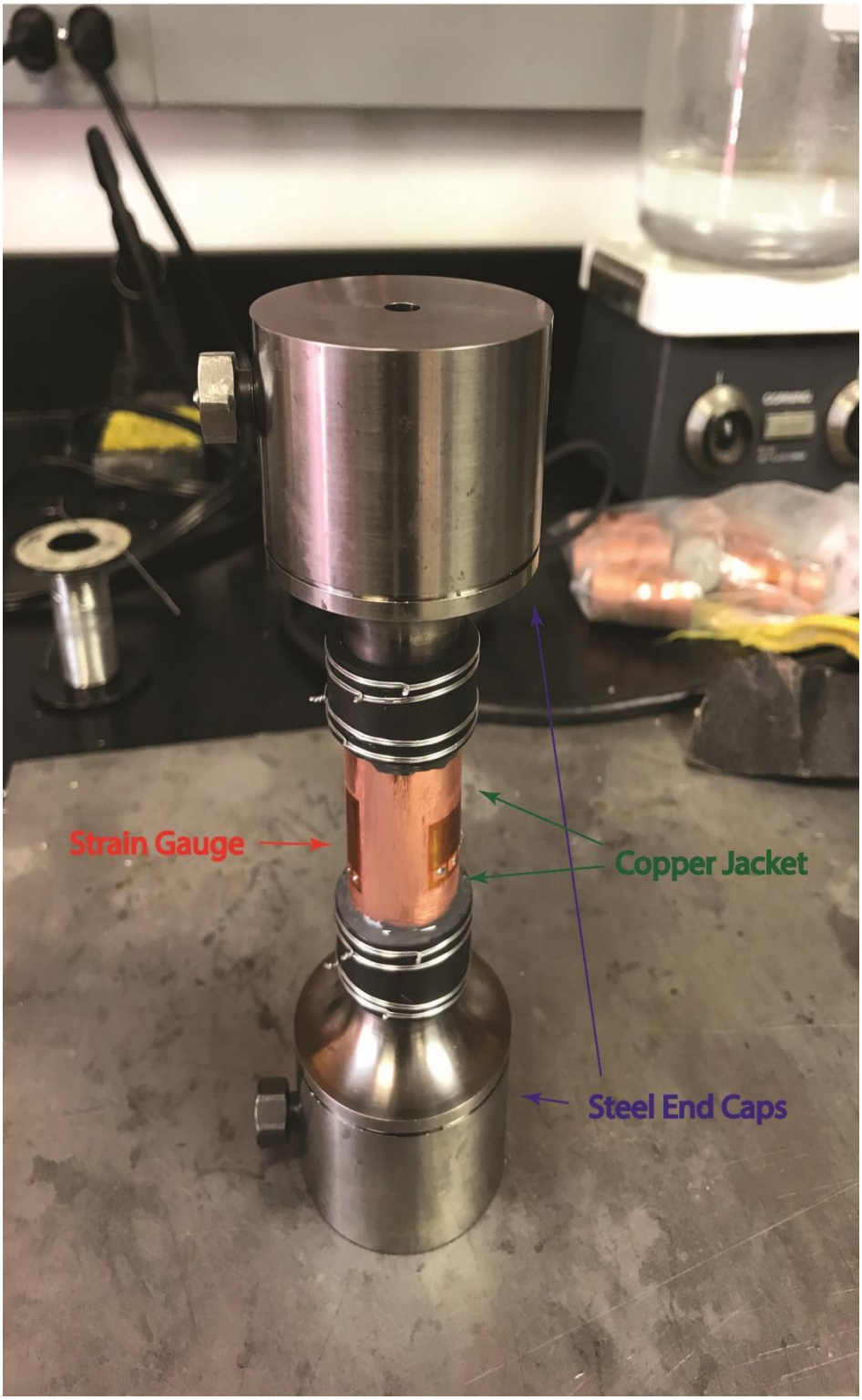

Figure 2.3: Experimental setup for deformation experiments. Limestone sample is between the two end-caps and sealed with the copper jacket.

Indiana limestone samples were first saturated with deionized water for 24 hours using a vacuum saturation method. The Israeli limestone samples were saturated for 48 hours prior to loading to ensure complete fluid saturation. Once saturated masses and volumes were measured, dry deformation samples were then re-dried for 24 hours, while the water-saturated deformations were not re-dried. Samples were jacketed with a copper of 127 μm thicknesses. Following this the samples were sealed with heat-shrink tubing and placed in the deformation apparatus. After seating the jacket to the sample at 5 MPa, three electrical resistance strain gages were then placed on the jacket: two oriented length wise to measure axial strain and one oriented laterally to measure radial strain (Figure 2.3). Samples were then placed between the two end-caps and sealed with polyolefin tubing and steel tie-wires to isolate the samples from the confining medium. Pore tubes were placed at the bottom end-cap of each sample during the pore fluid experiments to allow control of pore pressure (Figure 2.4).

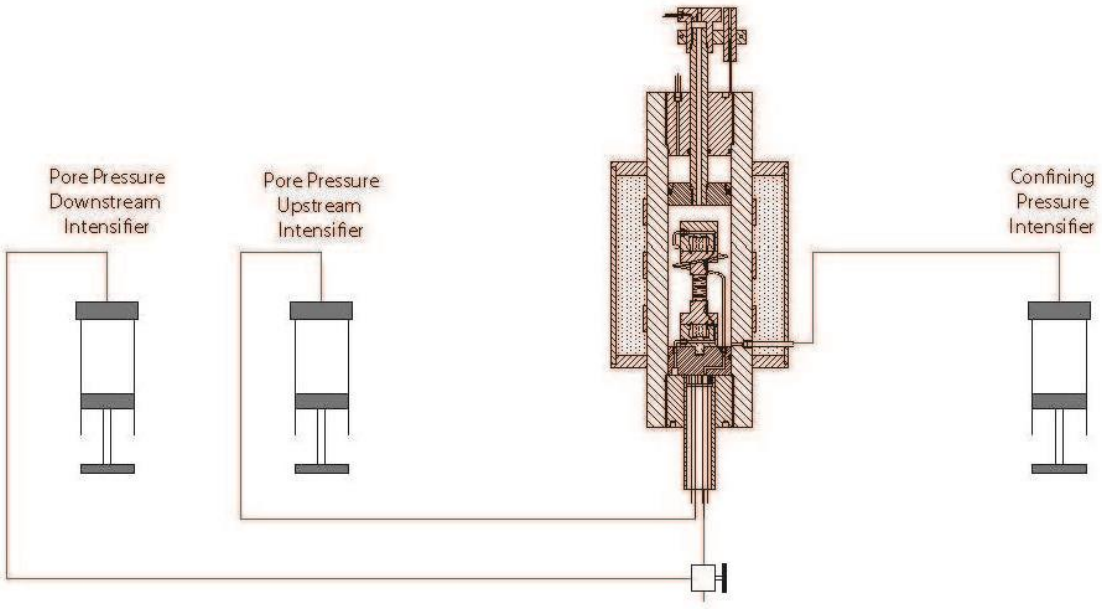

Figure 2.4: Model of the pore system for fluid system in the AutoLab 1500. Separate fluid systems control the confining, differential, and pore pressure.

2.2: Experimental Procedures

2.2.1: Dry Deformation Experiments

All experiments were conducted at room temperature. A hydrostatic experiment was first performed to characterize the loading behavior of dried Indiana limestone and find the P* value, or the pressure at which inelastic pore collapse begins (*Zhang et al., 1990*). Dried samples are jacketed and loaded into the pressure vessel. A small confining pressure (3 MPa) is then added to the sample, and the confining pressure is hydrostatically loaded at a rate of 2 MPa/min (equivalent to an axial strain rate of $6x10^{-5}$ s^{-1} for Indiana limestone) to around ~125 MPa.

Axial deformation experiments with constant axial displacement were conducted on dried Indiana limestone afterwards. Samples were jacketed, inserted into the pressure vessel, and then loaded to the effective confining pressures used. Experiments were conducted at 10, 30, and 50 MPa confining pressures and axially

deformed with strain rates of $1.5x10^{-5}$ s^{-1} and $1.5x10^{-6}$ s^{-1}. The variation in strain rate allows for analysis of the effect of strain rate.

2.2.2: Water-Saturated Deformation Experiments

Water saturated Indiana and Israeli limestone samples were inserted into the pressure vessel and loaded to a small confining pressure (3 MPa). Then, deionized water was added to the system and the pore pressure of the sample was raised to 1 MPa. Trapped air was then vacuumed from the pore system, after which the sample was loaded to the specific experimental conditions.

Water saturated Indiana limestone samples were deformed under both hydrostatic and axial conditions. The axial deformation experiments were conducted with effective confining pressures of 10 and 30 MPa. A pore pressure of 10 MPa was applied to all samples. To compare the time-dependent behavior of the saturated experiments, strain rates of $1.5x10^{-4}$, $1.5x10^{-5}$, and $1.5x10^{-6}$ s^{-1} were used during the axial experiments. Additionally, two water saturated hydrostatic deformations were conducted. This was made in order to determine if time-dependent deformation could occur under purely hydrostatic loading conditions in porous carbonate rocks. These deformations were conducted at rates of $6x10^{-5}$ and $6x10^{-6}$ s^{-1}, which were calculated from the rate of axial strain per second during the elastic portion of the hydrostatic loading.

For the Israeli limestone, a water-saturated hydrostatic deformation was conducted first. Once the hydrostatic loading behavior was quantified, the effective pressures used for the axial deformation experiments were determined. Axial

deformations were conducted using strain rates of $1.5x10^{-5}$ s^{-1} with effective pressures of 30 and 70 MPa.

2.2.3: Data Processing

Data points during experiments were collected every 0.1 second for $1.5x10^{-4}$ s^{-1} axial deformations and every 2 seconds for all hydrostatic deformations, as well as all the $1.5x10^{-5}$ s^{-1} and $1.5x10^{-6}$ s^{-1} strain rate axial deformations. Volumetric strains were calculated using the relation for axisymmetric samples:

$$\varepsilon_v = 2 * \varepsilon_3 + \varepsilon_1 \tag{2.1}$$

where ε_v is the volumetric strain and ε_1 and ε_3 are the radial and axial strains.

The bulk modulus (K), or the resistance of a material to compression, was calculated by dividing the change in effective mean stress by the change in volumetric strain:

$$K = \frac{d\sigma_E}{d\varepsilon_v} \tag{2.2}$$

where σ_v is the volumetric strain and σ_E is the effective stress. The linear portion of the hydrostatic deformation can be used to calculate the bulk modulus prior to the onset of grain breakage and pore collapse. The inverse of this is referred to as the compressibility (B) and be used when discussing the hydrostatic deformations.

Effective mean stress was calculated using the relation:

$$\sigma_e = \frac{\sigma_1 + \sigma_2 + \sigma_3}{3} - P_P \tag{2.3}$$

with σ_1, σ_2, and σ_3 as the principal stresses applied and P_P as the pore pressure. The differential stress, σ_{ds}, was calculated as the difference between the maximum principal stress and the minimum principal stress:

$$\sigma_{ds} = \sigma_1 - \sigma_3 \tag{2.4}$$

Experiment Name	σ_e	σ_p	$\dot{e}$	K	E	ν	C* (σ_{ms})	C* (σ_{ds})	τ* (σ_{ds})	σ_{ds} at 1% Strain	β	μ	h/E_{min}
Name	MPa	MPa	s^{-1}	GPa	GPa	-	MPa	MPa	MPa	MPa	-	-	-
IndLs9-6	H	-	6×10^{-5}	19.2	-	-	-	-		-	-	-	-
IndLs9-5	10	-	1.5×10^{-5}	-	18.4	0.21	14	12	6.928203	39.5381	-0.81	-0.0218	7.794228634
IndLs8-24	30	-	1.5×10^{-5}	-	17.4	0.22	33.5	10.5	6.062178	56.6098	0.31	-0.1427	6.92820323
IndLs9-4	50	-	1.5×10^{-5}	-	15.9	0.22	51.3	3.9	2.251666	60.2273	0.72	-0.24996	2.25166605
IndLs8-20	10	-	1.5×10^{-6}	-	20.01	0.22	14.5	13.5	7.794229	42.7747	-1.3	-0.0226	5.715767665
IndLs8-21	30	-	1.5×10^{-6}	-	18.9	0.25	32.5	7.5	4.330127	59.0215	0.16	-0.1014	5.196152423
IndLs8-19	50	-	1.5×10^{-6}	-	15.5	0.17	50.8	2.4	1.385641	51.977	0.6	-0.1726	1.385640646
IndLs9-21	H	10	6×10^{-5}	19.5	-	-	-	-	-	-	-	-	-
IndLs9-19	H	10	6×10^{-6}	18.9	-	-	-	-	-	-	-	-	-
IndLs9-12	10	10	1.5×10^{-4}	-	20.03	0.21	12.5	7.5	4.330127	43.3459	-1.6	0.2646	5.196152423
IndLs9-13	10	10	1.5×10^{-5}	-	22.7	0.22	14.5	13.5	7.794229	41.8862	-1.1	0.01992	4.849742261
IndLs9-9	10	10	1.5×10^{-6}	-	18.1	0.22	12	6	3.464102	37.1264	-1.2	-0.0489	3.464101615
IndLs9-14	30	10	1.5×10^{-4}	-	27.2	0.24	35	15	8.660254	54.3886	0.06	-0.33516	4.5033321
IndLs9-15	30	10	1.5×10^{-5}	-	19.1	0.19	32.4	7.2	4.156922	45.7575	0.1	-0.21822	2.944486373
IndLs9-16	30	10	1.5×10^{-6}	-	17.2	0.12	31.8	5.4	3.117691	47.2807	0.42	-0.1325	1.732050808
IsrLs_Wet_Hydrostatic	H	10	-	64.2	-	-	-	-	-	-	-	-	-
IsrLs_Wet_30MPa	30	10	1.5×10^{-5}	-	103.9	0.0224	-	-	-	-	-	-	-
IsrLs_Wet_70MPa	70	10	1.5×10^{-5}	-	55	0.0332	-	-	-	-	-	-	-

Table 2.1: Experiment names and list of elastic and plastic parameters of Indiana and Israeli limestones. σ_e = effective confining pressure, σ_p = pore pressure, è = strain rate, K = bulk modulus, E = Young's modulus, ν = Poisson's ratio, C* = onset of shear-enhanced compaction, σ_{ds} at 1% Strain = differential stress at 1% axial strain, β = dilatancy factor, μ = internal coefficient of friction, h/E_{min} = hardening modulus.

Subsection 1: Hydrostatic Indiana Limestone Deformations

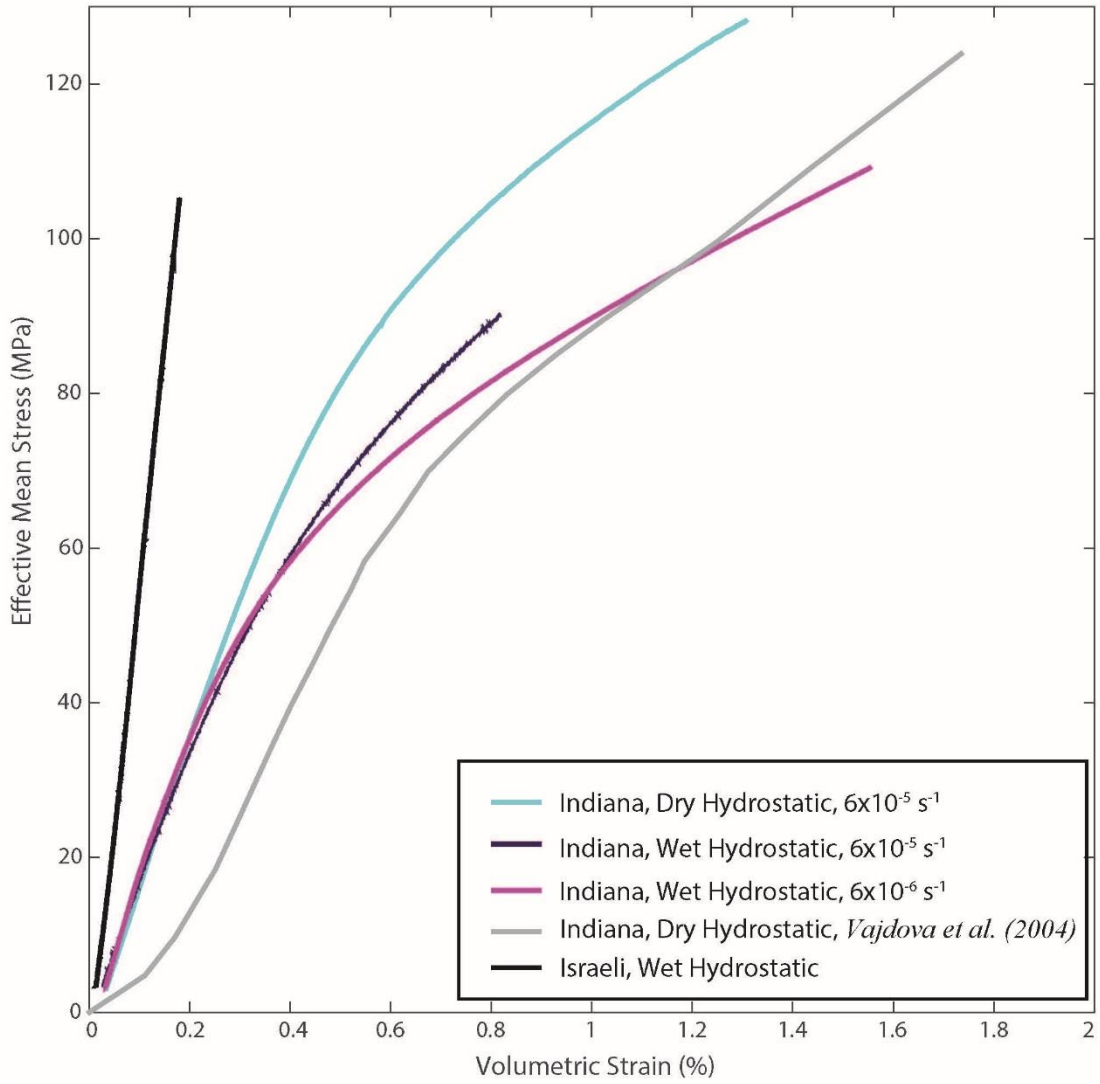

Figure 2.5: Mechanical data for hydrostatic compaction conducted on each limestone, under both dry and water-saturated conditions. Dry data from *Vajdova et al. (2004)* also plotted for comparison.

Mechanical data from all hydrostatic deformation experiments of Indiana and Israeli limestone are plotted in Figure 2.5. All Indiana limestone samples follow a general trend of linearly increasing strain with increased stress, followed by a nonlinear period where the rate of compaction changes with increased effective pressure. The point where behavior deviates from the linear trend of compaction

marks the onset of pore collapse and the breakdown of grains. This is referred to here as the P* or grain-crushing pressure (*Zhang et al., 1990*).

The dry hydrostat shows similar behavior to previously reported deformations with Indiana limestone reported in *Vajdova et al. (2004)* (shown in Figure 2.5). Data for hydrostatic compaction these and of other limestones with different porosities are reported in Table 3.1. The P* value of the dry hydrostatic deformation found here and in *Vajdova et al. (2004)* (~60 MPa) were found to be of similar values, indicating a general similarity in the deformation of dry Indiana limestone. The dry and water saturated Indiana limestone show similar linear trends of compaction prior to the onset of pore collapse (similar bulk moduli (K)). However, the grain crushing pressure P* is significantly lower when Indiana limestone is saturated with water.

The Israeli limestone had a significantly greater bulk modulus compared to the all the Indiana limestone samples (Table 2.1). The P* value was unable to be determined, as it did not occur within the range of confining pressures obtainable by the deformation apparatus.

Subsection 2: Axial Deformation of Indiana Limestone Dry and Water Saturated Deformations

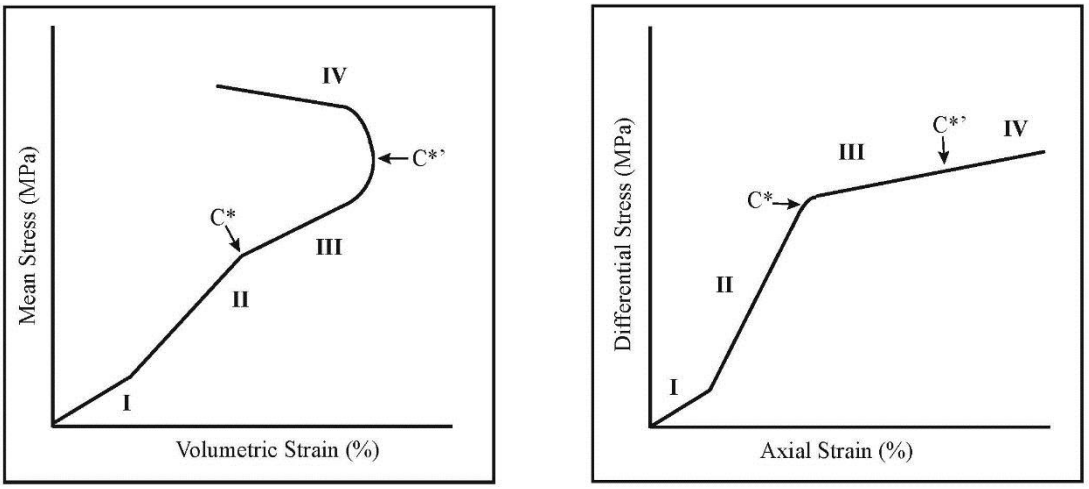

Figure 2.6: Depictions of the transition through stages I-IV and the transition from shear-enhanced compaction (C*) to shear-enhanced dilation (C*'). Volumetric and axial strain plot models adapted *Wawersik and Brace (1971).*

Deformation behavior of porous rocks can generally be separated into four stages (*Wawersik and Brace 1971*). Nonlinear shortening with decreasing compliance (I), followed by a period of linear shortening (II), and a second nonlinear stage with increasing apparent compliance during which the rock may or may not reach a peak stress (III), followed by strain softening or hardening (IV) (Figure 2.6). These stages correspond to (I) pre-existing crack closure, (II) elastic or recoverable deformation, (III) initiation of plastic deformation such as microcracking and crystal plasticity, and (IV) overall rock failure and stress drop.

With the onset of inelastic deformation during axial deformation, porous rocks may either exhibit shear-enhanced compaction (marked by C*) or shear-enhanced dilation (marked by C*') (nomenclature adapted from *Wong et al., 1997*). When the rock experiences a rapid decrease in volumetric strain (marked by C'), the degree of dilation or crack opening is greater than the degree of compaction and the sample

deforms through localized brittle faulting. When the rock experiences a rapid increase in volumetric strain (marked by C*), the degree of compaction or pore collapse is greater than the degree of crack opening and deformation occurs primarily through distributed cataclastic flow (*Wong et al., 1997*). Eventually compaction of the rock transitions from shear-enhanced compaction to shear-enhanced dilation as localized microcracking becomes dominant, the transition is referred to as C*' (*Baud et al., 2000a*).

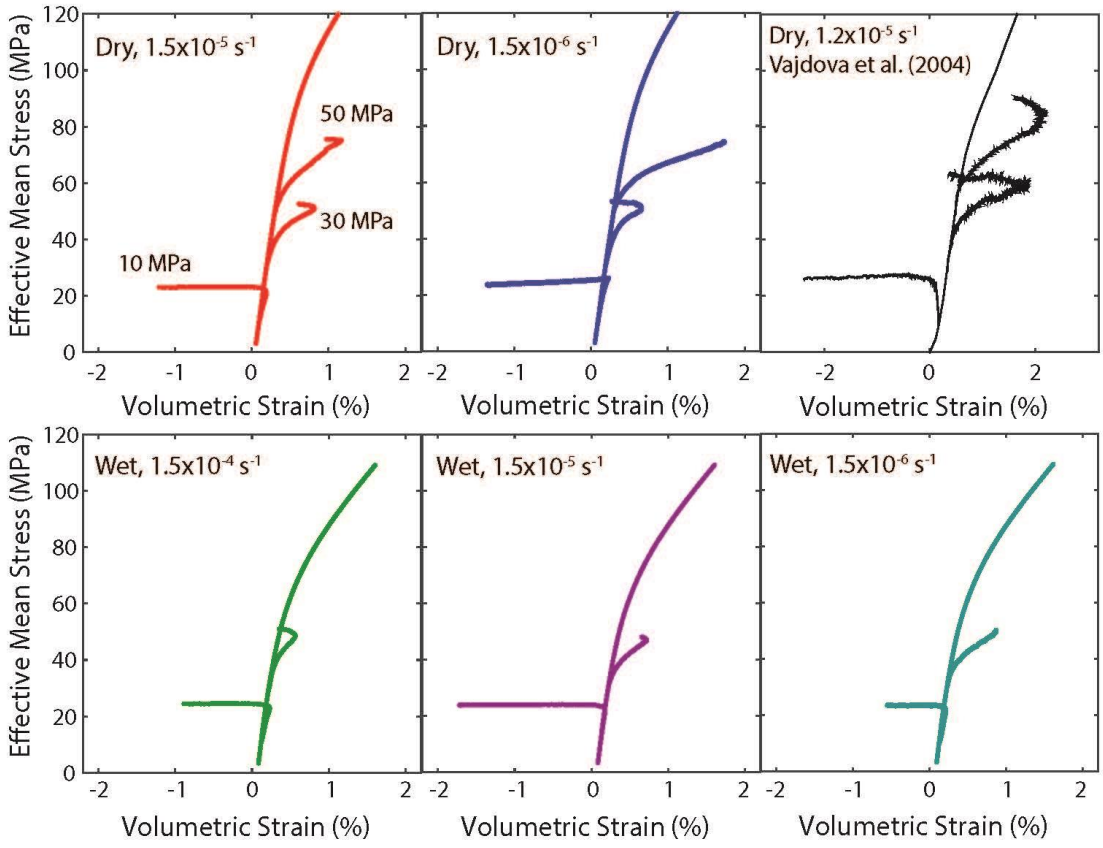

Figure 2.7: Mechanical data for volumetric strain of all Indiana limestone experiments, both hydrostatic and axial deformation experiments. Data from *Vajdova et al. (2004)* plotted in black.

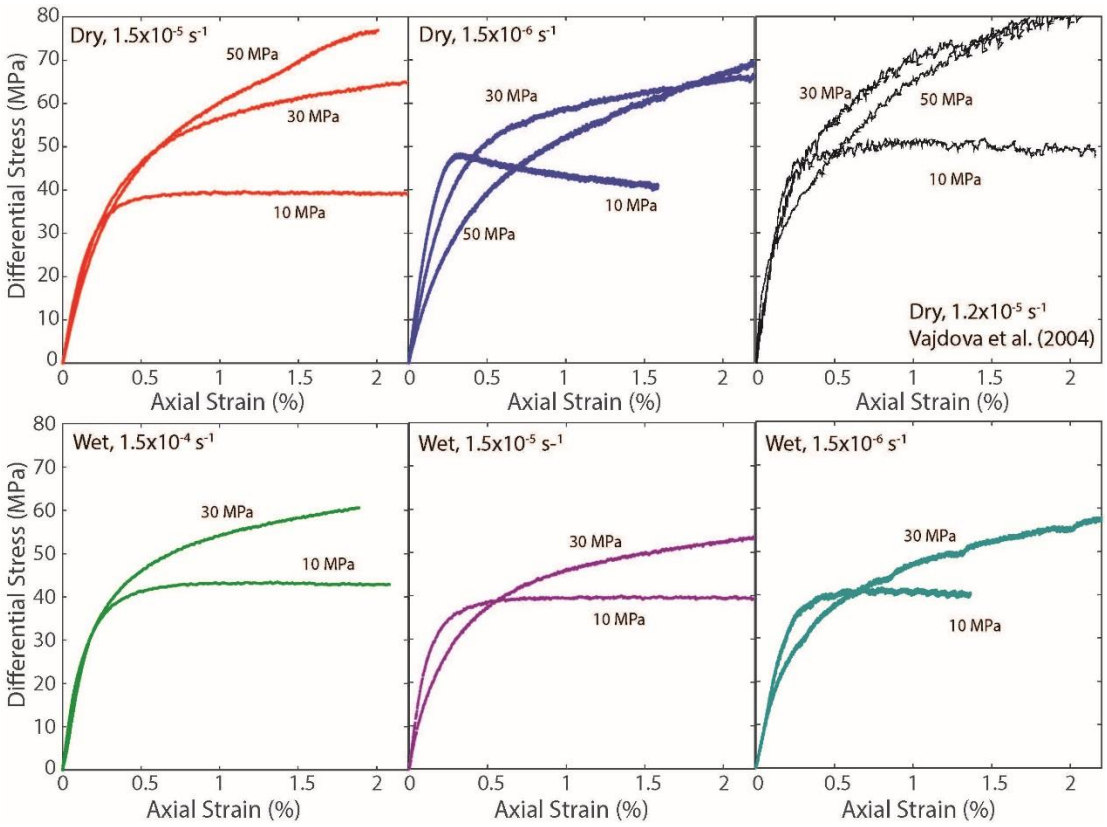

Figure 2.8: Axial deformation data for volumetric strain of all Indiana limestone experiments. Data from *Vajdova et al. (2004)* plotted in black.

The volumetric strains for all Indiana limestone deformations are plotted in Figure 2.7 against the effective mean stress (σ_e). At low confining pressure, all the limestones experienced a shift from inelastic compaction (C*) before quickly transitioning to rapid dilation (C*') as the opening of microcracks becomes dominant. At moderate to higher pressures, all the limestones tested experienced shear-enhanced compaction quickly following the application differential stress. At 30 MPa, samples at all conditions experienced a brief period of shear-enhanced compaction before transitioning to shear-enhanced dilation. As confining pressure was increased further, the inelastic compaction prior to the onset of dilatancy also increased.

The differential stress as a function of axial strain for all axial deformations is plotted in Figure 2.8. With the exception of the dry sample deformed with a strain

rate of $1.5x10^{-6}$ s^{-1}, at a confining pressure of 10 MPa all samples experienced negligible amounts of strain softening. For the exception, a peak differential stress was achieved before the onset of strain softening, though no localized failure was observed post-deformation. As confining pressure was increased on each limestone, the degree of strain hardening increased and plastic deformation was achieved at progressively lower differential stresses. Though variation exists between the differential stresses experienced at each condition tested, no changes in the specific mode of failure behavior were observed at any of the conditions tested.

2.4: Discussion

Indiana limestone deformed axially in this study did not experience localized brittle failure at any of the conditions. In order to quantify the plastic properties of the limestone as the fluid, pressure and strain rate conditions vary, the yield-cap model developed by *Rudnicki (2004)* for a primarily compactant material was used here. Normally shear stress is inferred from the maximum differential stress experienced before brittle failure occurs (*Jaeger, 1960*). Here the failure envelope is defined in shear stress-normal stress space. The stress is inferred from the point at which the volumetric strain first deviates from the hydrostat during axial deformation (in this case C*). Shear stress in this model is inferred as:

$$\tau^* = \frac{\sigma_1 - \sigma_3}{N} \tag{2.5}$$

where $\sigma_1 - \sigma_3$ is the differential stress and τ^* is the shear stress at the onset of shear-enhanced compaction (C*). *N* is the normalcy factor, which in the case of

axisymmetric samples is $\frac{1}{\sqrt{3}}$ (*Rudnicki and Rice, 1975*). The slope of the yield surface here can be inferred as the coefficient of friction. The dilatancy factor following the onset of shear-enhanced compaction (referred to here as β) can be found from the tangent of the deformation behavior in shear strain-volumetric strain space once slope has become quasi-linear. With the coefficient of friction and the dilatancy factor, the hardening modulus can be used to describe the plastic behavior during inelastic deformation.

2.4.1: Effect of Pressure

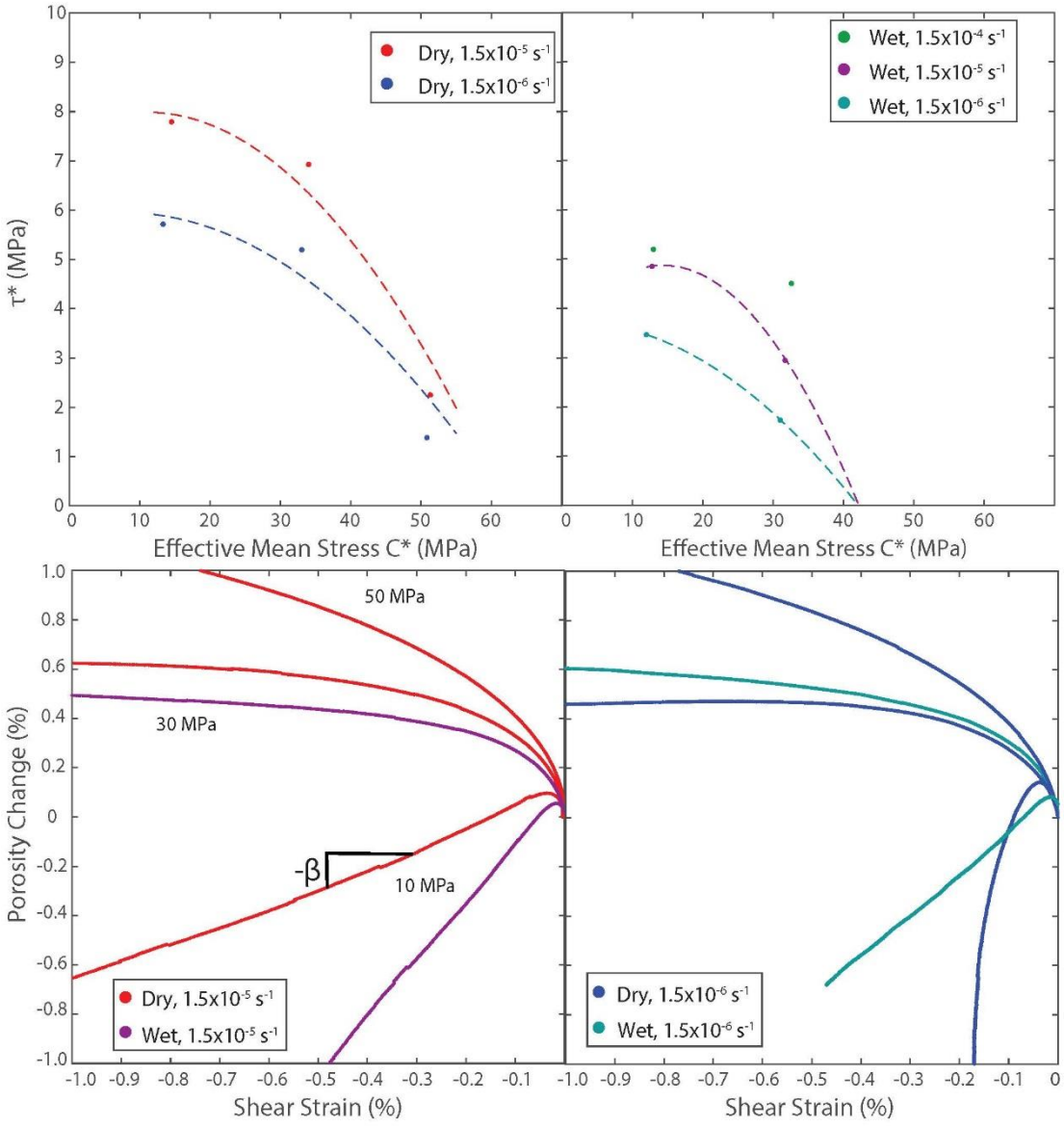

Figure 2.9: Top: Compactive yield envelope derived from initiation of shear-enhanced compaction (C*); bottom: plots of shear strain against porosity change in Indiana limestone. The dilatancy factor (β) is inferred from the negative slope of the shear strain plot following the onset of inelastic compaction.

The effective pressure applied during deformation appears to have the most noticeable effect on systemically changing the deformation behavior of Indiana limestone. In Figure 2.9, shear strain is plotted against the porosity change in order to clarify the change from brittle dilatant behavior to semibrittle distributed deformation. The shear strain γ here was inferred from the second invariant of the strain tensor

(*Rice, 1968*; *Rudnicki, 2004*). The slope of the lines can be used to infer the dilatancy factor following the onset of shear-enhanced compaction (β). As the slope transitions from more positive to more negative with increasing pressure (*Fredrich 1989; Renner and Rummel, 1996*), the dilatancy factor serves as a good indicator of the transition from dilatant brittle deformation to distributed cataclastic flow. All values are reported in Table 2.1.

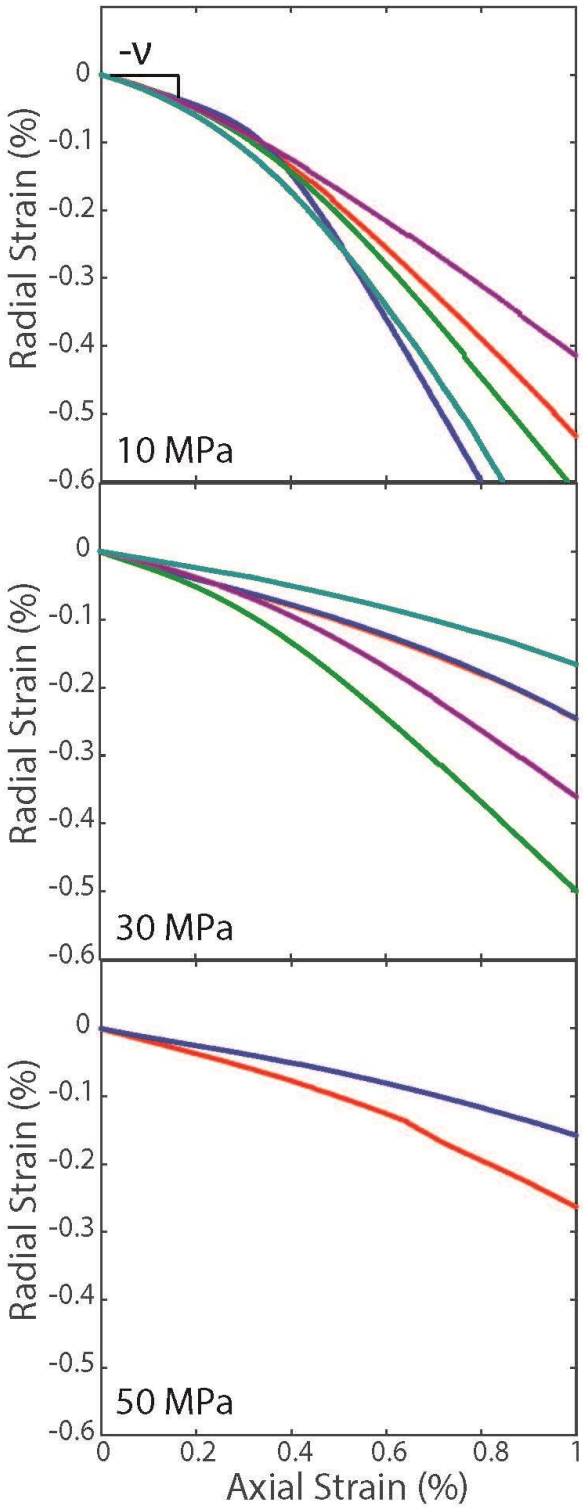

Figure 2.10: Plots of axial strain against radial strain as a function of confining pressure. The negative of the Poisson's ratio (ν) may be inferred from the slope of the elastic portion of the mechanical data in these plots.

The transition from brittle to semibrittle deformation (nomenclature from *Evans et al., 1990*) in Indiana limestone occurs between the effective pressures of 10 and 20 MPa, in agreement with previous findings (*Vajdova et al., 2004*). At 30 and 50 MPa confining pressures, the behaviors are consistent despite the change in magnitude of the strain rate during deformation. Interestingly, at the low confining pressure of 10 MPa, the slower strain rate deformation actually experienced greater dilatancy for the same degree of axial strain (see Figure 2.11). This is contrary to what is expected in that an increase in strain rate is expected to lead to an increased embrittlement of a rock during axial deformation (*Wawersik and Fairhurst, 1970*; *Rutter, 1974*). However, porous carbonate rocks can have wide petrophysical heterogeneity over small geologic scales in properties such as porosity, permeability, grain size, and texture (*Folk, 1959; Hugman and Friedman, 1979*; *Lønøy, 2006*; *Huella and Nicholls, 2012*). More recently, *Dautriat et al. (2011)* and *Nicolas et al. (2016)* found, within the transitional regime between brittle and semibrittle deformation in porous carbonate rocks, the deformation response can be highly variable even for the same loading conditions. At 10 MPa confining pressure, for Indiana limestone, Indiana limestone could potentially deform in both the brittle and semibrittle deformation regimes (*Vajdova et al, 2004*; *Zhu et al., 2010*).

2.4.2: Effect of Water

The hydrostatic deformations with water as a pore fluid show a significant reduction of the P* value as compared to the dry hydrostatic experiment (38 and 42 MPa compared to 61 MPa). The bulk moduli for the elastic portion of the deformation show little variability (see Table 2.1). This indicates that though the

onset of grain-crushing is significantly reduced by the presence of water, the effective compressibility of the rock and its pore spaces is largely unchanged (*Baud et al., 2000a*; *Vajdova et al., 2004*).

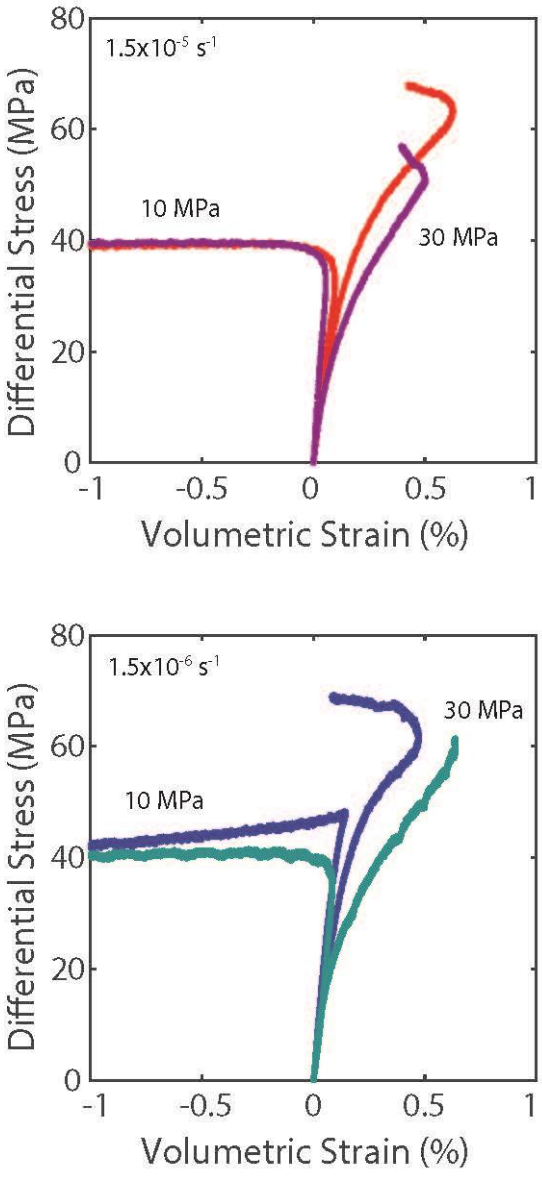

Figure 2.12: Volumetric strain following the application of differential stress. Water-saturated deformations only display pronounced weakening at the greater effective pressure of 30 MPa. Red, blue are dry data; violet, turquoise are water-saturated data.

Qualitatively, the axial deformations show only limited changes in the observed strain behavior and no change in the mode of failure (compactant or dilatant), similar to what is observed in the deformation of porous sandstones (*Baud et al., 2000b*). The effect of water during axial deformations is variable, and seems to be dependent on the confinement condition applied during deformation. At the lower effective pressure of 10 MPa, the deformations appear to be unchanged for the conditions utilized in this study (Figure 2.12). It does appear however that no noticeable reduction in the deviatoric stress occurred during each water-saturated deformation, unlike during the dry deformation. This may indicate that while the observed deformation behavior is largely the same at these conditions, water may have the effect of suppressing brittle deformation mechanisms at the transitional stage of deformation through the addition of chemically-induced deformation mechanisms such as pressure solution creep. The apparent lack of significant weakening of porous limestone is similar to experimental observations of water-saturated Indiana limestone (*Glowacki and Selvedurai, 2016*).

At effective pressures of 30 MPa, Indiana limestone shows a reduction in the maximum differential stress required to facilitate compaction when saturated with water (see Figure 2.12) following the onset of inelastic compaction. The pressure required to facilitate shear-enhanced compaction (C*) shows a minor reduction for all water saturated samples, though the transition to shear-enhanced dilation occurs at much lower effective stresses than under similar conditions without fluids present. Coupled with the hydrostatic data, this suggests that fluid-assisted weakening of

Indiana limestone is related to the effective stress experienced by the rock prior to axial deformation.

One possible explanation for the change in the water-weakening behavior could be from a shift in the micromechanics of deformation. When saturated with water, fluid-enhanced subcritical cracking and pressure solution will both be occurring in Indiana limestone. At lower confining pressures, the opening of microcracks will occur more easily than other deformation mechanisms. At higher confining pressures, the opening of microcracks is suppressed by the increased pressure. At lower effective confining pressures the propagation of subcritical cracks through dissolution of crack tips is likely the controlling deformation mechanism, and the increased dilatancy as a result may diminish the compactive behavior associated with pressure solution (*Le Guen et al., 2007*; *Liteanu et al., 2013*). At greater confining pressures this allows more deformation to be accommodated by the pressure solution creep, while the opening of microcracks is impeded by the increased confining pressure.

2.4.3: Effect of Strain Rate

Observation of hydrostatic compaction in the presence of fluids suggests that a reduction of an order of magnitude in loading rate has no appreciable change in the observed compaction behavior (Figure 2.7). This is reasonable, as chemically-assisted weakening in sedimentary rocks is largely driven by the application of differential stress and the regional temperature conditions (*Lehner, 1959*; *Zhang and Spiers, 2005; Croizé et al., 2013*). It can be observed that a change by one order of magnitude in the

strain rate of axial deformation has no significant effect on samples deformed while under dry conditions as well (Figure 2.13). This is in agreement with previous work exploring time-dependent weakening of porous limestone (*Lajtai et al., 1991*). While under dry conditions, plastic deformation of most rocks occurs primarily through increased microcracking and, in the case of carbonate rocks, crystal plasticity processes such as twinning and dislocation slip (*Brantut et al., 2014a*). At the strain rates used here, microcracks propagate at speeds much higher than natural subcritical cracks develop. Thus the propagation of microcracks is instead determined by the critical stress intensity factor at microcrack tips, which is essentially time-independent (*Costin, 1983*). Likewise, crystal twinning is a primarily ductile process, and is largely a function of the pressure and temperature experienced to the rock during deformation (*Burkhard et al., 1993*; *Ferrill et al., 2004*).

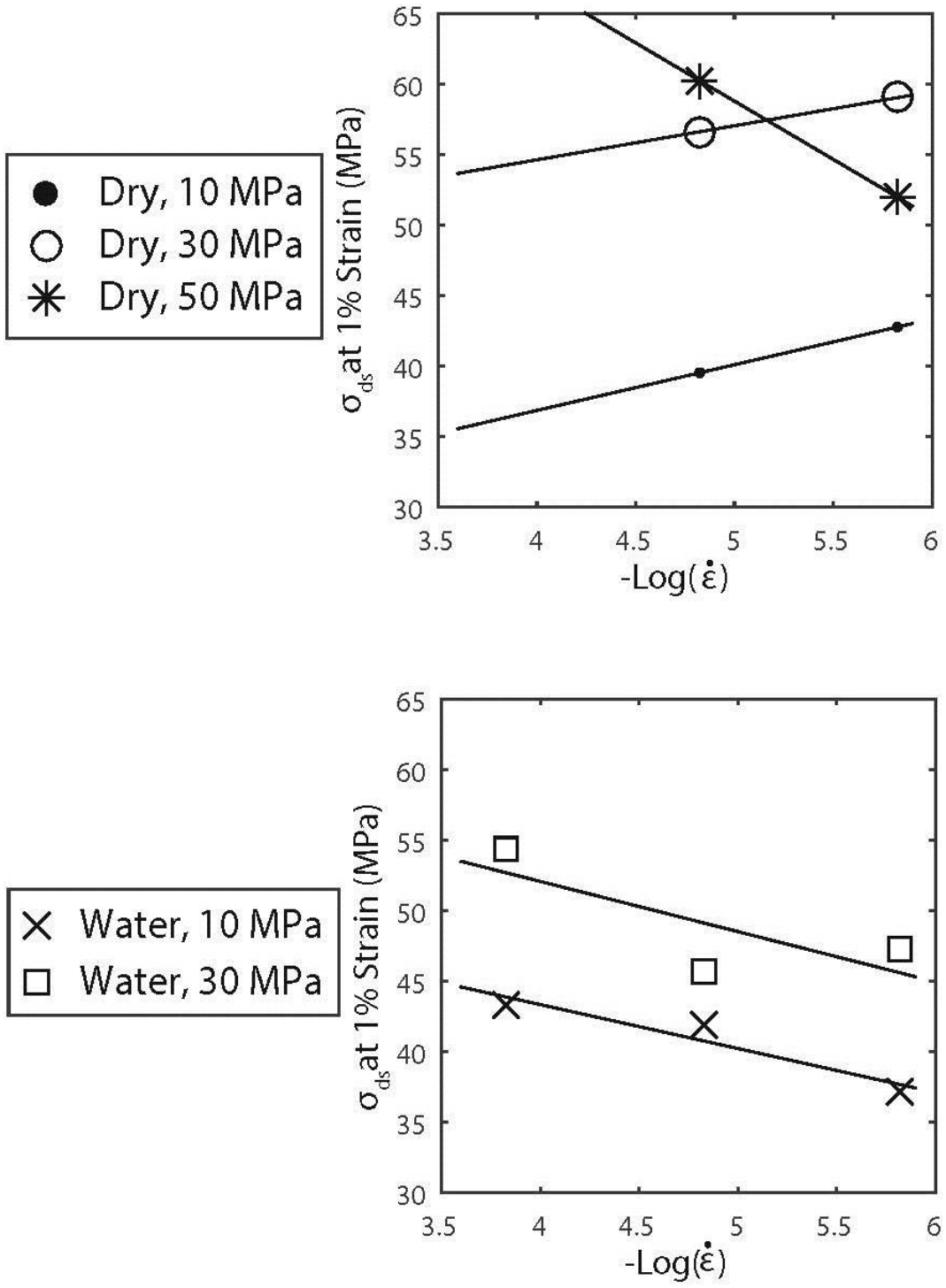

Figure 2.13: Data for differential stress achieved at 1% axial strain for all experiments deformed with differential load. Values for the strain rate ($\dot{\varepsilon}$) applied are reported in negative log values.

Conversely, the presence of fluids adds chemically-assisted deformation mechanisms, which are strictly time-dependent (*Brantut et al., 2014a*). At the

temperature conditions utilized in this study, the period of time required to achieve fluid equilibrium with calcite should be within 50 hours of the addition of non-equilibrated water (*Zhang and Spiers, 2010*; *Liteanu et al., 2013*; *Lisabeth and Zhu, 2015*). This means that the fluid should not be in equilibrium and dissolution of the calcite should be occurring throughout the experiment, allowing for time-dependent weakening of the limestones. However, there is not a significant variation in mechanical behavior between the deformations conducted at an effective pressure of 10 MPa (Figure 2.8). No embrittlement was observed as the strain rate was increased from $1.5x10^{-6}$ s^{-1} to $1.5x10^{-4}$ s^{-1} (see Figure 2.13). Indeed, at the intermediate strain rate condition, the water saturated limestone seemed to experience greater shear strain than its dry counterpart (see Figure 2.13). It is worth noting however that the differential stress required to achieve the same degree of strain decreases systematically as the rate of strain is decreased, unlike the deformations conducted under dry conditions (Figure 2.13). This may indicate that time-dependent deformation is occurring, but the change in the mechanical behavior of the limestone is not significant at this effective pressure.

At effective pressures of 30 MPa, there is a decrease in the differential stress required to achieve both shear-enhanced compaction and dilation (C* and C*') (Figure 2.12), unlike in the lower effective pressure experiments. Similar to the 10 MPa experiments, there is also a systematic decrease in the stress achieved at 1% axial strain (Figure 2.13).

The water saturated experiment conducted at $1.5x10^{-4}$ s^{-1} achieves a slightly greater differential stress than either of the dry Indiana limestone experiments. This

strengthening could be due to a number of reasons. First, as noted in Equation 1.2, the maintenance of the same effective pressure is dependent upon a constant pore pressure. However, if the reduction in permeability is rapid enough, pore fluid will be unable to escape, leading to a localized increase in pore pressure and subsequent embrittlement. Such behavior has been previously observed in both limestones (*Rutter, 1972*) and sandstones (*Duda and Renner, 2013*). At an effective pressure of 10 MPa, this strengthening does not seem to occur for the same strain rate. This is likely due to either only a small decrease in permeability being achieved at such a low effective pressure, or due to the counter effect of permeability increasing in the brittle regime due to the opening microcracks subparallel to the maximum principal stress in sedimentary rocks (*Zhu and Wong, 1997*).

Alternatively, it could be that the fluid-assisted mechanisms of deformation are not enabled at such a rapid strain rate. As strain rate is decreased, the effect of calcite dissolution on deformation behavior becomes more prominent, and reduction of strength occurs with each magnitude of strain rate decrease. The changes in behavior suggest that time-dependent weakening is occurring in the water saturated samples at all conditions, but that only with greater confinement is the change in deformation response appreciable. It is possible that this may be due to a shift in the controlling micromechanism of deformation between the two pressure conditions.

Chapter 3: Indiana Limestone Petrophysical and Microstructural Analysis

Microstructures can serve as a bridge between laboratory-conducted rock analysis and field observations of deformed rocks. They are particularly important for calcite-rich rocks, as deformation behavior can be accommodated by more than simple microcracking and cataclasis even at room temperature. This analysis will seek to use stereologic techniques to analyze post-test behavior of Indiana limestone deformed in laboratory conditions.

3.1: Quantitative Analysis Procedure

3.1.1: Methodology

Petrophysical Analysis

The behavior of a rock under stress is highly interrelated with the petrophysical properties (*Wong et al., 1997, Patterson and Wong, 2005, Vajdova et al., 2012*). Properties such as average grain-size, porosity, pore connectivity, and mineralogy can all have a significant impact on deformation behavior. Carbonate rocks in particular are additionally influenced by the specific texture and composition (see *Hugman and Friedman, 1979, Vajdova et al., 2004, Zhu et al., 2010, Dautriat et al., 2011*). High petrophysical variability in sedimentary rocks has been shown previously to hide changes in the mechanical behavior due to changes in deformation conditions (*Donath and Fruth, 1971*). Given this, three properties are evaluated to characterize the compositional properties relevant to the observed deformation behavior: the initial porosity, the grain/matrix proportion, and grain size distribution.

Initial porosities are determined via the saturation method mentioned previously. All porosity measurements are reported in Table 3.1. Indiana limestone is an oolitic grainstone primarily composed of two components: large allochems composed of a combination of micrite and calcite spar, with a matrix of calcite spar (*Churcher et al., 1991*) (Figure 3.1). Though the rock is dominantly composed of calcite (>98%), previous studies have noted that deformation in Indiana limestone is unevenly accommodated between these components (*Vajdova et al., 2012*). Additionally, numerical studies (*Yin and Mavko, 1994*; *Wong and Wu, 1995*) as well as laboratory experiments (*Menéndez et al., 1996*; *David et al., 1998*) have indicated that even a small change in the cement content (i.e. matrix material) plays a significant role in sedimentary rocks' elastic and inelastic response to deformation. In order to find the average proportion of each component, a point count was performed on a thin section of an undeformed sample of Indiana limestone. 300 points were taken to eliminate bias in the analysis. Photomicrographs were taken at 10X magnification. Analysis divides components into micrite, intracrystalline spar, and intercrystalline spar. Data is compared with previous results for Indiana limestone published in *Hugman and Friedman (1979)*.

The grains of Indiana limestone vary in shape from elongate ellipsoid to nearly spherical. To find grain size of the limestone, photomicrographs of an undeformed Indiana limestone thin section were taken at 10X magnification to find the average diameter of individual grains. A chord length analysis (*Underwood, 1972*) was used to find the average grain diameter of the limestone samples. A series of horizontal lines were drawn through a vertical line crossing a series of

photomicrographs. A chord was drawn in both the horizontal and vertical directions to find the average grain diameter (*Underwood, 1972*). Horizontal lines were spaced at 0.5 mm increments from one another.

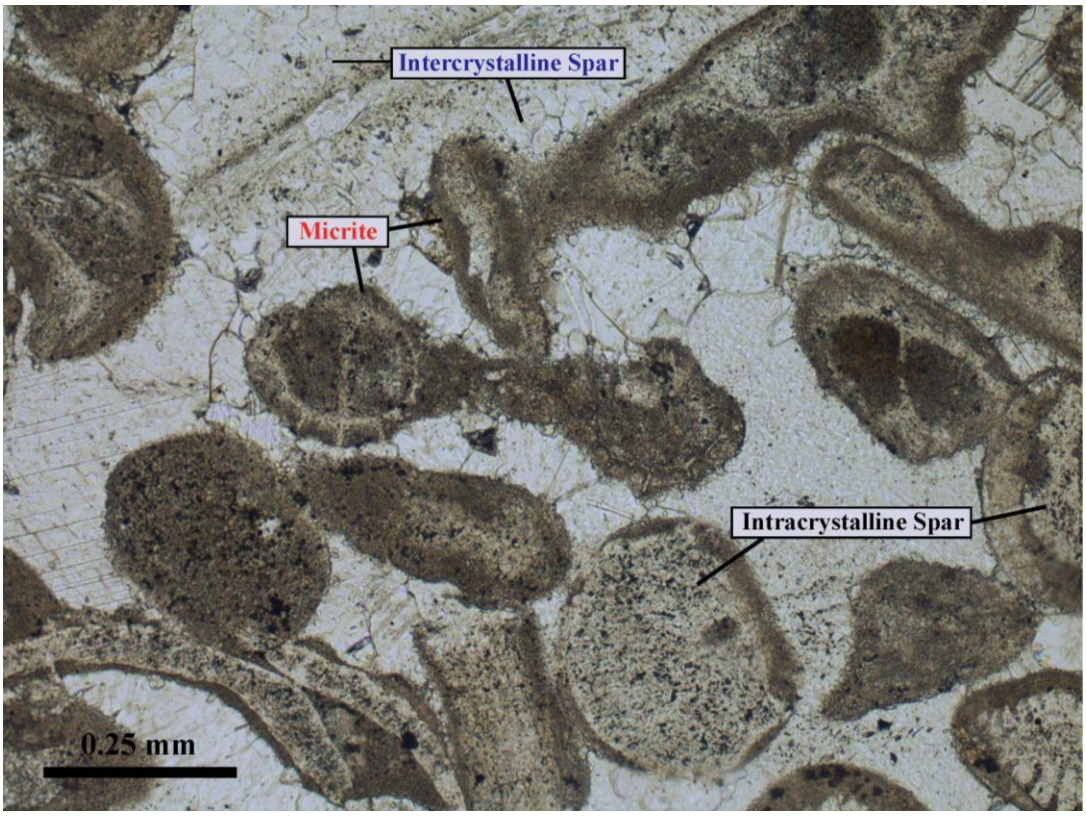

Figure 3.1: Diagram shows the variability of individual grains both in terms of the texture and morphology.

Microstructure Analysis

Quantitative analysis of each limestone thin-section was performed using a modified variation of the stereologic methods utilized in *Menéndez et al. (1996).* A

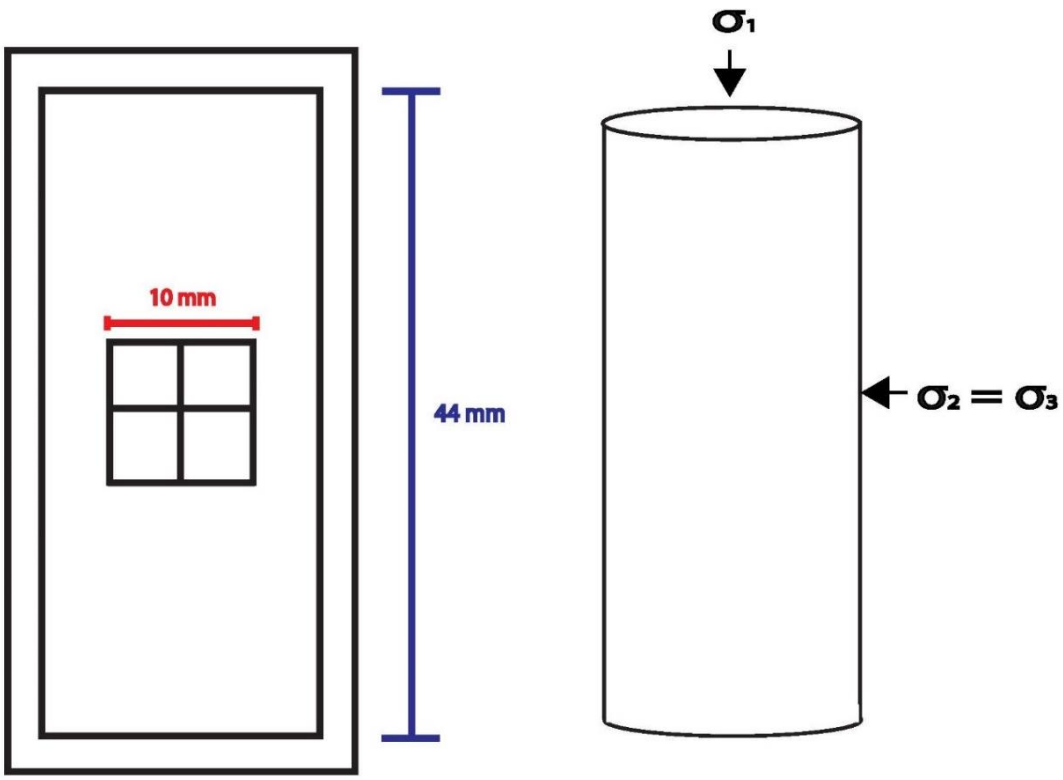

Figure 3.2: Schematic of microstructural analysis. All micrograph lines were parallel or perpendicular to the maximum compressive stress σ_1.

series of micrographs approximately 10 mm in length by 1.4 mm in width were taken through each section: three parallel and three perpendicular to the maximum compressive stress (σ_1) (Figure 3.2). In order to measure the density of specific deformation features, lines were drawn through each series of micrographs. Each line was used to characterize the individual microstructures, with each feature being crossed treated as a single incident. Similar methodologies have been used in prior work with sandstones (*Wong et al., 1992*; *Menendez et al. 1996*; *Tamarkin et al. 2012*) and optical measument of microstructure density has been corroborated by measurement of acoustic emissions in sandstones (*Sayers et al., 1990*) and cracked glass (*Mallet et al., 2013*). The length of each line was measured, allowing for the occurrence of microcrack, twin, and pressure solution incidents per mm to be

calculated. To reduce error and bias ten lines were taken, five perpendicular to σ_1 and five parallel to σ_1 (referred to as horizontal and vertical in analysis respectively). Multiple lines allow for a better average of the microstructures occurring in each rock and an approximation of the degree of anisotropy of each feature in the direction of the maximum and least compressive stresses. All analyses were performed at 10X magnification.

3.1.2: Microstructures

Microcrack Density Analysis

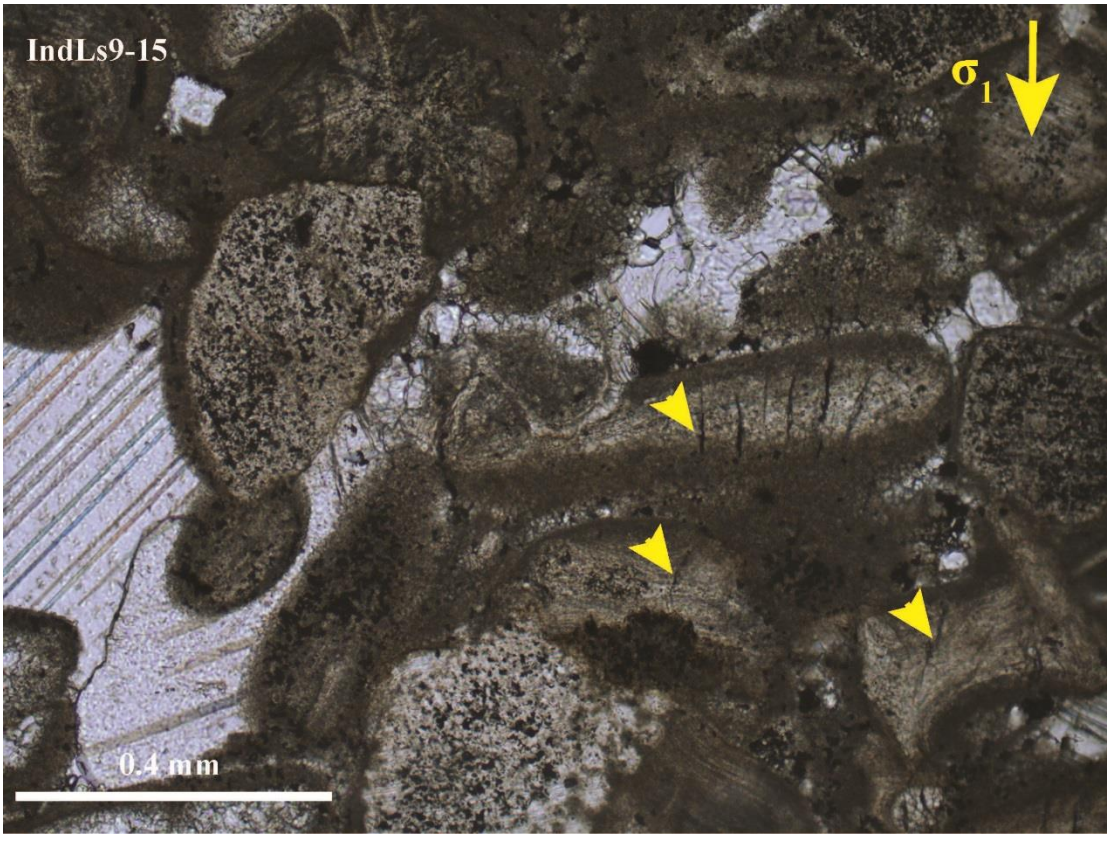

Figure 3.3: Photomicrograph taken at 10X magnifications. The maximum principal stress was vertical in the image. Microcracks are labeled with yellow arrows.

The degree of microcracking in each sample is analyzed for each sample. Each crack that intercepts a given line is considered a single incident of

microcracking. The incidence of microcracking was averaged between the five lines in each direction and recorded as incidents per mm (mm^{-1}). Cracks intercepted by the vertical lines parallel to σ_1 are referred to as $P_L^{\perp}$ (cracks are oriented parallel to σ_3) while cracks intercepted by the horizontal line parallel to σ_3 are referred to as $P_L^{||}$ (nomenclature adapted from *Wong (1985)*).

Total incidents of $P_L^{||}$ and $P_L^{\perp}$ occurring in each sample are normalized for the length of each line. If the value of $P_L^{||}$ is greater than the value of $P_L^{\perp}$, then stress-induced anisotropy has led to the preferential development of microcracks parallel to σ_1 and the degree of anisotropy can be calculated.

Pressure Solution Indentation Analysis

Pressure solution density was quantified by counting incidents of grain contacts where grains are completely connected (i.e. no calcite spar between grains). Pressure solution features are primarily marked by indentation and suturing of grain-grain contacts (Figure 3.4). To distinguish between connected grains with little to no pressure solution occurring and contacts showing significant dissolution, two types were quantified. The first includes all contacts where the grains appear to be in contact but no suturing has occurred. The second is where degradation and significant dissolution has occurred between the grains. These are referred to with the nomenclature of G_c and PS respectively (Figure 3.4). As grain size reduction and breakdown are greater for PS contacts, these are expected to accommodate the most strain. By quantifying both the non-sutured and sutured grains at all conditions, the increase in pressure solution accommodated deformation can be represented at all conditions.

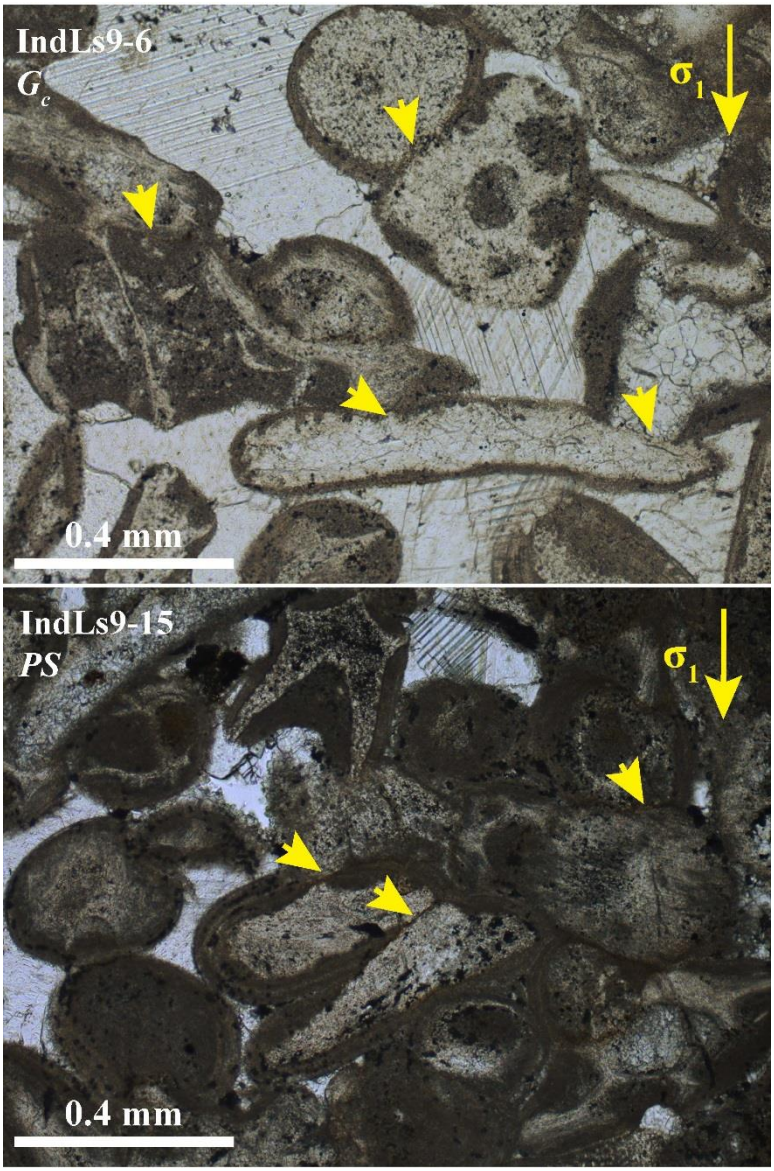

Figure 3.4: Micrograph image shows both G_c and *PS* contacts. Examples of G_c (top) with any grain boundary fully in contact and no calcite spar between are labeled with arrows. Examples of *PS* (right) with prominent dissolution and indentation at the grain contact are labeled with arrows. Images were taken in plane-polarized light at 10X magnification.

If PS-type contacts are more abundant at grain contacts oriented perpendicular, rather than parallel, to σ_1, then pressure solution occurred preferentially through the application of differential stress. This conclusion may be further strengthened if PS indentations perpendicular to σ_1 are more abundant than compared to the dry examples.

Calcite Twin Analysis

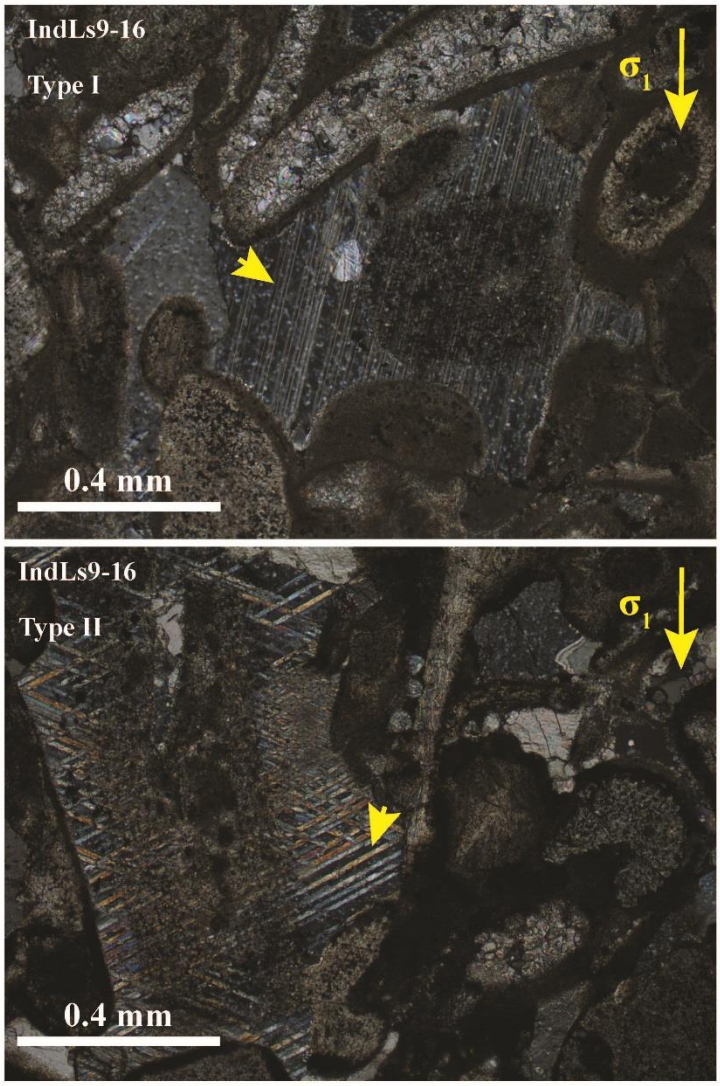

Figure 3.5: Micrograph image shows both type I and II calcite twins. Examples of thin Type I twins (left) are examples of twins counted as one incident in this study. Examples of thick Type II twins (right) are examples of twins normally occurring at high temperatures and are not counted in this analysis. Images were taken in cross-polarized light at 10X magnification.

Four types of twins can be observed in carbonate rocks, following the Burkhard classification for carbonate rocks (*Burkhard, 1993*) (Figure 1.2). In Indiana limestone, only type I and type II twins are observed. The variation in twin types is not related to the pressure conditions but the specific temperature the rock is

subjected to. It is for this reason calcite twinning has been speculated as a potential geothermometer in carbonate rocks (*Rowe and Rutter, 1990).* Type II twins generally nucleate at temperatures in excess of 200 °C. All our deformations were conducted at room temperature (~23 °C). Thus all type II twins in thin section are treated as relics of the original paleostress conditions prior to deformation and disregarded.

In this analysis, one twin plane orientation crossed in the limestone (whether in the spar matrix or grains) is treated as a single incident. The formation of twins in calcite generally relieves stress by dislocation of atoms (*Ferrill et al., 2004*). Forming a second set of twins requires additional stress, so if twinning occurs along two separate planes at the same point, it is counted as two incidents. As calcite twinning and other crystal plasticity mechanisms do not display a preferred orientation, the average normalized values for calcite twins are reported here.

3.2: Results

3.2.1: Petrophysics

Porosity

Initial porosity values for each deformed Indiana limestone were reported in Table 3.1.

Experiment Name	**Initial Porosity (%)**
IndLs9-6	15.9
IndLs9-5	16.9
IndLs8-24	13.4

IndLs9-4	15.1
IndLs8-20	15.6
IndLs8-21	16.7
IndLs8-19	14.9
IndLs9-21	15.8
IndLs9-19	16.5
IndLs9-12	16.9
IndLs9-13	15.9
IndLs9-9	14.9
IndLs9-14	17.4
IndLs9-15	16.9
IndLs9-16	16.7

Table 3.1: Initial porosity values for all Indiana limestone deformations conducted.

The mean porosity of the samples was found to be 16.0%. Using the formula for standard deviation:

$$\sigma_{sd} = \frac{1}{N_T}\sum_{i=1}^{N}\left(x_{\mathrm{i}} - m_p\right)^2 \tag{3.1}$$

where σ_{sd}, N, x_{i}, m_p are the standard deviation, number of variables measured, the individual porosity measurements, and the mean porosity respectively, was used to calculate the standard deviation of the porosity measurements. The deviation was found to be 1.0269. Previous research of Indiana limestone corroborates the highly variable porosity measurements, with porosity values as low as 13% reported in *Logan et al. (1922)* and as high as 20% in *Vajdova et al. (2004)*.

Micrite/Calcite Spar Distribution

Analysis	**Micrite (%)**	**Intercrystalline Spar (%)**	**Intracrystalline Spar (%)**
This Study	47.3	22.5	30.2
Hugman and Friedman (1979)	39.0	19.0	42.0

Table 3.2: Textural analyses conducted on Indiana limestone.

Petrophysical analysis of Indiana limestone performed in both this study and *Friedman and Hugman (1979)* are reported in Table 3.2. Based on these results, Indiana limestone can be classified as a sorted oosparite (*Folk, 1959*). Most of the grains are subrounded oolites with a sparite center surrounded by varying degrees of micrite. The matrix is primarily a crystalline calcite spar surrounding the matrix. While the data for average texture and fabric analysis reported here are relatively similar to previous research with Indiana limestone (*Friedman and Hugman, 1979; Zhu et al. 2010*; *Vajdova et al., 2012*), the differences between reported values suggests the variability may influence the specific deformation behavior occurring in Indiana limestone.

Previous observations of microstructures in deformed Indiana limestone have suggested that the deformation is not equally distributed between the micritic content and the sparite content (*Vajdova et al. 2012, Lisabeth and Zhu, 2015*). While properties such as the grain size, porosity, and calcite content may be similar for the same limestone, the textural variability may play a significant role in varying the deformation behavior at relatively similar conditions. The observed textural variation could offer some explanation as to the observed discrepancies between the

deformation behavior of Indiana limestone in this and previous studies (*Boozer et al., 1963*; *Friedman and Hugman, 1979*; *Vajdova et al. 2004*; *Zhu et al. 2010*; *Lisabeth and Zhu, 2015*).

Grain Size Distribution

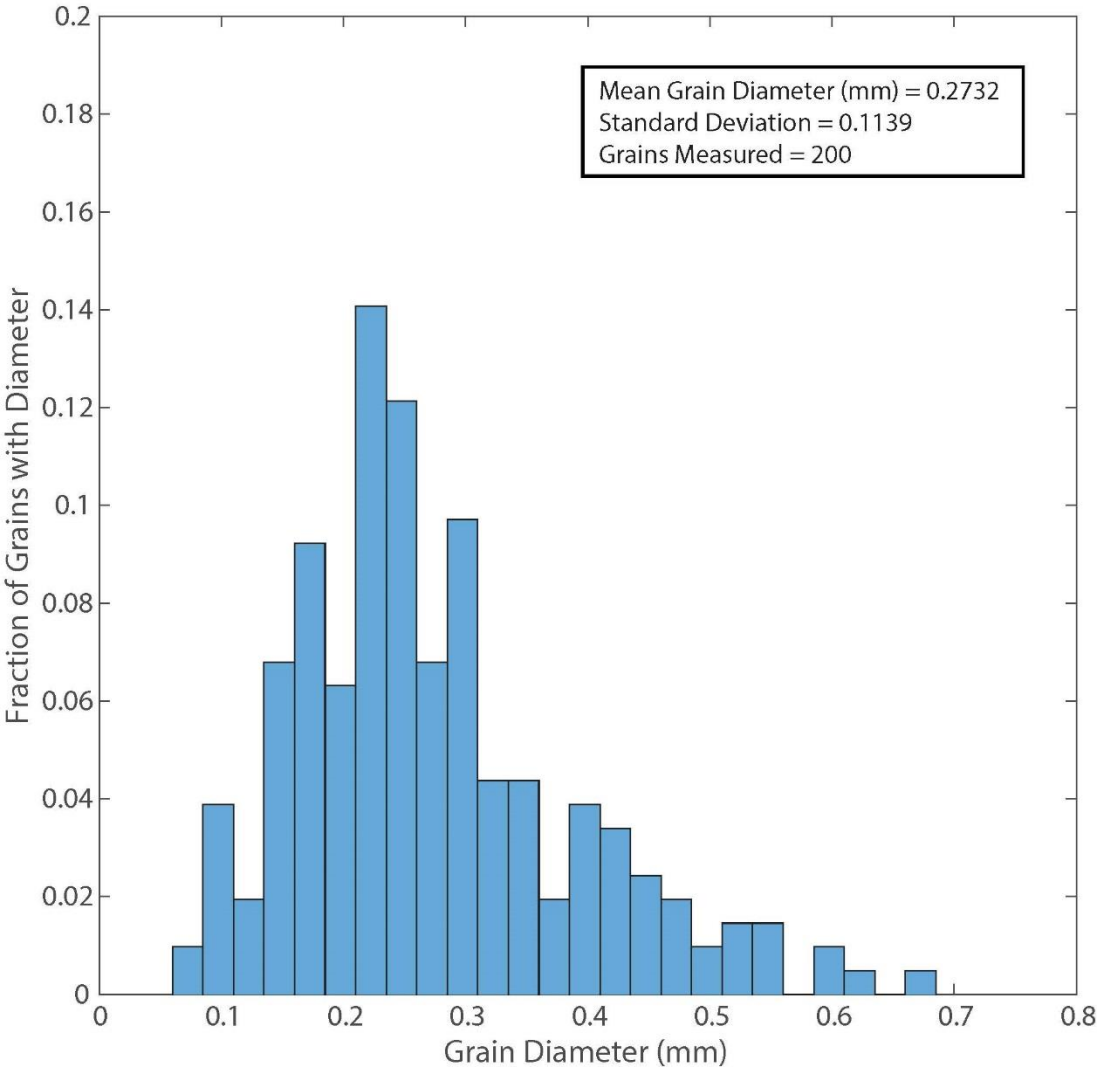

Figure 3.6: Grain size histogram for Indiana limestone used in this study. Mean grain diameter and standard deviation displayed on image.

The grain diameters of 200 grains were found. The grain size distribution was plotted as a histogram to show the average grain size (Figure 3.6). An average grain size was found to be approximately 270 μm, with most having diameters between 200

and 300 μm. A standard deviation of 0.1139 for the grain size distribution was found, in agreement with this.

These values are similar to those reported for the grain sizes found in other work with Indiana limestone (*Zhu et al., 2010*). Most grains are round to sub-rounded ellipsoids, with elongate grains tending to align parallel to bedding and consequently perpendicular to the overburden stress.

	Microcracks			***G_c***		***PS***		**Calcite Twins**
Conditions	$P_L^{\perp}$	$P_L^{\parallel}$	**S_v**	**⊥**	**∥**	**⊥**	**∥**	**Average**
Undeformed	0.28	0.26	0.56	1.06	0.98	0.51	0.37	0.08
Dry, Hydrostatic	0.52	0.29	0.94	1.11	0.68	0.31	0.20	0.34
Dry, 10 MPa, $1.5x10^{-5}$ s^{-1}	0.73	1.10	1.78	0.74	0.56	0.17	0.26	0.39
Dry, 30 MPa, $1.5x10^{-5}$ s^{-1}	0.46	0.62	0.99	1.84	0.95	0.50	0.33	0.54
Dry, 50 MPa, $1.5x10^{-5}$ s^{-1}	0.67	0.80	1.40	1.72	1.04	0.67	0.48	0.52
Dry, 30 MPa, $1.5x10^{-6}$ s^{-1}	0.35	0.77	0.89	2.23	1.10	0.67	0.39	0.20
Dry, 50 MPa, $1.5x10^{-6}$ s^{-1}	0.75	0.92	1.57	2.29	0.86	1.11	0.36	0.35
Wet, 10 MPa, $1.5x10^{-4}$ s^{-1}	0.57	1.34	1.46	2.38	1.22	1.15	0.36	0.10
Wet, 10 MPa, $1.5x10^{-5}$ s^{-1}	0.94	1.34	2.05	1.79	1.13	0.95	0.41	0.28
Wet, 10 MPa, $1.5x10^{-6}$ s^{-1}	0.86	0.97	1.77	1.79	1.26	1.26	1.02	0.42

Wet, 30 MPa, $1.5x10^{-4}$ s^{-1}	0.94	1.28	2.03	1.89	1.47	1.45	0.83	0.30
Wet, 30 MPa, $1.5x10^{-5}$ s^{-1}	0.62	1.02	1.41	2.44	1.83	1.78	1.02	0.24
Wet, 30 MPa, $1.5x10^{-6}$ s^{-1}	0.96	1.05	1.95	2.06	1.52	1.61	0.73	0.53

Table 3.3: Average microcrack, grain-grain contact, pressure solution contacts oriented perpendicular (⊥) and parallel (∥) to the maximum principal stress applied. Calcite twin density averaged over entire sample measured here.

3.2.2: Microcracking

Microstructural data for deformed Indiana limestones is reported in Table 3.3. Data for sample deformed at a confining pressure of 10 MPa and strain rate $1.5x10^{-6}$ s^{-1} could not be listed as damage to the sample during unloading lead to significant breakdown of the rock and made analysis of microstructures untrustworthy. All axial deformations experienced the same axial strain, within ± 0.5%. Line length for each measurement was between 10 and 11 mm. This indicates an average of between 150-200 grains were measured both parallel and perpendicular to σ_1. However, since deformation features appears to have been preferentially accommodated by the calcite spar, this may not be statistically relevant.

Data for microcracks suggests an increase in the observed number of microcracks with an increase in the effective pressure the sample was deformed under. All samples showed a preferential alignment of microcracking parallel to the maximum compressive stress, similar to other microstructural observations of deformed Indiana limestone (*Zheng et al, 1989*; *Vajdova et al., 2012*). This suggests that stress-induced anisotropy is induced in all samples regardless of the effective pressure, strain-rate, or fluid content. For axisymmetrically deformed samples, microcracks measured by the line perpendicular to σ_1 ($P_L^{||}$) and microcracks

measured along the line parallel to σ_1 ($P_L^{\perp}$) can be related by the stereologic parameter:

$$S_V = \left(\frac{\pi}{2}\right) P_L^{\perp} + (2 - \left(\left(\frac{\pi}{2}\right)\right) P_L^{||} \tag{3.2}$$

where S_V quantifies the total crack surface area in a given volume of the deformed rock (mm^2/ mm^{-3}) in a thin section (adapted from *Wong, 1985*).

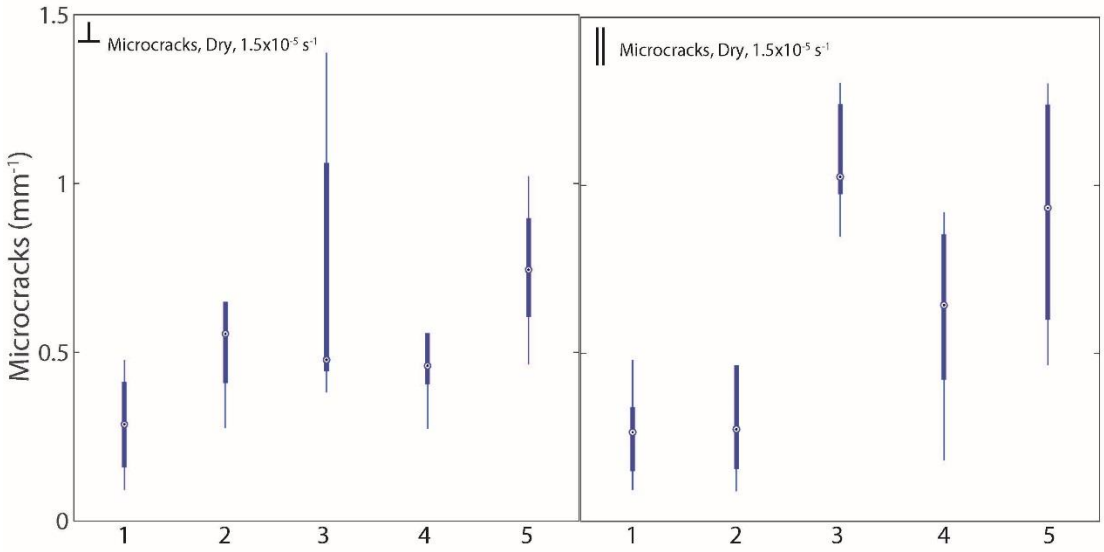

Figure 3.7: Microcracks oriented perpendicular (⊥) and parallel (| |) to the maximum principal stress in limestones deformed at strain rate of $1.5x10^{-5}$ s^{-1} under dry conditions. 1) Undeformed; 2) Hydrostatic; 3) 10 MPa; 4) 30 MPa; 5) 50 MPa.

The density of microcracks in the undeformed sample is relatively low (Figure 3.7). While compaction through hydrostatic loading does increase the density of microcracks, deformation appears to be largely accommodated by the intercrystalline spar, with relatively little microcracking occurring in the grains (Figure 3.7). The application of differential stress induces a significant increase in the density of microcracks occurring at all conditions. Considering the role of effective pressure, there seems to be a slight increase in the density of microcracks on experiments conducted close to the brittle-semibrittle transition (~10 MPa).

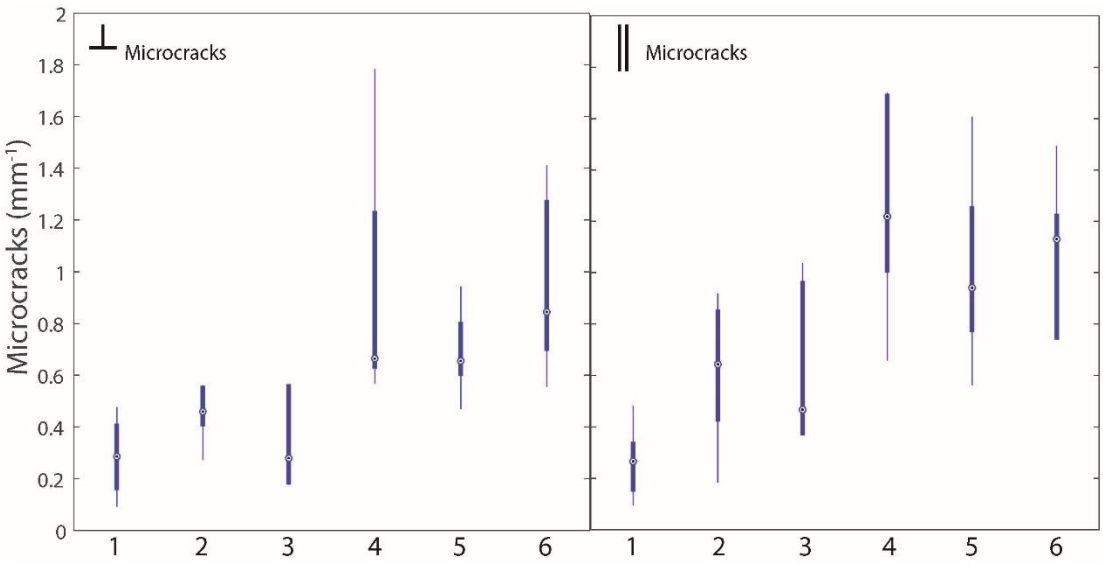

Figure 3.8: Microcracks oriented perpendicular (⊥) and parallel (‖) to the maximum principal stress in limestones deformed with an effective pressures of 30 MPa. Numbers signify strain rate and chemical environment applied in each deformation: 1) Undeformed; 2) $1.5x10^{-5}$ s^{-1}, Dry; 3) $1.5x10^{-6}$ s^{-1}, Dry; 4) $1.5x10^{-4}$ s^{-1}, Wet; 5) $1.5x10^{-5}$ s^{-1}, Wet; 6) $1.5x10^{-6}$ s^{-1}, Wet.

Water saturated samples show a marked increase in the density of microcracks when compared to limestones deformed under dry conditions (Figure 3.8). It is well established that the chemical effects of fluids can facilitate microcracking in geologic materials by lowering the free surface energy (*Orowan, 1944*) or through dissolution of the crack tip. This will be further enhanced by the relatively rapid dissolution of calcite. At the strain rates utilized, it seems that the propagation of microcracks is largely time-independent (*Atkinson, 1984*; *Brantut et al., 2014b*).

The three types of cracks appear in the experiments can be observed in thin section: intergranular cracks (synonymous with grain boundary cracks), intragranular cracks (occurring within the grains) and transgranular cracks (*Simmons and Richter, 1976*; *Kranz, 1983*). Under dry conditions, microcracks rarely appear within the grains, with most of the damage appearing in the microcrystalline spar. Under water saturated conditions, intergranular cracks begin to appear, especially at grain-to-grain

contacts where stress-enhanced dissolution is occurring. Transgranular cracks were rarely observed, and were mainly observed in the water-saturated experiments at higher confining pressure.

Microcrack density appears to be far greater in the calcitic spar as compared to the larger oolitic grains. When microcracking does occur in grains, there seems to be a relation between the elongate nature of the grains and the degree of microcracking observed. The more spherical grains display the least microcracking, while the grains with the largest difference between the maximum and minimum diameters display prominent microcracking. This bares further investigation, as the preferential localization of damage may be dependent not only on the heterogeneity of the cement-matrix material but also the degree of grain size variability.

3.2.3: Pressure Solution Indentation

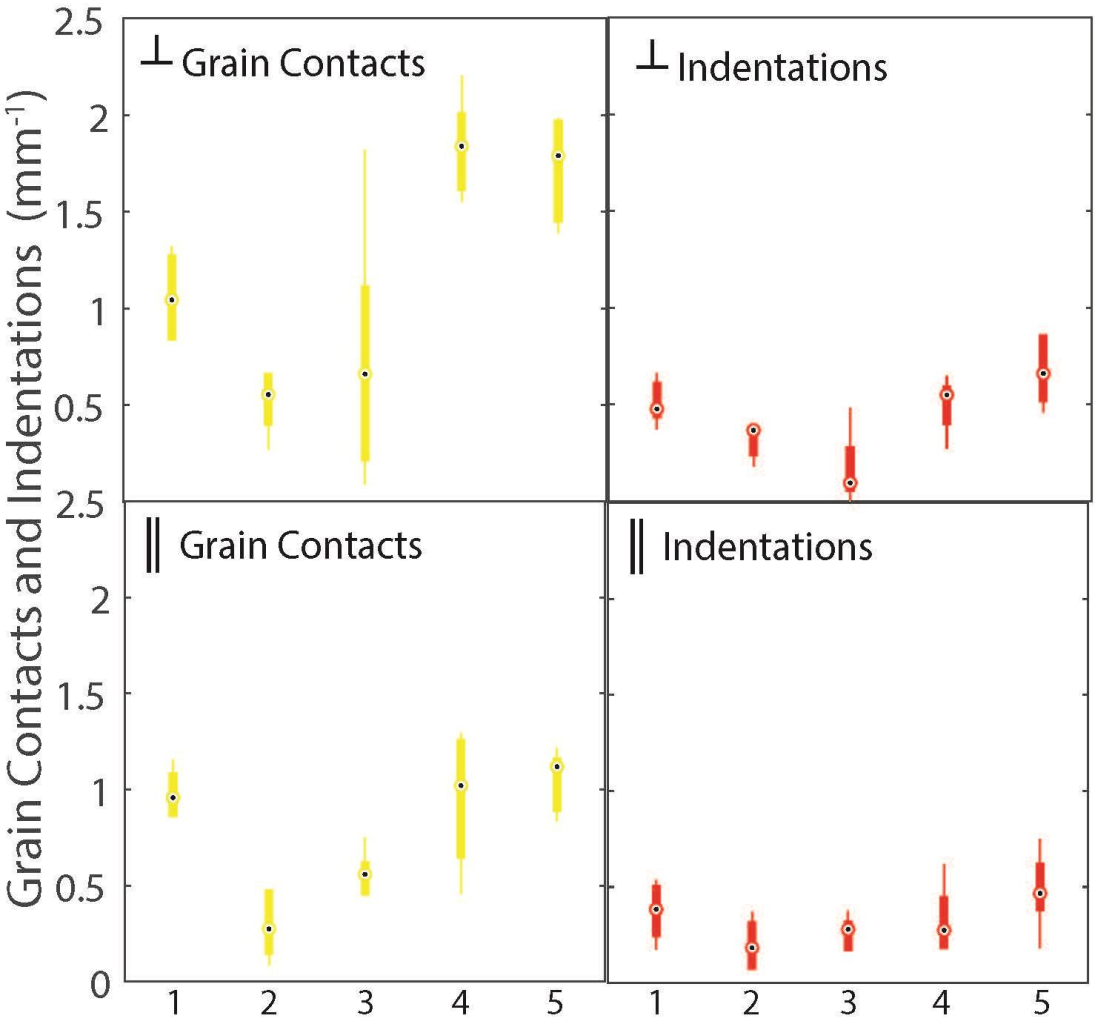

Figure 3.9: Shows number of contacts (yellow, left) and pressure solution indentations (red, right). Grain contacts and pressure solution indentation oriented perpendicular (⊥) and parallel (‖) to the maximum principal stress. It can be seen that the number of contacts increases with increased confining pressure, while the indentations do not change significantly change, reflecting the lack of chemical dissolution. 1) Undeformed; 2) Hydrostatic; 3) 10 MPa; 4) 30 MPa; 5) 50 MPa.

The total number of contacts G_c represents the number of grain contacts where grains are fully connected (i.e. no calcite spar is between the contact) that are crossed by each line. It can be seen that the number of fully contacted grains, whether sutured or otherwise, is relatively low in the undeformed thin section (Table 3.3). The number of grains in contact is lower than the hydrostatic deformation. This is likely due to the undeformed limestone being from a different block of Indiana limestone. It is

observed that the number of contacts increases systematically with the application of differential stress. More grain contacts were noted as the effective pressure was increased in both dry and water saturated conditions.

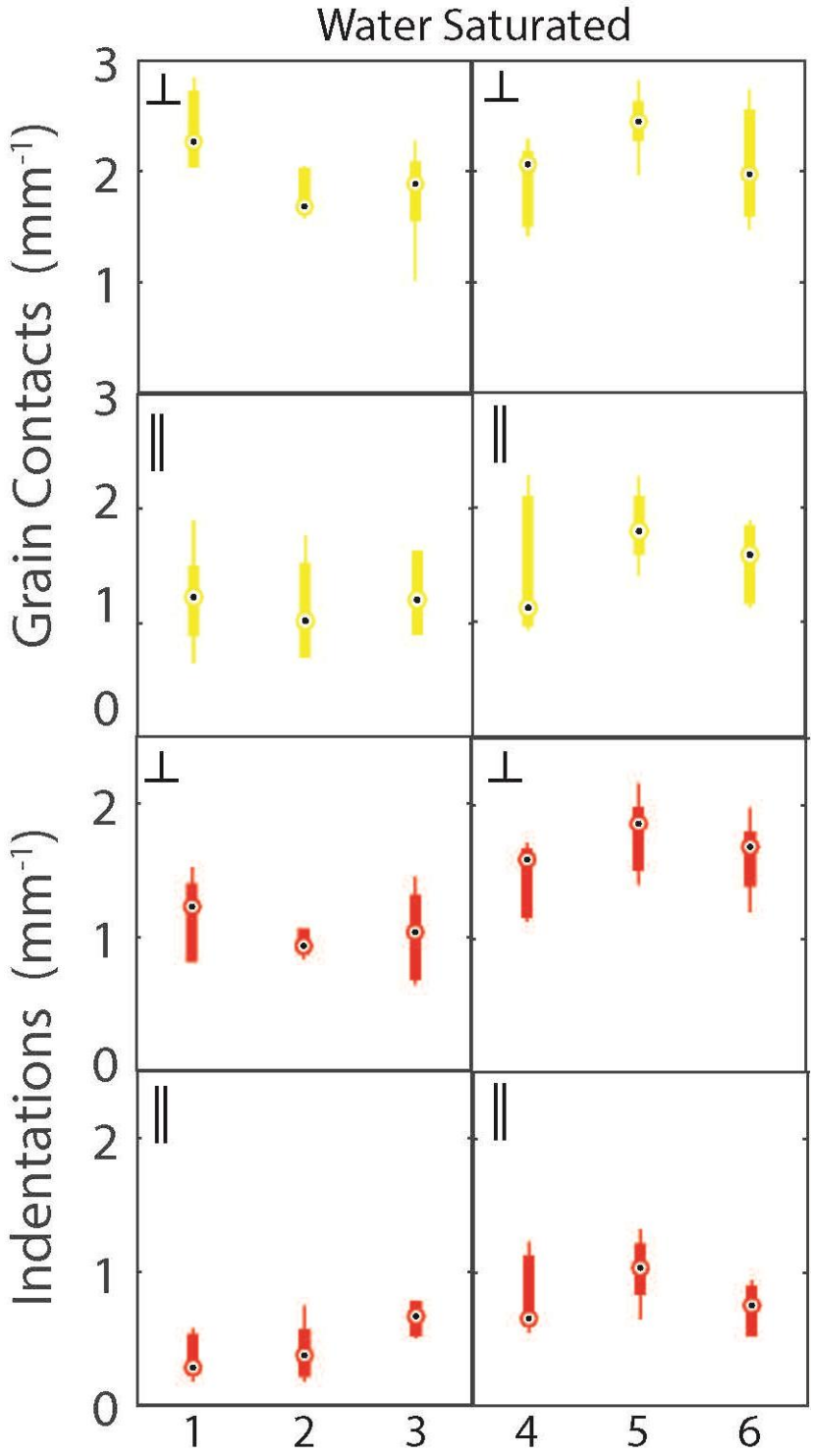

Figure 3.10: Comparison of grain contacts (yellow) and pressure solution indentation (red) at 10 and 30 MPa effective pressure under water-saturated conditions. Grain contacts and pressure solution indentation oriented perpendicular (⊥) and parallel (∥) to the maximum principal stress. 1) 10 MPa, $1.5x10^{-4}$ s^{-1}; 2) 10 MPa, $1.5x10^{-5}$ s^{-1}; 3) 10 MPa, $1.5x10^{-6}$ s^{-1}; 4) 30 MPa, $1.5x10^{-4}$ s^{-1}; 5) 30 MPa, $1.5x10^{-5}$ s^{-1}; 6) 30 MPa, $1.5x10^{-6}$ s^{-1}.

When the limestone is saturated with water there is a marked increase in the number of indented and sutured (*PS*) contacts in thin section. While there is no relationship observed at any strain rate with an effective pressure of 10 MPa, it can be seen that there is a distinct increase in the number of sutured indentations at 30 MPa as the strain rate decreases (Figure 3.10). The number of sutured contacts occurring both parallel and perpendicular to the maximum principal stress increases, showing a heightened grain-grain dissolution as the effective pressure is increased.

3.2.4: Twinning

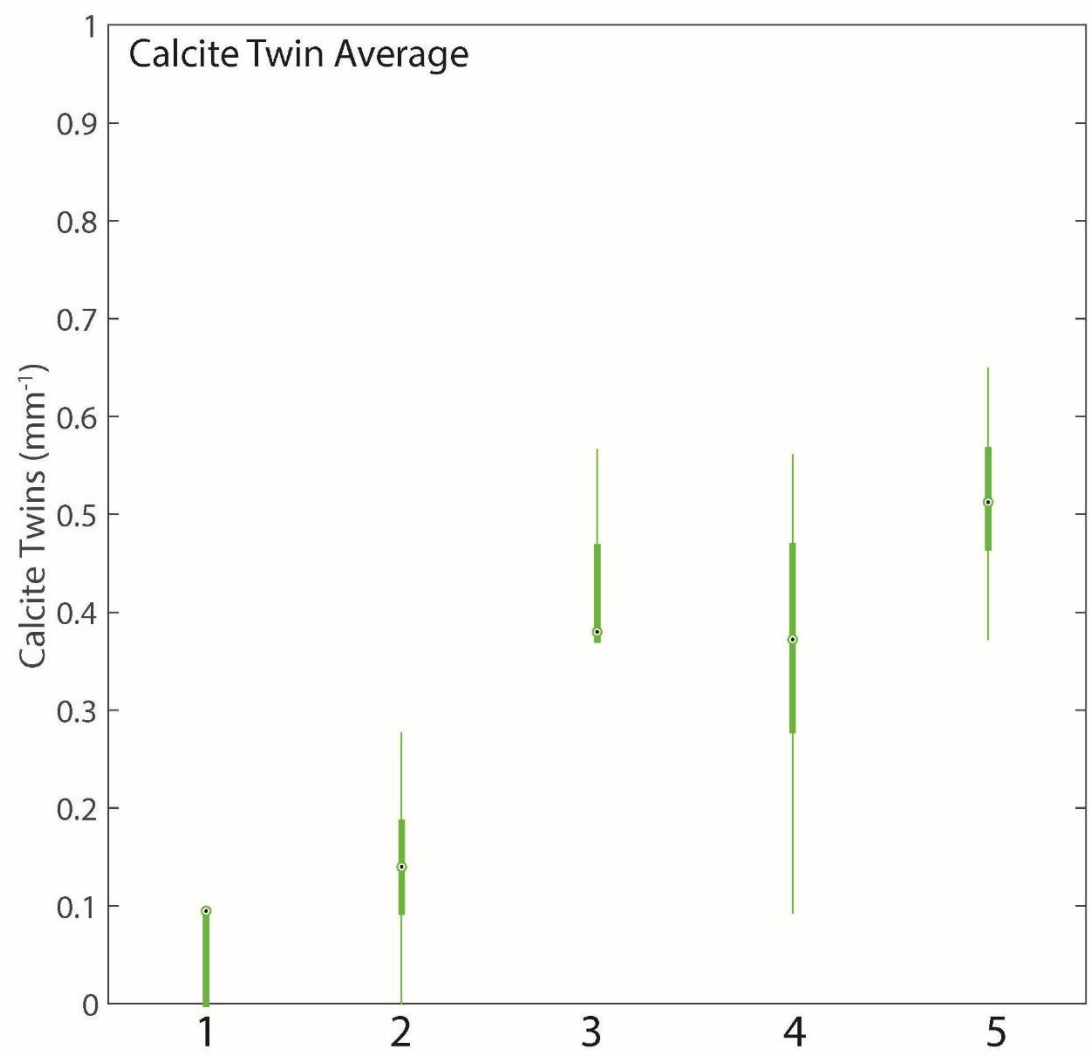

Figure 3.11: Average of calcite twins (green) measured both parallel and perpendicular to the maximum principal stress. These numbers were averaged and displayed here. Figure displays twinning under dry deformation conditions, at a strain rate of $1.5x10^{-5}$ s^{-1}. 1) Undeformed; 2) Hydrostatic; 3) 10 MPa; 4) 30 MPa; 5) 50 MPa.

As can be seen in Figure 3.11, the density of calcite twins measured in all samples is fairly low. There is minor increase in twin density with increasing confining pressure, and potentially with decreasing strain rate. Deformation experiments with marble (*Fredrich et al., 1989*) show that significant twinning in calcite is induced primarily at much greater axial strains than were applied here. Since all the samples were axially deformed within 2-3% axial strain and at room

temperature, the low density of Type I twinning is to be expected. It is worth noting that in all samples the density of Type II twins appears to be still higher than the number of Type I twins both pre-existing in the limestone and induced by deformation.

Chapter 4: Discussion

4.1: Stress-Induced Anisotropy in Dry and Water Indiana Limestone

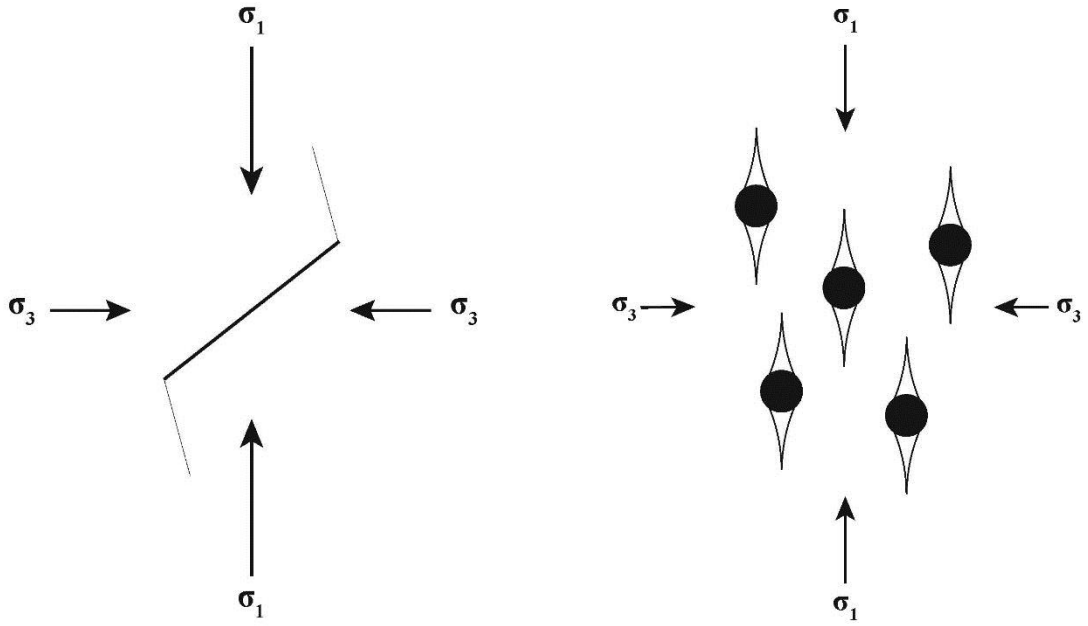

Figure 4.1: Models for microcrack propagation. Left) "sliding wing crack" model is more appropriate for brittle dilatant deformation in carbonate rocks. Right) "pore-emanating crack" model is more appropriate for compactive semibrittle or ductile deformation in carbonate rocks (*Vajdova et al., 2012*). In either model, the stress-induced anisotropy is predicted to decrease with increasing confining pressure and increasing initial porosity (*Baud et al., 2000a*).

The microstructural observations indicate that for all axially deformed cases stress-induced anisotropy was initiated in Indiana limestone (Table 3.3). The anisotropy of crack damage in rocks has been studied in low porosity rocks (*Tapponnier and Brace, 1976*) and high porosity rocks (*Baud et al., 2000*; *Wu et al., 2000*; *Vajdova et al. 2004*). One conceptual model from fracture mechanics widely used to analyze the micromechanical process of fracture growth is the "sliding wing crack" (Figure 4.1, left) (*Kemeny et al., 1991*). This model considers the growth of "wing cracks" initiating from tensile stress concentrations at pre-existing flaws or cracks undergoing frictional sliding. The fracture mechanics is such that the

increasing stress will lead to a propagation of the wing crack along a path quasi-parallel to the maximum principal stress (σ_1). However, fracture nucleation in porous carbonate rocks has been seen to also occur pre-existing pore spaces rather than microscopic flaws (*Baud et al., 2000a*; *Vajdova et al., 2012*). *Vajdova et al. (2004)* observed that for compactive non-localized deformation in Indiana limestone, a pore-emanating crack model was more appropriate (see Figure 4.1) (see *Sammis and Ashby, 1986*).

With increasing confining pressure, it has been shown that stress-induced anisotropy of decreases for the same degree of axial strain (*Wu et al. 2000*). The results of this analysis also suggest similar results for Indiana limestone deformed under dry conditions. The greatest variation in crack density measured parallel and perpendicular occurs at the confining pressure of 10 MPa, where microcrack density is greater than for all the other deformed limestones (Table 3.3). Anisotropy of microcracks decreases from the 10 MPa experiments progressively with increasing confining pressure (Figure 3.7, Table 3.3). Under increased confining pressure, the opening of tensile Mode I cracks, the most commonly observed in deformed rocks (*Kranz, 1983*), is increasingly opposed and requires greater stress to propagate crack tips. However, under dry conditions, the variation of one magnitude in loading rate does not lead to a significant variation in the anisotropy of crack damage. This means that for nominally dry conditions and moderate strain rates, the propagation of microcracks (the primary mechanism of deformation) in Indiana limestone is dependent on the stress intensity at crack tips, and thus only the applied stress during deformation.

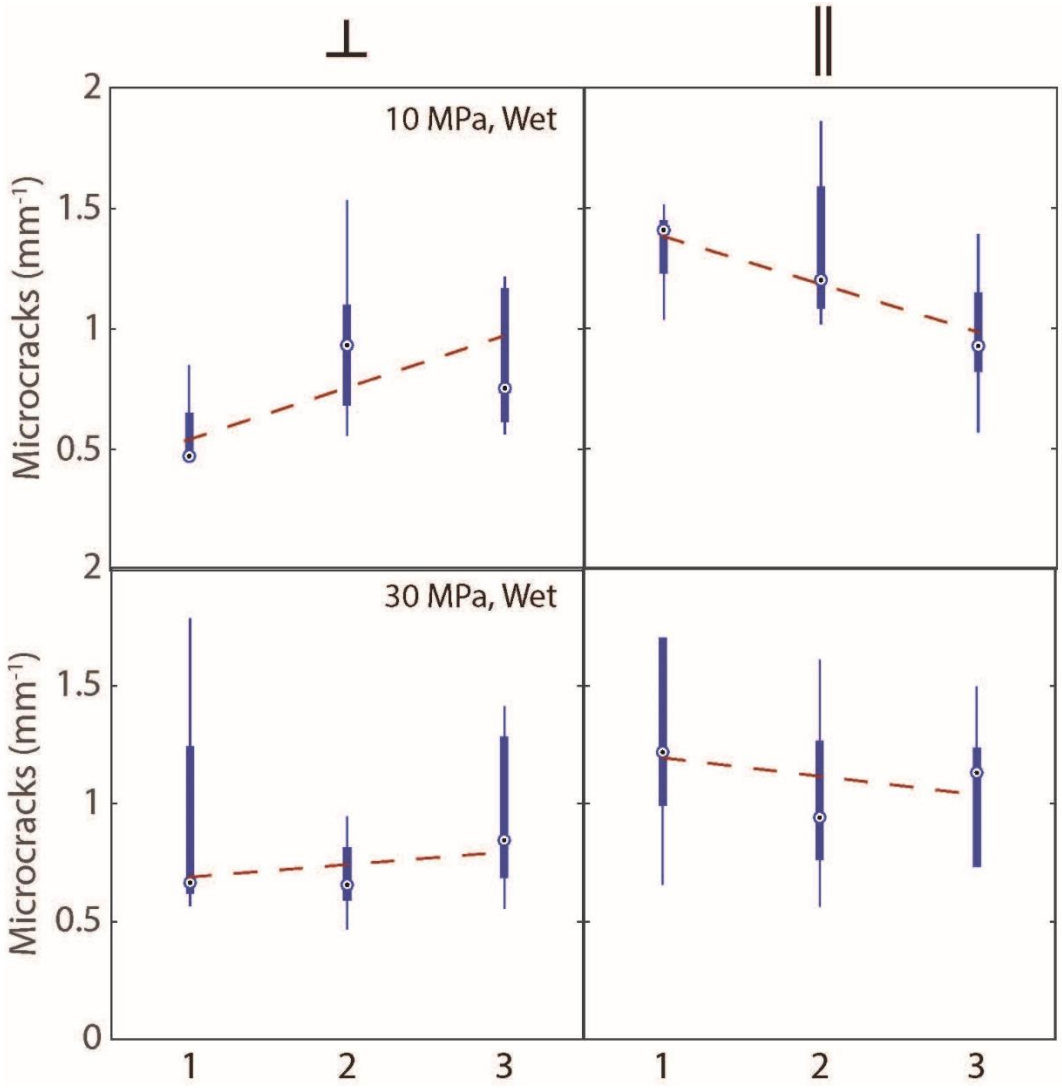

Figure 4.2: Density of microcracks oriented parallel (||) and perpendicular (⊥) to the maximum principal stress (σ_1). For both confining pressures (10 and 30 MPa) there is a trend of decreasing stress-induced anisotropy in each sample with decreasing strain rate. This suggests that the addition of water makes the microcrack propagation time-dependent, due to the effect of chemical dissolution at the crack tip. 1, 2, and 3 represent three strain rates used: $1.5x10^{-4}$, $1.5x10^{-5}$, and $1.5x10^{-6}$ s^{-1} respectively.

The degree of microcracks oriented parallel and perpendicular to the maximum principal stress is on average greater than for the deformations conducted under dry conditions (see Table 3.3). When deformed in a chemically active environment, the deformation of Indiana limestone transitions to time-dependent (see 2.4.3). As strain rate is decreased for the water saturated Indiana limestone, at both confining pressures, the degree of stress-anisotropy decreases (Figure 4.2). Unlike

when deformed under dry conditions, the change in mechanical loading rate appears inhibit stress-induced anisotropy, and potentially decrease the overall dilatancy of the deformation.

The increased propagation of microcracking due to the presence of water could occur for one of two reasons. First, the water could alter the mechanical strength of the solid material and thus decrease the required stress needed to initiate microcracks, also known as the Rehbinder effect (*Baud et al. 2000b*). Second, the chemically active environment may allow for stress-corrosion cracking, or dissolution of a crack tip allowing for decreased stress requirements for crack tip growth (*Atkinson, 1981*), to occur. Of these two, only the process of stress-corrosion crack propagation would agree with the observation that deformation of Indiana limestone becomes time-dependent with the addition of water.

However, microcracking is likely not the mechanism responsible for changes in the deformation behavior when Indiana limestone is deformed in a chemically active environment, or not the main mechanism, for two reasons. First, the dissolution of the limestone occurring should lead to a minor increase of the pH (*Garrels and Christ, 1965*; *Plummer et al. 1978*), which can decrease calcite solubility (*Dunning et al., 1994; Bergsaker et al. 2016*) leading to crack tip strengthening and potentially increasing the frictional strength of the rock. The effect of pH should increase as the duration of the experiments increases and thus dissolution of the limestone is greater. Second, it does not explain why the time-dependency of deformation is greatest at 30 MPa (see Figure 2.12), especially since microcrack anisotropy is lower at the higher confining pressure (Figure 4.2). While stress-corrosion cracking may play a role in

the deformation response under water saturated conditions, it does not offer a mechanism for explaining the greater weakening observed at effective pressures of 30 MPa.

4.2: Role of Grain-Contacts and Water-Weakening

At all conditions, the effective pressure applied appears to play the greatest role in both the observed laboratory data and the resulting microstructures. Microcracks and crystal plastic mechanisms such as crystal twinning, under dry conditions, are responsible for the observed deformation response in Indiana limestone. Under these conditions, both of these micromechanisms should be dominantly dependent on the applied stress and strain during each experiment, and the limestone behavior should be essentially time-independent.

The addition of water has an interesting effect. The P* value is reduced by nearly 1/3 when deformed with deionized water present, as has been observed in other works with carbonate grainstones (*Baud et al., 2009*). Increases in microcrack density and pressure solution indentation were observed at all conditions when Indiana limestone was saturated with water. However, only the experiments at 30 MPa effective pressure show more significant weakening relative to the dry deformations at the same effective pressure. For the fastest strain rate, the data indicates that its strength is nearly that of deformation experiments conducted under

dry conditions at this same effective stress. This could be due to the effect of rapid loading leading to localized pore pressure increases (*Rutter, 1972*).

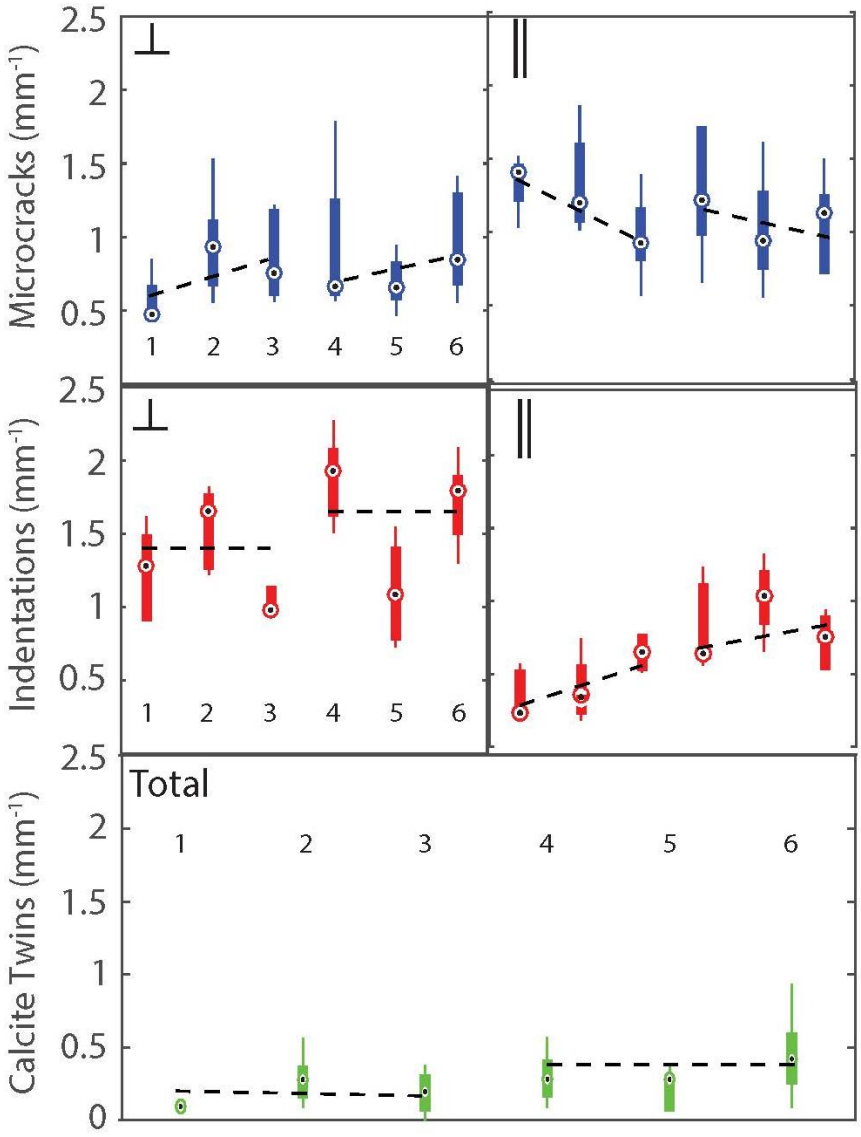

Figure 4.3: Data for microcrack (blue), pressure solution indentation (red), and calcite twinning (green) oriented parallel (||) and perpendicular (⊥) to the maximum principal stress. Twins measurements are an average of measurements in both orientations. The degree of pressure solution indentation increases as the confining pressure is raised. Indentation increases in both the directions measured parallel and perpendicular to the maximum principal stress. 1, 2, and 3 are experiments conducted at 10 MPa and strain rates of $1.5x10^{-4}$, $1.5x10^{-5}$, and $1.5x10^{-6}$ s^{-1} respectively, and 4, 5, 6 are experiments conducted at 30 MPa with strain rates of $1.5x10^{-4}$, $1.5x10^{-5}$, and $1.5x10^{-6}$ s^{-1} respectively.

Examination of the microstructures suggests another possibility. The density of microcracks observed at the $1.5x10^{-4}$ s^{-1} strain rate for both water saturated

conditions are fairly high (Figure 4.3). Microstructural analysis at this rapid strain rate suggest the effects of chemical dissolution, and thus stress corrosion and pressure solution indentation, are minimized and deformation is essentially time-independent (i.e. only the applied pressure is relevant). Unlike for the low effective pressure experiments, when mechanical loading rate is decreased at an effective pressure of 30 MPa and when saturated with water, the strength of the limestone appears to be reduced. Since there is not a significant variation in microcrack density between the two confining pressures (Figure 4.3), this indicates that pressure solution indentation is responsible for the observed water weakening with strain rate reduction.

The observed weakening of Indiana limestone only at specific confining pressures bears further discussion. Since microcrack density under water saturated conditions does is not significantly affected by the change in the effective pressure (possibly due to increased pressure impeding the opening of microcracks) (Figure 4.1), this can be ruled out as an explanation. Calcite twinning can also be ruled out, as the density remains low at all conditions (Figure 4.2). This only leaves intergranular pressure solution as a deformation mechanism.

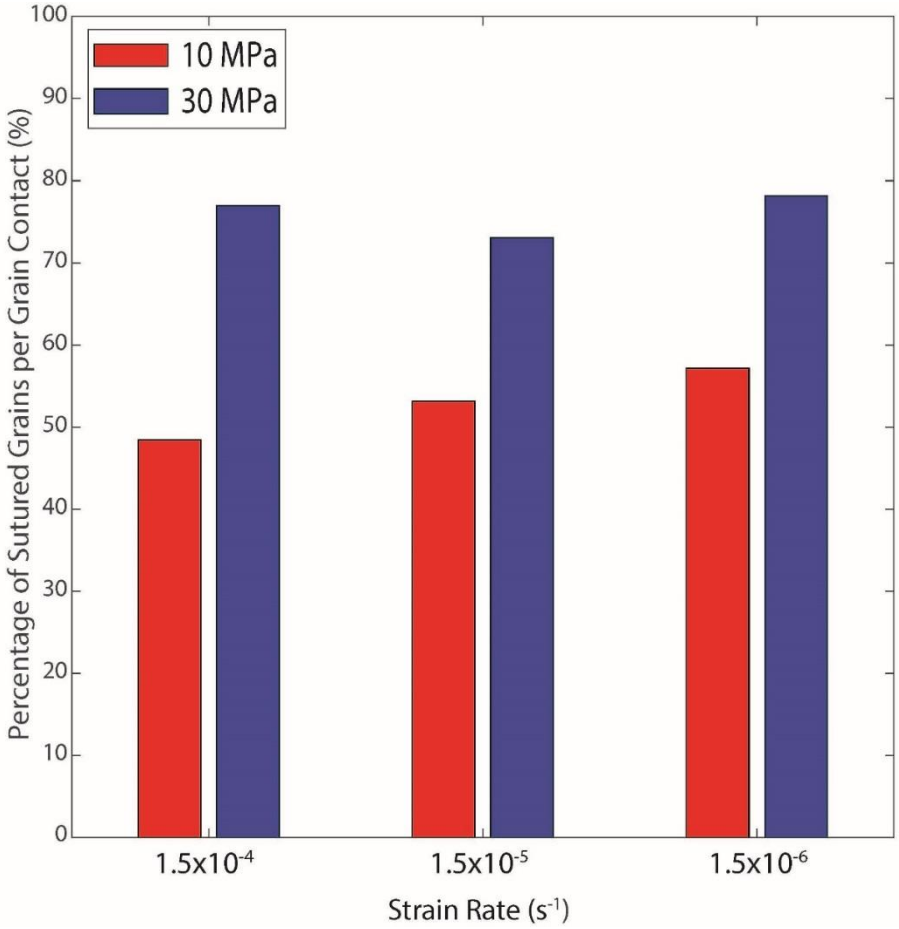

Figure 4.4: Percentage of grain contacts with pressure solution indentation oriented perpendicular (⊥) to the maximum principal stress.

Previous research by *Zhang and Spiers (2005)* showed that for crushed limestone saturated with calcium carbonate solution, intergranular pressure solution was the dominant mechanism of deformation and the compaction by pressure solution was strongly dependent on the applied normal stress. The percentage of the total grain contacts that display pressure solution indentation is plotted in Figure 4.4. It can be seen that the percentage of grains displaying indentation increases as much as 20-30% with the increase of effective pressure from 10 to 30 MPa. These results suggest that the reduction of the grain-crushing pressure (P*) and the pressure-dependent water-

weakening of Indiana limestone are a result of increased intergranular pressure solution.

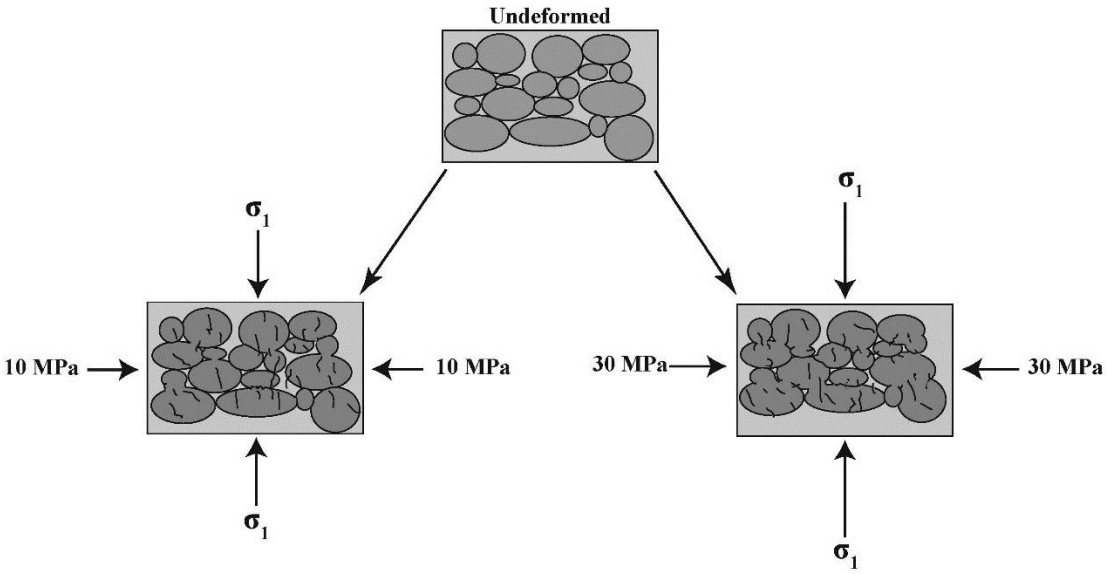

Figure 4.5: Diagram of the effect of confining pressure on enhancing dissolution at grain boundary contacts. The role of the applied stress during each experiments controls whether the deformation behavior is controlled by microcracking or intergranular pressure solution.

4.3: Water-Weakening in Carbonate Rocks

Our results suggest that the water-weakening of limestones and other carbonate rocks is not a simple process to predict, even with a relatively homogenous material like Indiana limestone. Research conducted by *Boozer et al. (1963)* suggested Indiana limestone would experience a reduction of strength of ~20% in the presence of water, while research conducted by *Lisabeth and Zhu (2015)* showed a reduction of strength of more than 50% for Indiana limestone saturated with water. Our results suggest limited water-weakening occurring for Indiana limestone, and only under certain pressure conditions. This discrepancy with the same limestone is noticeable and bears further discussion.

One possibility that has been discussed (*Rutter, 1972*) is the role of grain size. The chemical effect on calcite-rich rocks may be dependent on the total surface area available for dissolution in the presence of water. *Boozer et al. (1963)* also suggested water weakening in limestone may occur due to the reduction of surface energy in calcite through interaction of water and the grain surface. *Heard* (1963) showed that for Solnhofen limestone of 1.3% porosity water-weakening was negligible, and behavior was largely the same between dry and water saturated deformations. For Solnhofen limestone of ~5% porosity, *Rutter (1972)* demonstrated a minor strength reduction when saturated with water. Water showed little effect on the coarse-grained Carrara marble both at room temperature (*Rutter, 1972*) and at elevated temperatures (*de Bresser, 2005*). The largest degree of water weakening has been observed in extremely-fine grained chalks, often with a more than 50% strength reduction compared to dry experiments (*Homand and Shao, 2000*; *Risnes et al., 2005*). However this does not offer an explanation as to the fact that the percentage of strength reduction due to water-weakening reported for Indiana limestone has been so variable.

Another possibility is the relation of porosity in carbonate rocks. Low porosity marble experiences negligible weakening in the presence of water, while highly porous chalks experience significant weakening (*de Bresser, 2005*; *Risnes et al., 2005).* Given the relationships of porosity and grain size with water-weakening in carbonate rocks, the greatest weakening in should occur in fine grained rocks with high porosities, such as chalk (*Rutter, 1972*). Such would be a reasonable explanation for the subsidence observed in the case of the aforementioned Ekofisk chalk

following fluid injection (*Sylite et al., 1999*). However, this does not adequately explain our results either.

This work suggests another factor may be in play when discussing water-weakening in limestones and other carbonate rocks. Most work regarding the effect of solubility on subcritical crack propagation and pressure solution in calcite (*Henry et al. 1977*; *Røyne et al., 2011; Zhang and Spiers, 2005; Zhang et al., 2010; Croizé et al., 2010*) has focused on observations of fine-grained calcite sediment or single crystals when examining chemical weakening in carbonate rocks. However, limestones and other porous carbonates are not as homogenous as these materials. The role of water-weakening has never been investigated previously with regard to carbonate fabric and texture.

Analyses of Indiana limestone have shown that the grain size and porosity of Indiana limestone are relatively similar to observations made in this study (*Churcher et al., 1991*; *Zhu et al., 2010*). This explains why the mechanical behavior is qualitatively similar to that observed in previous studies under dry conditions (*Vajdova et al., 2004*). However the chemical effects of water and fluid-assisted deformation are dependent on the number of grain-to-grain contacts (*Rutter, 1972*). Comparison of our petrophysical data with that of previous studies of the fabric of Indiana limestone reveals a wide disparity between the observed grain/matrix distributions in Indiana limestone (*Hugman and Friedman, 1979*). This suggests water-weakening may vary significantly depending on the fabric heterogeneity in a limestone.

A reasonable explanation for the observation that water only shows a noticeable weakening effect and apparent time- and pressure-dependence is that at the lower confining pressure the number of grain contacts is relatively low. If the grains are not in contact, deformation will occur primarily by the nucleation and growth of microcracks, mostly within the calcite cement, which is generally time-independent within the time ranges here. As confining pressure is increased however, grains come into contact with one another, and pressure solution becomes a more significant factor in driving the compaction observed. This could explain why during hydrostatic deformation the bulk moduli remain relatively the same, while the initiation of pore collapse and grain-crushing occurs at much lower confining pressures. At 30 MPa effective pressure, there is a trend of decreasing microcracks while simultaneously increased pressure solution indentation (Table 3.3) as strain rate-decreases. This is absent in limestones deformed with an effective pressure of 10 MPa. These results suggest carbonate fabric is the third component that affects the water-weakening in limestones besides grain size and porosity.

4.4: Geologic Implications

Observations here have indicated that water-weakening in limestone in limestone does occur, as has been previously noted. However, the chemical effects on deformation of calcite-rich rocks are not as simple as can be predicted for homogenous materials. These result suggest that the water-weakening in an oolitic limestone will be significantly affected by the local pressure conditions of a formation.

The removal or injection of fluids into carbonate reservoirs will alter the local stress field by lowering the effective stress applied. These changes are relatively predictable. The chemical effects are not as predictable as numerical models and experimental results would suggest. Indeed, chemical weakening of carbonates may depend strongly on the number of grain contacts at a given pressure condition. In the case of a material like chalk, the effect of calcite dissolution may be relatively predictable with its natural homogeneity and fine grain size, and pressure solution compaction will occur as in the case of the Ekofisk chalk (*Sylte et al., 1999*). For carbonate rocks such as the heterogeneous limestones tested in this study, water-weakening and time-dependence will likely also vary based on the texture and local stress conditions.

This has important implications for a number of reasons. Fluid injection is a common practice in many industrial and scientific applications. Carbonate reservoirs host resources such as hydrocarbons and freshwater. Any prospective fluid injection into one of these reservoirs should take into account the texture and fabric of the carbonate rock as well, as the chemical-weakening of the material may be depend on the local stress conditions and degree of grain-grain contacts. Carbonate rocks are also known to host numerous faults (*Han et al., 2007*) that can be affected by fluid weakening processes such as fault lubrication (*Di Toro et al., 2011*) and thermal decomposition (*Han et al., 2010*). These results may allow for a better prediction of the likelihood of fault slip in carbonate rocks.

Carbonate rocks are also being considered as a potential sink for in-situ geologic sequestration of CO_2 (*Benson and Cole, 2008*). However, in-situ

sequestration of CO_2 in carbonate rocks is considered hazardous due to the solubility increase with CO_2-rich fluids (*Korsnes et al., 2008*; *Pokrovsky et al., 2009*). However, the effects of chemically-induced weakening may not be as significant as previously predicted. For carbonate rocks such as chalk, CO_2 injection may lead to significant reservoir compaction (*Hellmann et al., 2002*). However, for limestones and other carbonate rocks with lower porosities and higher grain sizes, dissolution-enhanced compaction may be less of a concern for CO_2 sequestration.

Chapter 5: Summary and Future Work

A series of triaxial deformation experiments were conducted on Indiana limestone. Under dry conditions, the mechanical behavior of an oolitic limestone is controlled dominantly by the confinement applied during deformation. Their deformation response is essentially time-independent, and natural petrophysical variations may obscure any potential variations with changes to the mechanical loading rate. When saturated with water, the pressure at which grain-crushing and pore collapse was initiated in Indiana limestone was significantly reduced. While only minor weakening occurred at lower effective pressures, at greater effective pressures Indiana limestone showed moderate water-weakening as well as time-dependence.

Quantitative microstructural and petrophysical analysis was performed on thin sections of deformed Indiana limestone to characterize the micromechanics of deformation at different conditions in an oolitic limestone. Comparison of petrophysical observations in previous studies suggests that while Indiana limestone is chemically homogenous, the texture and fabric are fairly variable, which may affect the ability to predict deformation behavior. Concurrent with previous work, microcracking occurred largely within the calcite cement under dry conditions. Under water saturated conditions, the degree of microcracks observed increased noticeably, implying fluid-assisted subcritical cracking was occurring. Calcite twinning was relatively small, with a majority of twins being observed in the more spherical grains rather than elongate grains or the cement matrix. The degree of grain connections and pressure solution features increased noticeably when saturated with water. However,

grain indentations appear to have been controlled strongly by the effective confining pressure conditions of each limestone.

This study raises a number of questions regarding the role of chemo-mechanical weakening plays, not only in limestone but in a variety of carbonate rocks. Future work from this study could focus on:

1) What role does cementation play in changing the behavior of limestones under dry and water-saturated conditions? Changes in the volume percentage of cement has been shown to significantly affect the behavior of sandstones and clastic rocks, but there is a scarcity of data regarding how this affects observed mechanical behavior in porous carbonate rocks.
2) Do fluid-assisted deformation mechanisms occur more or less easily in calcite spar versus micrite coated grain in carbonate grainstones? Previous studies of these mechanisms have focus prominently on single crystals of calcite or homogenous materials such as chalk.
3) Water-weakening and time-dependent deformation in carbonate rocks have not been adequately explored from the perspective of grain size and porosity. Further work to quantify the role each of these plays in the degree of weakening observed would be of significant value to any future reservoir injection projects in carbonate rocks.
4) Previous work has looked at the effect CO_2 has on the deformation behavior of porous limestones (*Grgic, 2011, Bemer et al., 2016*). Very little weakening was found at the conditions used, with the most noticeable chemical weakening only occurring under greater confining pressures within the

semibrittle and ductile deformation regimes. These findings are similar to this work regarding the role of chemical weakening and pressure, but with water as a pore fluid. This is at odds with work that predict significant compaction due to high CO_2 fluid presence in chalk (*Hellmann et al., 2002*; *Korsnes et al., 2008*). Further work should focus on whether predictions of significant reservoir compaction in chalk are in fact applicable to less porous limestones.

Appendix A: Deformation Apparatus

Samples were deformed in a conventional triaxial deformation apparatus (NER AutoLab 1500) (Figures A.1 and A.2). It consists of a single pressure vessel with a hydraulic piston inside for axial deformation experiments, an external furnace for progressive temperature changes, and two pore pressure intensifiers for controlling sample pore pressure. The hydraulic piston and steel end caps have a stiffness of 4.4×10^{-7} N/m for 1 inch samples and a stiffness of 2×10^{-7} N/m for 0.725 inch samples. Samples are loaded with two end-caps (Figure 2.3) on top and bottom through which pore fluid and pressure is controlled by upstream and downstream intensifiers (Figure 2.4). Pressure transducers above and below the assembled sample allow for in-situ pore pressure measurements to be taken during experiments. Mineral oil is used as the confining pressure medium. Confining pressure and pore pressure transducers have ranges of 0-137.9 MPa, while the differential pressure transducer has a range of 0-206.84 MPa for 1 inch diameter samples. Piston displacement is measured by a linear-vertical-displacement-transducer (LVDT). Axial stress is measured by an internal load cell. Sample strain is measured with electrical resistance strain gages applied to the surface and connected to the base plug for the pressure vessel.

Figure A.1: NER AutoLab 1500. Triaxial deformation apparatus used in this study, located in the Rock Physics Lab at the University of Maryland in College Park.

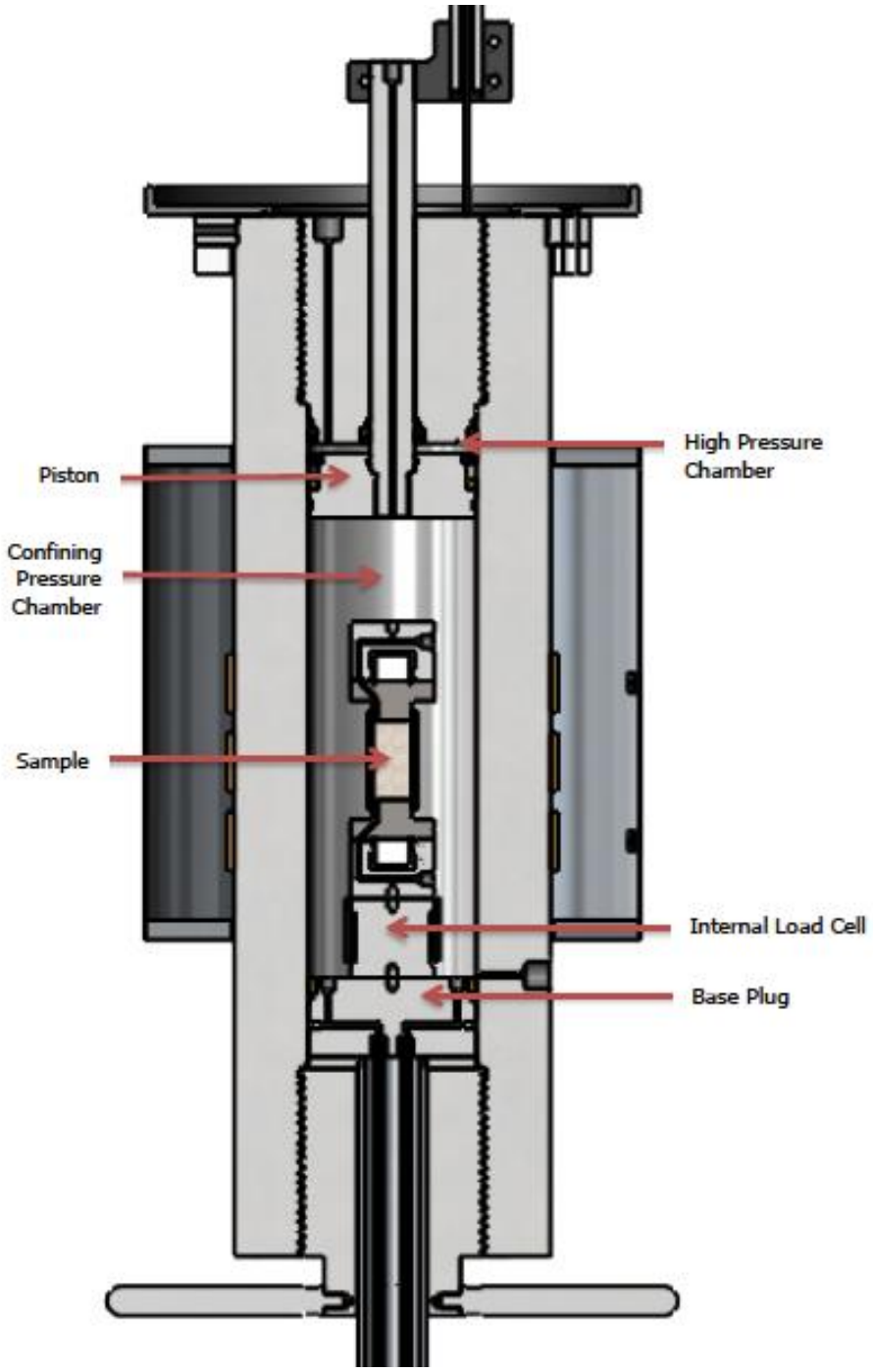

Figure A.2: Schematic of experimental setup in pressure vessel, adapted from manual for NER AutoLab 1500.

Appendix B: Thin-Section Preparation and Microscope

Deformed Indiana limestone samples were dried for 24 hours following deformation. These samples were then epoxy impregnated before being cut parallel to the maximum compressive stress (σ_1) or vertically along all cylindrical samples. The cut samples were then sent out to have 30 μm thick thin-sections made from each thin section.

Thin-sections were analyzed using with a Nikon Eclipse LV100n POL petrographic microscope. The microscope feature objectives with magnification of 3.5X, 5X, 10X, 20X, and 50X magnification. All photos have been taken with a MicroPublisher 5.0 RTV camera.

Figure A.3: Image of Nikon Eclipse LV100n POL petrographic microscope used in this study.

Appendix C: Total Microstructure Data

Microcracking:

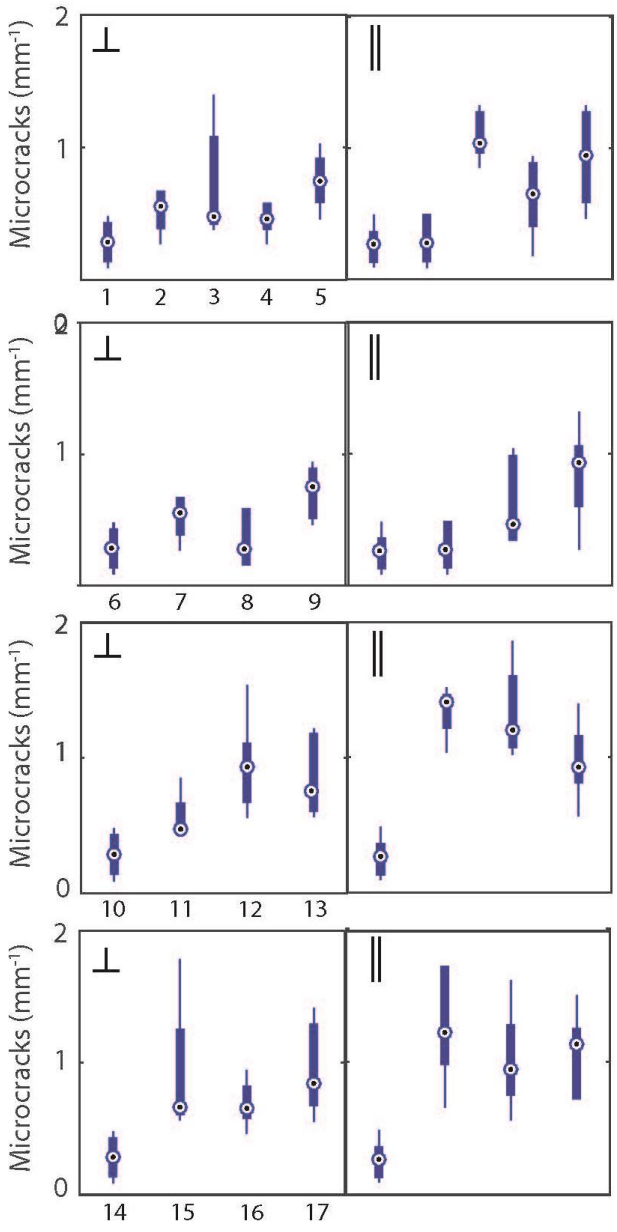

Figure A.4: Total microcracks oriented perpendicular (⊥) to σ_1 and lines perpendicular (‖) to σ_1. Microcrack incidents are recorded as per mm (mm^{-1}). 1) Undeformed; 2) Hydrostatic; 3) 10 MPa, Dry, $1.5x10^{-5}$ s^{-1}; 4) 30 MPa, Dry, $1.5x10^{-5}$ s^{-1}; 5) 50 MPa, Dry, $1.5x10^{-5}$ s^{-1}; 6) Undeformed; 7) Hydrostatic; 8) 30 MPa, Dry, $1.5x10^{-6}$ s^{-1}; 9) 50 MPa, Dry, $1.5x10^{-6}$ s^{-1}; 10) Undeformed; 11) 10 MPa, Wet, $1.5x10^{-4}$ s^{-1}; 12) 10 MPa, Wet, $1.5x10^{-5}$ s^{-1}; 13) 10 MPa, Wet, $1.5x10^{-6}$ s^{-1}; 14) Undeformed; 15) 30 MPa, Wet, $1.5x10^{-4}$ s^{-1}; 16) 30 MPa, Wet, $1.5x10^{-5}$ s^{-1}; 17) 30 MPa, Wet, $1.5x10^{-6}$ s^{-1}.

Grain-Grain Contacts:

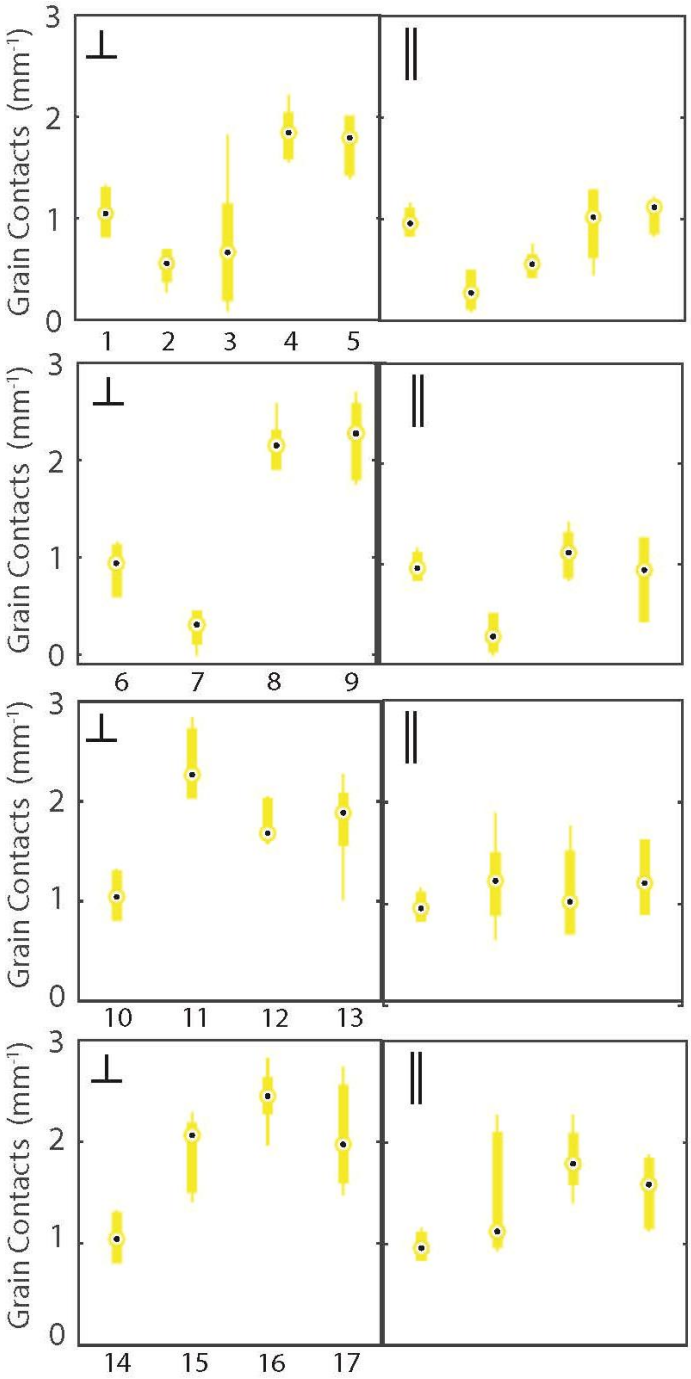

Figure A.5: Total grain-grain contacts oriented perpendicular (⊥) to σ_1 and lines perpendicular (‖) to σ_1. Contact incidents are recorded as per mm (mm^{-1}). 1) Undeformed; 2) Hydrostatic; 3) 10 MPa, Dry, $1.5x10^{-5}$ s^{-1}; 4) 30 MPa, Dry, $1.5x10^{-5}$ s^{-1}; 5) 50 MPa, Dry, $1.5x10^{-5}$ s^{-1}; 6) Undeformed; 7) Hydrostatic; 8) 30 MPa, Dry, $1.5x10^{-6}$ s^{-1}; 9) 50 MPa, Dry, $1.5x10^{-6}$ s^{-1}; 10) Undeformed; 11) 10 MPa, Wet, $1.5x10^{-4}$ s^{-1}; 12) 10 MPa, Wet, $1.5x10^{-5}$ s^{-1}; 13) 10 MPa, Wet, $1.5x10^{-6}$ s^{-1}; 14) Undeformed; 15) 30 MPa, Wet, $1.5x10^{-4}$ s^{-1}; 16) 30 MPa, Wet, $1.5x10^{-5}$ s^{-1}; 17) 30 MPa, Wet, $1.5x10^{-6}$ s^{-1}.

Pressure Solution Indentations:

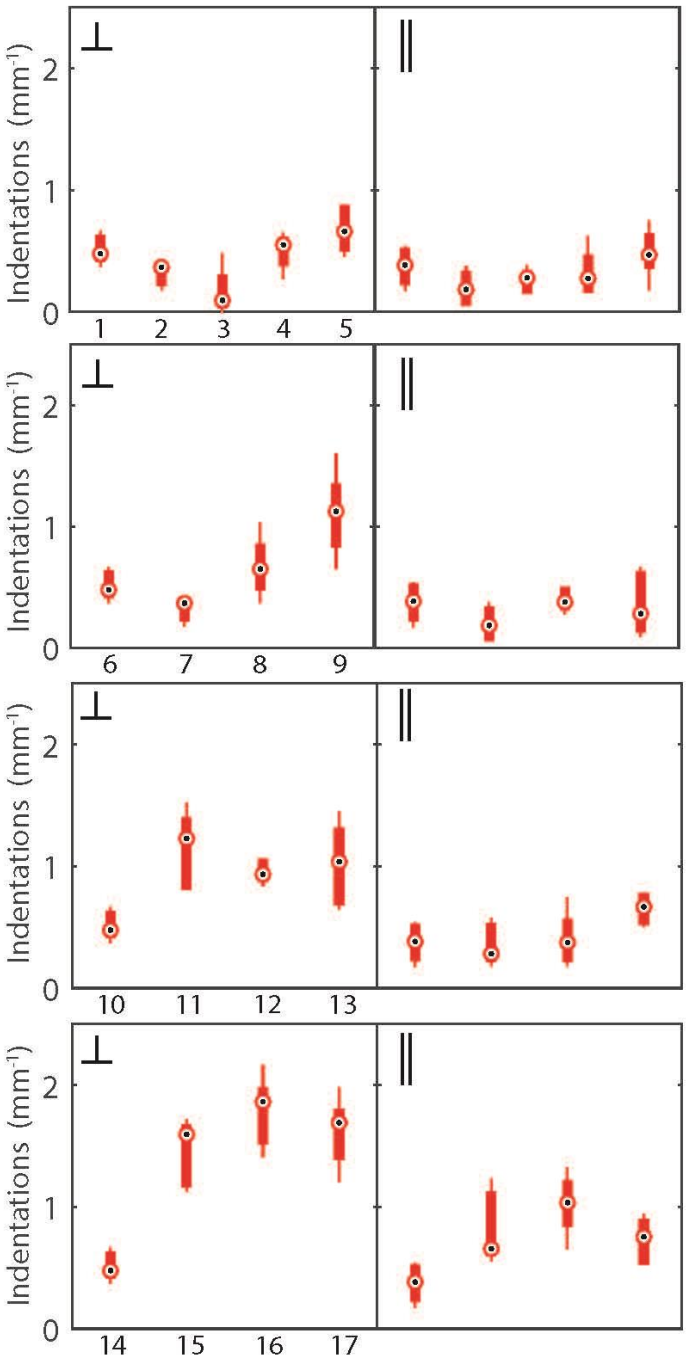

Figure A.6: Total pressure solution indentation oriented perpendicular (⊥) to σ_1 and lines perpendicular (‖) to σ_1. Contact incidents are recorded as per mm (mm^{-1}). 1) Undeformed; 2) Hydrostatic; 3) 10 MPa, Dry, $1.5x10^{-5}$ s^{-1}; 4) 30 MPa, Dry, $1.5x10^{-5}$ s^{-1}; 5) 50 MPa, Dry, $1.5x10^{-5}$ s^{-1}; 6) Undeformed; 7) Hydrostatic; 8) 30 MPa, Dry, $1.5x10^{-6}$ s^{-1}; 9) 50 MPa, Dry, $1.5x10^{-6}$ s^{-1}; 10) Undeformed; 11) 10 MPa, Wet, $1.5x10^{-4}$ s^{-1}; 12) 10 MPa, Wet, $1.5x10^{-5}$ s^{-1}; 13) 10 MPa, Wet, $1.5x10^{-6}$ s^{-1}; 14) Undeformed; 15) 30 MPa, Wet, $1.5x10^{-4}$ s^{-1}; 16) 30 MPa, Wet, $1.5x10^{-5}$ s^{-1}; 17) 30 MPa, Wet, $1.5x10^{-6}$ s^{-1}.

Calcite Twins:

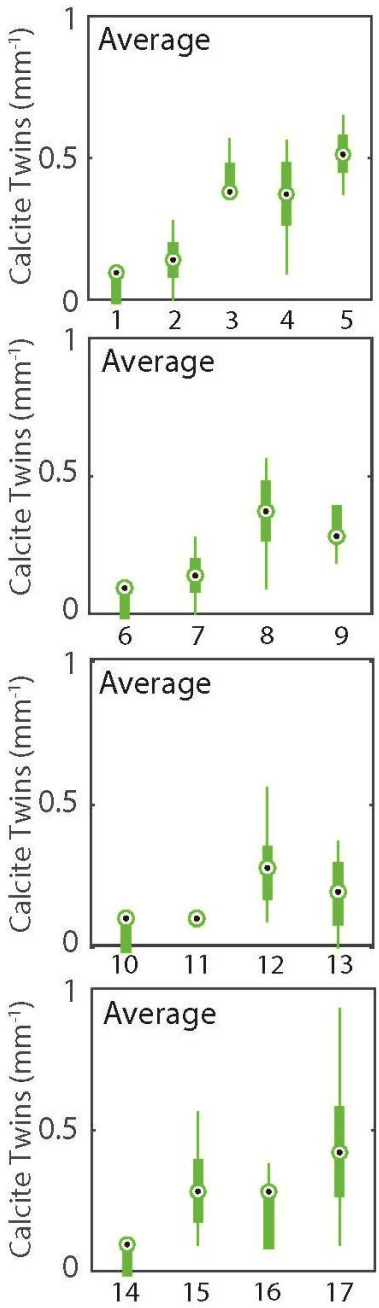

Figure A.7: Calcite twins measured by lines parallel to σ_1 and lines perpendicular to σ_1. Data is reported as the average of the two orientations. Twin incidents are recorded as per mm (mm^{-1}). 1) Undeformed; 2) Hydrostatic; 3) 10 MPa, Dry, $1.5x10^{-5}$ s^{-1}; 4) 30 MPa, Dry, $1.5x10^{-5}$ s^{-1}; 5) 50 MPa, Dry, $1.5x10^{-5}$ s^{-1}; 6) Undeformed; 7) Hydrostatic; 8) 30 MPa, Dry, $1.5x10^{-6}$ s^{-1}; 9) 50 MPa, Dry, $1.5x10^{-6}$ s^{-1}; 10) Undeformed; 11) 10 MPa, Wet, $1.5x10^{-4}$ s^{-1}; 12) 10 MPa, Wet, $1.5x10^{-5}$ s^{-1}; 13) 10 MPa, Wet, $1.5x10^{-6}$ s^{-1}; 14) Undeformed; 15) 30 MPa, Wet, $1.5x10^{-4}$ s^{-1}; 16) 30 MPa, Wet, $1.5x10^{-5}$ s^{-1}; 17) 30 MPa, Wet, $1.5x10^{-6}$ s^{-1}.

Appendix D: Israeli Limestone Water Saturated Deformations

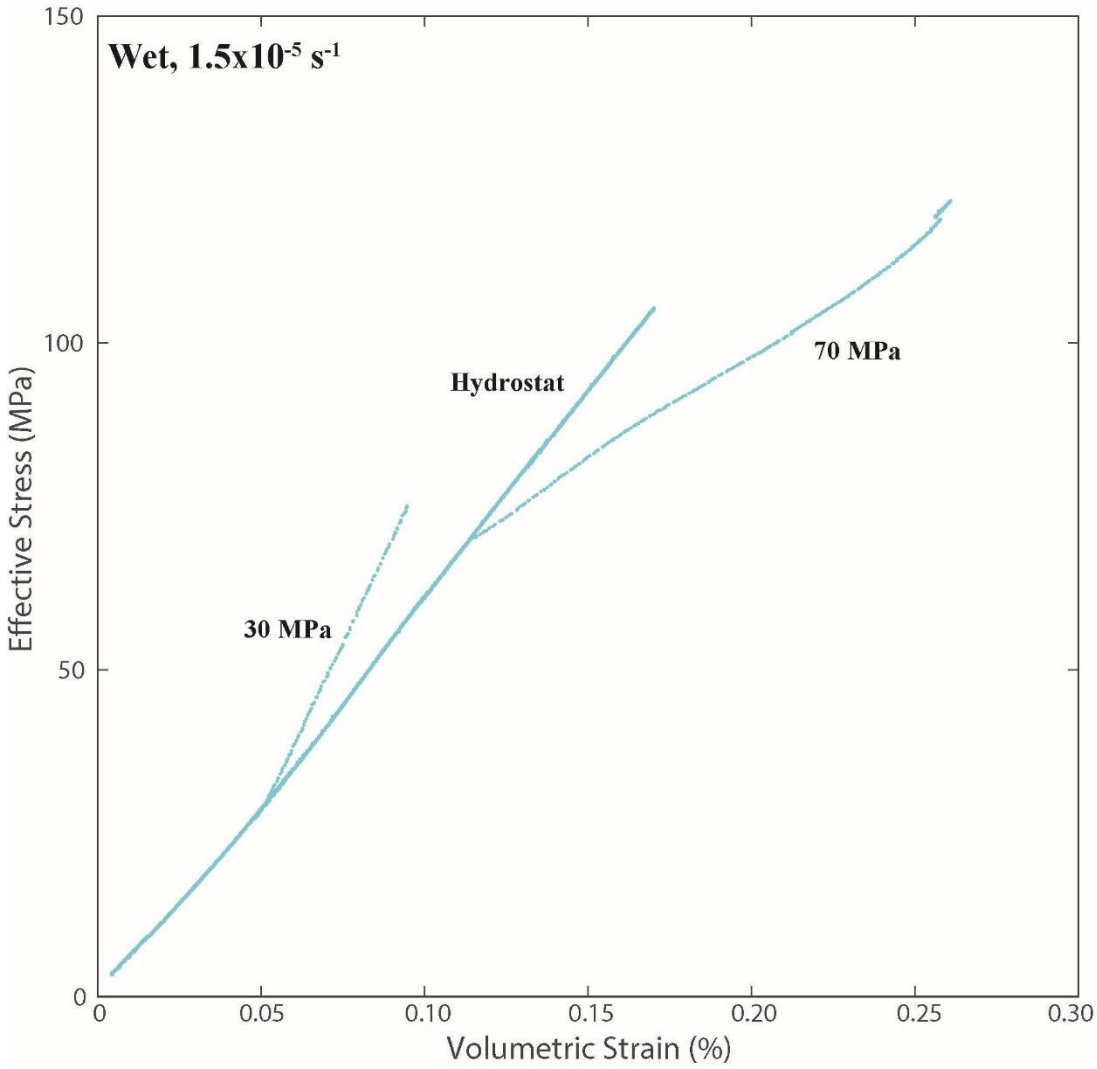

Figure A.8: Volumetric strain data for all deformations with Israeli limestone under water saturated conditions.

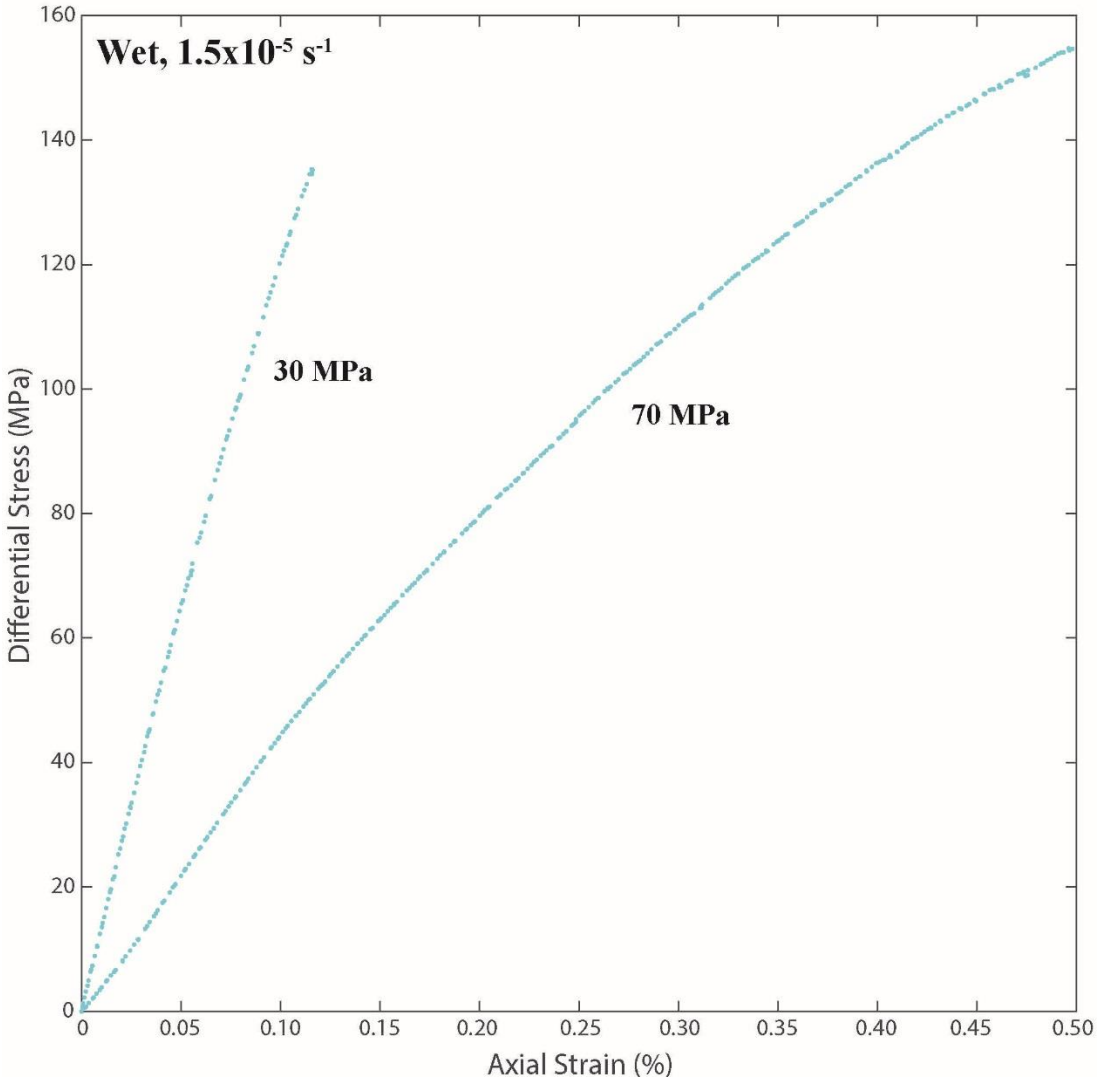

Figure A.9: Axial strain data for all deformations with Israeli limestone under water saturated conditions.

Mechanical data for deformation of the Israeli limestone are plotted in Figure 2.8 and 2.9. Unlike the Indiana limestone, the grain-crushing pressure was not achieved within the effective pressure range of the conducted hydrostatic deformation. At an effective pressure of 30 MPa the limestone deformed predominately by brittle failure. The rock experienced dilatant behavior following the onset of axial deformation, before localized failure occurred through the coalescence of microcracks. At the higher effective pressure of 70 MPa, the limestone instead experienced a brief period of shear enhanced compaction prior to deformation, again

displaying localized failure along a plane of weakness. It seems that within the confining pressures tested, there is a shift from brittle dilatant behavior to brief distributed deformation, though the rock is able to accommodate very little axial strain before yielding.

Appendix E: Effect of Petrophysics

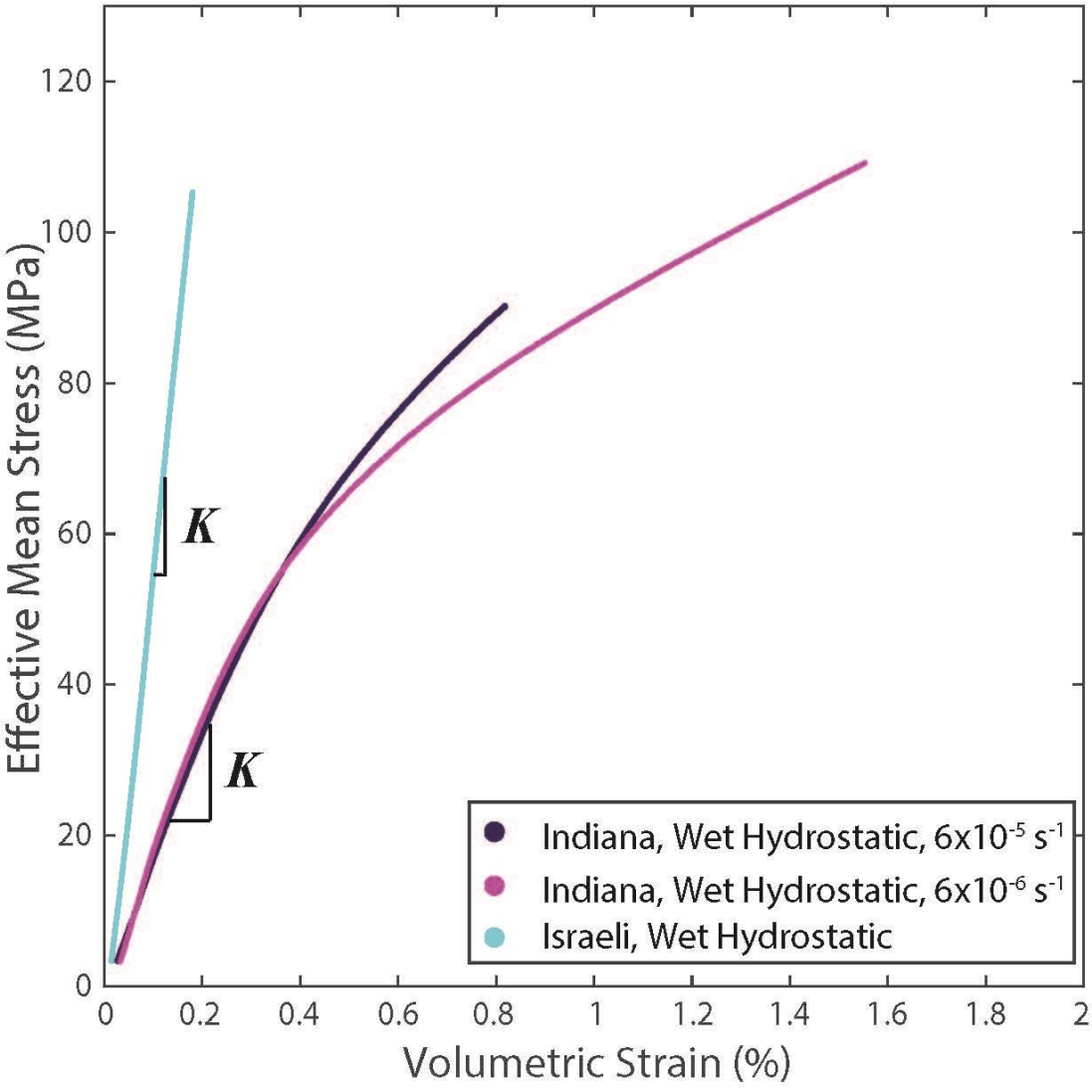

Figure A.10: Volumetric strains of Indiana limestone and the Israeli limestone compared. *K*, or the bulk modulus, is significantly greater for the Israeli limestone than in the Indiana limestone. This can be attributed to the differences in initial porosity between the two limestones.

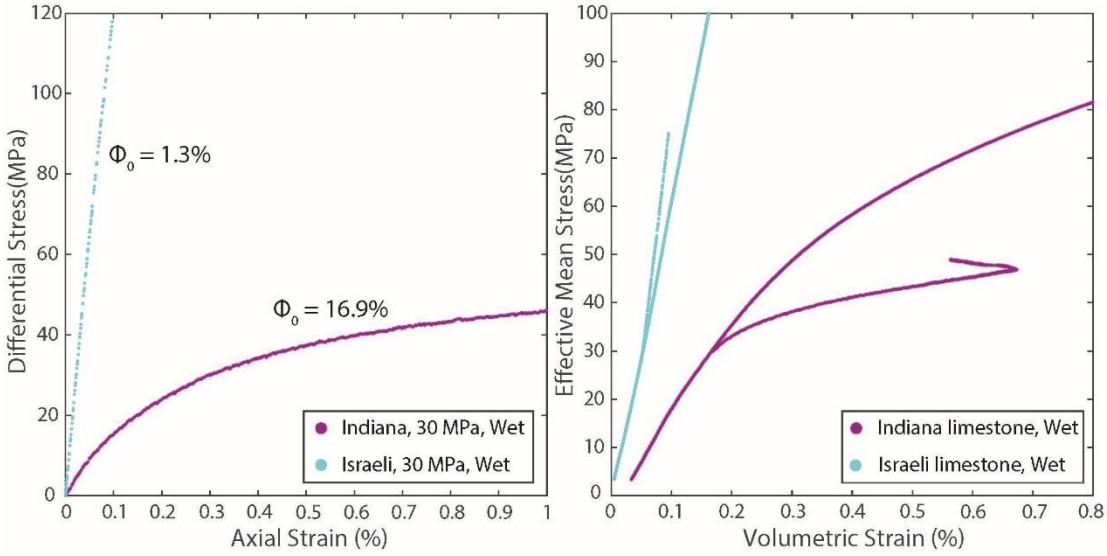

Figure A.11: Axial and volumetric strain data for deformations conducted at effective pressures of 30 MPa.

Deformation experiments demonstrate a significant variation in the mechanical behavior of each limestone (Figure 2.14 and 2.15). Fluid-saturated deformations under both hydrostatic and 30 MPa effective pressure conditions suggest the role the petrophysical properties play in determining the elastic and inelastic behavior in carbonate rocks is significant.

Limestone	***Ø₀***	***P* (Dry)***	***P* (Wet)***	***Referenced Work***
Israeli Limestone	0.016			*This Study*
Solnhofen Limestone	0.03	550		*Zhu et al., 2010*
Tavel Limestone	0.104	290		*Vajdova et al., 2004*
Tavel Limestone	0.136	180		*Zhu et al., 2010*
Indiana Limestone	0.156	60		*Vajdova et al., 2004*
Indiana Limestone	0.16	61	42	*This Study*
Chavigny Limestone	0.174	140		*Fabre and Gustkiewicz, 1997*
Lavoux Limestone	0.218	30		*Fabre and Gustkiewicz, 1997*

Cordoba Cream Limestone	0.25	41.4		*Mowar et al., 1994*
Estillaides Limestone	0.27	30		*Dautriat et al., 2009*
Majella Limestone	0.3	37.5	26.5	*Baud et al., 2009*
Saint Maximin Limestone	0.37	17	13	*Baud et al., 2009*

Table A.1: Data for the initial porosity and P* values reported in this and previous studies of limestones under dry and water saturated conditions. Φ_0 represents the limestones initial porosity prior to compaction.

Table A.1 shows that there is a trend of decreasing onset of grain crushing pressure with increasing confining pressure. *Vajdova et al. (2004)* previously noted that the relationship with the P* value for porous carbonate rocks is related to the grain size and porosity by

$$P^* \propto (\emptyset_0 * R)^{-0.7} \quad \text{(A.1)}$$

where $\emptyset_0$ is the initial porosity and R is the average grain radius. Using this formula, and estimating the average grain size of the fossiliferous grains and the micritic matrix to be ~50 and 5 μm respectively, a range of 240 to 1200 MPa can be predicted as the range of the P* value for the Israeli limestone under both dry and water saturated conditions. The values for the reduction of the P* value from dry and water conditions suggests that inelastic compression can be initiated at anywhere between 1/10 and 1/3 of the effective pressure when saturated with water. Values for a number of hydrostatic compaction experiments are plotted in Figure A.12.

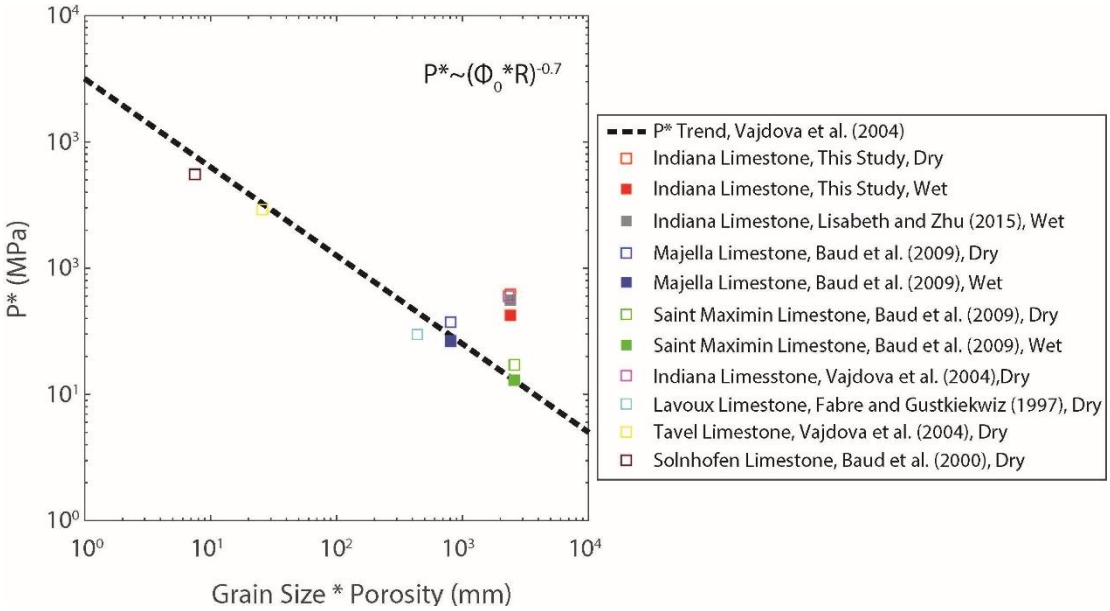

Figure A.12: Trend found in *Vajdova et al. (2004)* shows inelastic compressibility and pore collapse occurs at lower effective stresses as porosity is decreased.

While the grain-crushing pressure of Indiana limestone was achieved at ~42 MPa, the onset of grain-crushing and pore collapse was not achieved in the Israeli limestone, even up to an effective pressure of 100 MPa (Figure 2.14). Likewise, the bulk moduli of the lower porosity Israeli limestone is more than 3 times that of the Israeli limestone (64.2 GPa versus 19.5 GPa). This is in line with the expected trend of decreasing compressibility *B* as the porosity is decreases, as most of the volumetric strain is accommodated by pore compaction under hydrostatic conditions.

When axially deformed, the inelastic behavior of the limestones is demonstrably different at the same effective pressures (Figure 2.15). While the higher porosity Indiana limestone achieves inelastic compaction upon the application of differential stress, the Israeli limestone experiences limited compaction, with a significantly greater Young's modulus. Indeed, brittle failure and macroscopic fracturing along a slip plane was achieved for both deformations of the Israeli

limestone, while all the Indiana limestone deformations exhibited predominantly semibrittle behavior at all conditions (see Figure 2.7).

Though both are limestones, this is not enough of a predictor of their mechanical and chemical behavior. Other petrophysical properties such as grain size, initial porosity, and fabric can each have a significant effect on both their mechanical behavior (*Gueguen and Bouteca, 2004*). Compressibility and the onset of inelastic deformation will increase dramatically as the porosity increases in carbonate rocks (*Zhu et al., 2010*). This relationship is similar to that of the effect of grain size on deformation behavior, but can be highly variable.

Additionally, the distribution of porosity in sedimentary carbonate rocks can significantly affect the heterogeneity of the rock's response to deviatoric stress (*Zhu et al., 2010; Ji et al., 2012*). In the case of the Israeli limestone, porosity primarily occurs in the micritic matrix, with roughly equant pores and few pre-existing microcracks. For the more porous limestone, porosity is divided between larger macropores surrounded by smaller micropores. This difference in distribution of the limestones' porosity affects both the mode of inelastic deformation and micromechanisms of pore collapse (*Baud et al., 2009, 2014; Vajdova et al., 2012*). Thus even minor petrophysical properties play an important role in carbonate rocks and cannot be disregarded when attempting to predict the hydromechanical properties.

Bibliography

Atkinson, B.K., 1984. Subcritical crack growth in geological materials. *Journal of Geophysical Research: Solid Earth*, *89*(B6), pp.4077-4114.

Atkinson, B.K. and Meredith, P.G., 1981. Stress corrosion cracking of quartz: a note on the influence of chemical environment. *Tectonophysics*, *77*(1-2), pp.T1-T11.

Barber, D.J. and Wenk, H.R., 1979. Deformation twinning in calcite, dolomite, and other rhombohedral carbonates. *Physics and Chemistry of Minerals*, *5*(2), pp.141-165.

Bassinot, F., Marsters, J.C., Mayer, L.A. and Wilkens, R.H., 1993. Variations of porosity in calcareous sediments from the Ontong Java Plateau.

Baud, P., Schubnel, A. and Wong, T.F., 2000a. Dilatancy, compaction, and failure mode in Solnhofen limestone. *Journal of Geophysical Research: Solid Earth*, *105*(B8), pp.19289-19303.

Baud, P., Vinciguerra, S., David, C., Cavallo, A., Walker, E. and Reuschlé, T., 2009. Compaction and failure in high porosity carbonates: Mechanical data and microstructural observations. In *Rock Physics and Natural Hazards* (pp. 869-898). Birkhäuser Basel.

Baud, P., Wong, T.F. and Zhu, W., 2014. Effects of porosity and crack density on the compressive strength of rocks. *International Journal of Rock Mechanics and Mining Sciences*, *67*, pp.202-211.

Baud, P., Zhu, W., Wong, T.F., 2000b. Failure mode and weakening effect of water on sandstone. *Journal of geophysical research*, *105*(B7), pp.16371-16389.

Bemer, E., Nguyen, M.T., Dautriat, J., Adelinet, M., Fleury, M. and Youssef, S., 2016. Impact of chemical alteration on the poromechanical properties of carbonate rocks. *Geophysical Prospecting*, *64*(4), pp.810-827.

Benson, S.M. and Cole, D.R., 2008. CO2 sequestration in deep sedimentary formations. *Elements*, *4*(5), pp.325-331.

Bergsaker, A.S., Røyne, A., Ougier-Simonin, A., Aubry, J. and Renard, F., 2016. The effect of fluid composition, salinity, and acidity on subcritical crack growth in calcite crystals. *Journal of Geophysical Research: Solid Earth*, *121*(3), pp.1631-1651.

Boozer, G.D., Hiller, K.H. and Serdengecti, S., 1963. Effects of pore fluids on the deformation behavior of rocks subjected to triaxial compression. *Proc. Fifth Sympos. Rock Mechanics. Univ. Minnesota*.

Brace, W.F., Paulding, B.W. and Scholz, C.H., 1966. Dilatancy in the fracture of crystalline rocks. *Journal of Geophysical Research*, *71*(16), pp.3939-3953.

Brantley, S.L., 2003. Reaction kinetics of primary rock-forming minerals under ambient conditions. *Treatise on geochemistry*, *5*, p.605.

Brantut, N., Heap, M.J., Baud, P. and Meredith, P.G., 2014a. Mechanisms of time-dependent deformation in porous limestone. *Journal of Geophysical Research: Solid Earth*, *119*(7), pp.5444-5463.

Brantut, N., Heap, M.J., Baud, P. and Meredith, P.G., 2014b. Rate-and strain-dependent brittle deformation of rocks. *Journal of Geophysical Research: Solid Earth*, *119*(3), pp.1818-1836.

Brantut, N., Heap, M.J., Meredith, P.G. and Baud, P., 2013. Time-dependent cracking and brittle creep in crustal rocks: A review. *Journal of Structural Geology*, *52*, pp.17-43.

Bruno, M.S., 1992. Subsidence-induced well failure. *SPE Drilling Engineering*, *7*(02), pp.148-152.

Burkhard, M., 1993. Calcite twins, their geometry, appearance and significance as stress-strain markers and indicators of tectonic regime: a review. *Journal of structural geology*, *15*(3-5), pp.351-368.

Byerlee, J.D., 1968. Brittle-ductile transition in rocks. *Journal of Geophysical Research*, *73*(14), pp.4741-4750.

Carpenter, B.M., Collettini, C., Viti, C. and Cavallo, A., 2016. The influence of normal stress and sliding velocity on the frictional behaviour of calcite at room temperature: insights from laboratory experiments and microstructural observations. *Geophysical Journal International*, *205*(1), pp.548-561.

Carter, N.L., Kronenberg, A.K., Ross, J.V. and Wiltschko, D.V., 1990. Control of fluids on deformation of rocks. *Geological Society, London, Special Publications*, *54*(1), pp.1-13.

Churcher, P.L., French, P.R., Shaw, J.C. and Schramm, L.L., 1991, January. Rock properties of Berea sandstone, Baker dolomite, and Indiana limestone. In *SPE International Symposium on Oilfield Chemistry*. Society of Petroleum Engineers.

Croizé, D., Renard, F., Bjørlykke, K. and Dysthe, D.K., 2010. Experimental calcite dissolution under stress: Evolution of grain contact microstructure during pressure solution creep. *Journal of Geophysical Research: Solid Earth*, *115*(B9).

Croize, D., Renard, F. and Gratier, J.P., 2013. Compaction and porosity reduction in carbonates: A review of observations, theory, and experiments. *Advances in Geophysics*, *54*, pp.181-238.

Dautriat, J., Gland, N., Dimanov, A. and Raphanel, J., 2011. Hydromechanical behavior of heterogeneous carbonate rock under proportional triaxial loadings. *Journal of Geophysical Research: Solid Earth*, *116*(B1).

Dautriat, J., Gland, N.F., Youssef, S., Rosenberg, E., Bekri, S. and Vizika-kavvadias, O., 2009. Stress-dependent directional permeabilities of two analog reservoir rocks: a prospective study on contribution of µ-tomography and pore network models. *SPE Reservoir Evaluation & Engineering*, *12*(02), pp.297-310.

David, C., Dautriat, J., Sarout, J., Delle Piane, C., Menéndez, B., Macault, R. and Bertauld, D., 2015. Mechanical instability induced by water weakening in laboratory fluid injection tests. *Journal of Geophysical Research: Solid Earth*, *120*(6), pp.4171-4188.

David, C., Menendez, B. and Bernabe, Y., 1998. The mechanical behaviour of synthetic sandstone with varying brittle cement content. *International Journal of Rock Mechanics and Mining Sciences*, *35*(6), pp.759-770.

De Waal, J.A. and Smits, R.M.M., 1988. Prediction of reservoir compaction and surface subsidence: Field application of a new model. *SPE Formation Evaluation*, *3*(02), pp.347-356.

Donath, F.A. and Fruth Jr, L.S., 1971. Dependence of strain-rate effects on deformation mechanism and rock type. *The Journal of Geology*, *79*(3), pp.347-371.

Duda, M. and Renner, J., 2013. The weakening effect of water on the brittle failure strength of sandstone. *Geophysical Journal International*, *192*(3), pp.1091-1108.

Dunning, J., Douglas, B., Miller, M. and McDonald, S., 1994. The role of the chemical environment in frictional deformation: stress corrosion cracking and comminution. *Pure and Applied Geophysics*, *143*(1), pp.151-178.

Ehrenberg, S.N. and Nadeau, P.H., 2005. Sandstone vs. carbonate petroleum reservoirs: A global perspective on porosity-depth and porosity-permeability relationships. *AAPG bulletin*, *89*(4), pp.435-445.

Evans, B., Fredrich, J.T. and Wong, T.F., 1990. The brittle-ductile transition in rocks: Recent experimental and theoretical progress. *The brittle-ductile transition in rocks*, pp.1-20.

Fabre, D. and Gustkiewicz, J., 1997. Poroelastic properties of limestones and sandstones under hydrostatic conditions. *International Journal of Rock Mechanics and Mining Sciences*, *34*(1), pp.127-134.

Ferrill, D.A., Morris, A.P., Evans, M.A., Burkhard, M., Groshong, R.H. and Onasch, C.M., 2004. Calcite twin morphology: a low-temperature deformation geothermometer. *Journal of Structural Geology*, 26(8), pp.1521-1529.

Folk, R.L., 1959. Practical petrographic classification of limestones. *AAPG Bulletin*, *43*(1), pp.1-38.

Fredrich, J.T., Arguello, J.G., Deitrick, G.L. and De Rouffignac, E.P., 2000. Geomechanical modeling of reservoir compaction, surface subsidence, and casing damage at the Belridge diatomite field. *SPE Reservoir Evaluation & Engineering*, *3*(04), pp.348-359.

Fredrich, J.T., Evans, B. and Wong, T.F., 1989. Micromechanics of the brittle to plastic transition in Carrara marble. *Journal of Geophysical Research: Solid Earth*, *94*(B4), pp.4129-4145.

Garrels, R.M. and Christ, C.L., 1965. Solutions, minerals, and equilibria.

Głowacki, A. and Selvadurai, A.P.S., 2016. Stress-induced permeability changes in Indiana limestone. *Engineering Geology*, *215*, pp.122-130.

Goldscheider, N., Mádl-Szőnyi, J., Erőss, A. and Schill, E., 2010. Review: thermal water resources in carbonate rock aquifers. *Hydrogeology Journal*, *18*(6), pp.13031318.

Grgic, D., 2011. Influence of CO2 on the long-term chemomechanical behavior of an oolitic limestone. *Journal of Geophysical Research: Solid Earth*, *116*(B7).

Grgic, D. and Giraud, A., 2014. The influence of different fluids on the static fatigue of a porous rock: Poro-mechanical coupling versus chemical effects. *Mechanics of Materials*, *71*, pp.34-51.

Griggs, D., 1967. Hydrolytic weakening of quartz and other silicates. *Geophysical Journal International*, *14*(1-4), pp.19-31.

Guéguen, Y. and Boutéca, M. eds., 2004. *Mechanics of fluid-saturated rocks* (Vol. 89). Academic Press.

Guilbot, J. and Smith, B., 2002. 4-D constrained depth conversion for reservoir compaction estimation: Application to Ekofisk Field. *The Leading Edge*, *21*(3), pp.302-308.

Hamilton, E.L., 1976. Variations of density and porosity with depth in deep-sea sediments. *Journal of Sedimentary Research*, *46*(2).

Han, R., Shimamoto, T., Ando, J.I. and Ree, J.H., 2007. Seismic slip record in carbonate-bearing fault zones: An insight from high-velocity friction experiments on siderite gouge. *Geology*, *35*(12), pp.1131-1134.

Handbook, I.L., 1998. Indiana Limestone Institute of America. *Inc., Bedford, IN*, pp.16-18.

Hanor, J.S., 1994. Origin of saline fluids in sedimentary basins. *Geological Society, London, Special Publications*, *78*(1), pp.151-174.

Heard, H.C., 1960. Transition from brittle fracture to ductile flow in Solenhofen limestone as a function of temperature, confining pressure, and interstitial fluid pressure. *Geological Society of America Memoirs*, *79*, pp.193-226.

Hellmann, R., Renders, P.J., Gratier, J.P. and Guiguet, R., 2002. Experimental pressure solution compaction of chalk in aqueous solutions Part 1. Deformation behavior and chemistry.

Henry, J.P., Paquet, J. and Tancrez, J.P., 1977, March. Experimental study of crack propagation in calcite rocks. In *International Journal of Rock Mechanics and Mining Sciences & Geomechanics Abstracts* (Vol. 14, No. 2, pp. 85-91). Pergamon.

Hirth, G. and Tullis, J., 1994. The brittle-plastic transition in experimentally deformed quartz aggregates. *Journal of Geophysical Research: Solid Earth*, *99*(B6), pp.11731-11747.

Hirth, G. and Tullis, J., 1989. The effects of pressure and porosity on the micromechanics of the brittle-ductile transition in quartzite. *Journal of Geophysical Research: Solid Earth*, *94*(B12), pp.17825-17838.

Homand, S. and Shao, J.F., 2000. Mechanical behaviour of a porous chalk and effect of saturating fluid. *Mechanics of Cohesive-frictional Materials*, *5*(7), pp.583-606.

Hugman III, R.H.H. and Friedman, M., 1979. Effects of texture and composition on mechanical behavior of experimentally deformed carbonate rocks. *AAPG Bulletin*, *63*(9), pp.1478-1489.

Hulea, I.N. and Nicholls, C.A., 2012. Carbonate rock characterization and modeling: Capillary pressure and permeability in multimodal rocks—A look beyond sample specific heterogeneity. *AAPG bulletin*, *96*(9), pp.1627-1642.

Jaeger, J.C., 1960. Shear failure of anisotropic rocks. *Geological Magazine*, *97*(01), pp.65-72.

Ji, Y., Baud, P., Vajdova, V. and Wong, T.F., 2012. Characterization of pore geometry of Indiana limestone in relation to mechanical compaction. *Oil & Gas Science and Technology–Revue d'IFP Energies nouvelles*, *67*(5), pp.753-775.

Kemeny, J.M., 1991, November. A model for non-linear rock deformation under compression due to sub-critical crack growth. In *International journal of rock mechanics and mining sciences & geomechanics abstracts* (Vol. 28, No. 6, pp. 459-467). Pergamon.

Kranz, R.L., 1983. Microcracks in rocks: a review. *Tectonophysics*, *100*(1-3), pp.449-480.

Korsnes, R.I., Madland, M.V., Vorland, K.A.N., Hildebrand-Habel, T., Kristiansen, T.G. and Hiorth, A., 2008, October. Enhanced chemical weakening of chalk due to injection of CO2 enriched water. In *International Symposium of the Society of Core Analysts, Abu Dhabi, United Arab Emirates* (Vol. 29).

Lajtai, E.Z., Duncan, E.S. and Carter, B.J., 1991. The effect of strain rate on rock strength. *Rock Mechanics and Rock Engineering*, *24*(2), pp.99-109.

LaMoreaux, P.E., Wilson, B.M. and Memon, B.A., 1984. *Guide to the hydrology of carbonate rocks*. Unesco.

Lehner, F.K., 1995. A model for intergranular pressure solution in open systems. *Tectonophysics*, *245*(3), pp.153-170.

Le Guen, Y., Renard, F., Hellmann, R., Brosse, E., Collombet, M., Tisserand, D. and Gratier, J.P., 2007. Enhanced deformation of limestone and sandstone in the presence of high fluids. *Journal of Geophysical Research: Solid Earth*, *112*(B5).

Lisabeth, H.P. and Zhu, W., 2015. Effect of temperature and pore fluid on the strength of porous limestone. *Journal of Geophysical Research: Solid Earth*, *120*(9), pp.6191-6208.

Liteanu, E., Spiers, C.J. and De Bresser, J.H.P., 2013. The influence of water and supercritical CO 2 on the failure behavior of chalk. *Tectonophysics*, *599*, pp.157-169.

Liteanu, E., Niemeijer, A., Spiers, C.J., Peach, C.J. and Bresser, J.H.P., 2012. The effect of CO_2 on creep of wet calcite aggregates. *Journal of Geophysical Research: Solid Earth*, *117*(B3).

Logan, W.N., Cumings, E.R., Malott, C.A., Visher, S.S., Tucker, W.M. and Reeves, J.R., 1922. *Handbook of Indiana geology* (No. 21). Wm. B. Burford, contractor for state printing and binding.

Lønøy, A., 2006. Making sense of carbonate pore systems. *AAPG bulletin*, 90(9), pp.1381-1405.

Majer, E.L., Baria, R., Stark, M., Oates, S., Bommer, J., Smith, B. and Asanuma, H., 2007. Induced seismicity associated with enhanced geothermal systems. *Geothermics*, *36*(3), pp.185-222.

Mallet, C., Fortin, J. and Gueguen, Y., 2013, April. Crack networks in damaged glass. In *EGU General Assembly Conference Abstracts* (Vol. 15, p. 1504).

Menéndez, B., Zhu, W. and Wong, T.F., 1996. Micromechanics of brittle faulting and cataclastic flow in Berea sandstone. *Journal of structural geology*, *18*(1), pp.1-16.

Mowar, S., Zaman, M., Stearns, D.W. and Roegiers, J.C., 1996. Micro-mechanisms of pore collapse in limestone. *Journal of Petroleum Science and Engineering*, *15*(2-4), pp.221-235.

Nagel, N.B., 2001. Compaction and subsidence issues within the petroleum industry: From Wilmington to Ekofisk and beyond. *Physics and Chemistry of the Earth, Part A: Solid Earth and Geodesy*, *26*(1-2), pp.3-14.

Nicolas, A., Fortin, J., Regnet, J.B., Dimanov, A. and Guéguen, Y., 2016. Brittle and semi-brittle behaviours of a carbonate rock: influence of water and temperature. *Geophysical Journal International*, *206*(1), pp.438-456.

Orowan, E., 1944. The fatigue of glass under stress. *Nature*, *154*(3906), pp.341-343.

Parry, M. ed., 2007. *Climate change 2007: impacts, adaptation and vulnerability* (Vol. 4). Cambridge: Cambridge University Press.

Paterson, M.S. and Wong, T.F., 2005. *Experimental rock deformation-the brittle field*. Springer Science & Business Media.

Plummer, L.N. and Busenberg, E., 1982. The solubilities of calcite, aragonite and vaterite in CO2-H2O solutions between 0 and 90 C, and an evaluation of the aqueous

model for the system CaCO3-CO2-H2O. *Geochimica et cosmochimica acta*, *46*(6), pp.1011-1040.

Plummer, L.N., Wigley, T.M.L. and Parkhurst, D.L., 1978. The kinetics of calcite dissolution in CO 2-water systems at 5 degrees to 60 degrees C and 0.0 to 1.0 atm CO 2. *American Journal of Science*, *278*(2), pp.179-216.

Pokrovsky, O.S. and Schott, J., 2002. Surface chemistry and dissolution kinetics of divalent metal carbonates. *Environmental science & technology*, *36*(3), pp.426-432.

Pokrovsky, O.S., Golubev, S.V. and Schott, J., 2005. Dissolution kinetics of calcite, dolomite and magnesite at 25 C and 0 to 50 atm pCO 2. *Chemical Geology*, *217*(3), pp.239-255.

Rice, J.R., 1968, June. A path independent integral and the approximate analysis of strain concentration by notches and cracks. ASME.

Risnes, R., 2001. Deformation and yield in high porosity outcrop chalk. *Physics and Chemistry of the Earth, Part A: Solid Earth and Geodesy*, *26*(1-2), pp.53-57.

Risnes, R., Madland, M.V., Hole, M. and Kwabiah, N.K., 2005. Water weakening of chalk—Mechanical effects of water–glycol mixtures. *Journal of Petroleum Science and Engineering*, *48*(1), pp.21-36.

Roehl, P.O. and Choquette, P.W. eds., 2012. *Carbonate petroleum reservoirs*. Springer Science & Business Media.

Rowe, K.J. and Rutter, E.H., 1990. Palaeostress estimation using calcite twinning: experimental calibration and application to nature. *Journal of Structural Geology*, *12*(1), pp.1-17.

Røyne, A., Bisschop, J. and Dysthe, D.K., 2011. Experimental investigation of surface energy and subcritical crack growth in calcite. *Journal of Geophysical Research: Solid Earth*, *116*(B4).

Royden, L. and Keen, C.E., 1980. Rifting process and thermal evolution of the continental margin of eastern Canada determined from subsidence curves. *Earth and Planetary Science Letters*, *51*(2), pp.343-361.

Røyne, A., Bisschop, J. and Dysthe, D.K., 2011. Experimental investigation of surface energy and subcritical crack growth in calcite. *Journal of Geophysical Research: Solid Earth*, *116*(B4).

Rudnicki, J.W., 2004. Shear and compaction band formation on an elliptic yield cap. *Journal of Geophysical Research: Solid Earth*, 109(B3).

Rudnicki, J.W. and Rice, J.R., 1975. Conditions for the localization of deformation in pressure-sensitive dilatant materials. *Journal of the Mechanics and Physics of Solids*, *23*(6), pp.371-394.

Rutter, E.H., 1986. On the nomenclature of mode of failure transitions in rocks. *Tectonophysics*, *122*(3-4), pp.381-387.

Rutter, E.H., 1983. Pressure solution in nature, theory and experiment. *Journal of the Geological Society*, *140*(5), pp.725-740.

Rutter, E.H., 1974. The influence of temperature, strain rate and interstitial water in the experimental deformation of calcite rocks. *Tectonophysics*, *22*(3-4), pp.311-334.

Rutter, E.H., 1972, March. The effects of strain-rate changes on the strength and ductility of Solenhofen limestone at low temperatures and confining pressures. In *International Journal of Rock Mechanics and Mining Sciences & Geomechanics Abstracts* (Vol. 9, No. 2, pp. 183-189). Pergamon.

Rutter, E.H. and Elliott, D., 1976. The kinetics of rock deformation by pressure solution [and discussion]. *Philosophical Transactions of the Royal Society of London A: Mathematical, Physical and Engineering Sciences*, *283*(1312), pp.203-219.

Sammis, C.G. and Ashby, M.F., 1986. The failure of brittle porous solids under compressive stress states. *Acta Metallurgica*, *34*(3), pp.511-526.

Sayers, C. M., Van Munster, J. G., & King, M. S. (1990, October). Stress-induced ultrasonic anisotrophy in Berea sandstone. In *International Journal of Rock Mechanics and Mining Sciences & Geomechanics Abstracts* (Vol. 27, No. 5, pp. 429-436). Pergamon.

Schmoker, J. W., Halley, R. B. (1982). Carbonate porosity versus depth: a predictable relation for south Florida. AAPG Bulletin, 66(12), 2561-2570.

Shalev, E., Lyakhovsky, V., Weinstein, Y. and Ben-Avraham, Z., 2013. The thermal structure of Israel and the Dead Sea Fault. *Tectonophysics*, *602*, pp.69-77.

Simmons, G. and Richter, D., 1976. Microcracks in rocks. *The physics and chemistry of minerals and rocks*, pp.105-137.

Simpson, D.W., Leith, W.S. and Scholz, C.H., 1988. Two types of reservoir-induced seismicity. *Bulletin of the Seismological Society of America*, *78*(6), pp.2025-2040.

Sjöberg, E.L. and Rickard, D., 1983. The influence of experimental design on the rate of calcite dissolution. *Geochimica et cosmochimica acta*, *47*(12), pp.2281-2285.

Spiers, C.J., Schutjens, P.M.T.M., Brzesowsky, R.H., Peach, C.J., Liezenberg, J.L. and Zwart, H.J., 1990. Experimental determination of constitutive parameters governing creep of rocksalt by pressure solution. *Geological Society, London, Special Publications*, *54*(1), pp.215-227.

Sylte, J.E., Thomas, L.K., Rhett, D.W., Bruning, D.D. and Nagel, N.B., 1999, January. Water induced compaction in the Ekofisk field. In *SPE Annual Technical Conference and Exhibition*. Society of Petroleum Engineers.

Tada, R., Maliva, R. and Siever, R., 1987. A new mechanism for pressure solution in porous quartzose sandstone. *Geochimica et Cosmochimica Acta*, *51*(9), pp.2295-2301.

Tamarkin, T., Ougier-Simonin, A. and Zhu, W., 2012. Progressive microscopic damage associated with fault growth. *Geophysical Research Letters*, *39*(15).

Tapponnier, P. and Brace, W.F., 1976, April. Development of stress-induced microcracks in Westerly granite. In *International Journal of Rock Mechanics and Mining Sciences & Geomechanics Abstracts* (Vol. 13, No. 4, pp. 103-112). Pergamon.

Terzaghi, K.V., 1936, June. The shearing resistance of saturated soils and the angle between the planes of shear. In *Proceedings of the 1st international conference on soil mechanics and foundation engineering* (Vol. 1, pp. 54-56). Harvard University Press Cambridge, MA.

Teufel, L.W., Rhett, D.W. and Farrell, H.E., 1991, January. Effect of reservoir depletion and pore pressure drawdown on in situ stress and deformation in the Ekofisk field, North Sea. In *The 32nd US Symposium on Rock Mechanics (USRMS)*. American Rock Mechanics Association.

Turner, F.J., T Griggs, Davod and Heard, H., 1954. Experimental deformation of calcite crystals. *Geological Society of America Bulletin*, *65*(9), pp.883-934.

Underwood, E.E., 1972. The mathematical foundations of quantitative stereology. In *Stereology and Quantitative Metallography*. ASTM International.

Vajdova, V., Baud, P., Wu, L. and Wong, T.F., 2012. Micromechanics of inelastic compaction in two allochemical limestones. *Journal of Structural Geology*, *43*, pp.100-117.

Vajdova, V., Baud, P. and Wong, T.F., 2004. Compaction, dilatancy, and failure in porous carbonate rocks. *Journal of Geophysical Research: Solid Earth*, *109*(B5).

Vajdova, V., Zhu, W., Chen, T.M.N. and Wong, T.F., 2010. Micromechanics of brittle faulting and cataclastic flow in Tavel limestone. *Journal of Structural Geology*, *32*(8), pp.1158-1169.

Wanless, H.R., 1979. Limestone response to stress: pressure solution and dolomitization. *Journal of Sedimentary Research*, *49*(2).

Wawersik, W.R. and Brace, W.F., 1971. Post-failure behavior of a granite and diabase. *Rock mechanics*, *3*(2), pp.61-85.

Wawersik, W.R. and Fairhurst, C., 1970, September. A study of brittle rock fracture in laboratory compression experiments. In *International Journal of Rock Mechanics and Mining Sciences & Geomechanics Abstracts* (Vol. 7, No. 5, pp. 561IN7565-564IN14575). Pergamon.

Weyl, P.K., 1959. Pressure solution and the force of crystallization: a phenomenological theory. *Journal of geophysical research*, *64*(11), pp.2001-2025.

Wintsch, R.P., Christoffersen, R. and Kronenberg, A.K., 1995. Fluid-rock reaction weakening of fault zones. *Journal of Geophysical Research: Solid Earth*, *100*(B7), pp.13021-13032.

Wong, T.F., 2000. Failure mode and weakening effect of water on sandstone. *Journal of geophysical research*, *105*(B7), pp.16371-16389.

Wong, T.F., 1992. Brittle-ductile transition in porous rocks: phenomenological and micromechanical models. In *International geological congress*.

Wong, T.F., 1985. Geometric probability approach to the characterization and analysis of microcracking in rocks. *Mechanics of Materials*, *4*(3-4), pp.261-276.

Wong, T.F. and Baud, P., 2012. The brittle-ductile transition in porous rock: A review. *Journal of Structural Geology*, *44*, pp.25-53.

Wong, T.F. and Baud, P., 1999. Mechanical compaction of porous sandstone. *Oil & Gas Science and Technology*, *54*(6), pp.715-727.

Wong, T.F., David, C. and Zhu, W., 1997. The transition from brittle faulting to cataclastic flow in porous sandstones: Mechanical deformation. *Journal of Geophysical Research: Solid Earth*, *102*(B2), pp.3009-3025.

Wong, T.F. and Wu, L.C., 1995. Tensile stress concentration and compressive failure in cemented granular material. *Geophysical Research Letters*, *22*(13), pp.1649-1652.

Wong, T.F., Szeto, H. and Zhang, J., 1992. Effect of loading path and porosity on the failure mode of porous rocks. *Appl. Mech. Rev*, *45*(8), pp.281-293.

Wu, X.Y., Baud, P. and Wong, T.F., 2000. Micromechanics of compressive failure and spatial evolution of anisotropic damage in Darley Dale sandstone. *International Journal of Rock Mechanics and Mining Sciences*, *37*(1), pp.143-160.

Yale, D.P. and Crawford, B., 1998, January. Plasticity and permeability in carbonates: dependence on stress path and porosity. In *SPE/ISRM Rock Mechanics in Petroleum Engineering*. Society of Petroleum Engineers.

Yin, H. and Dvorkin, J., 1994. Strength of cemented grains. *Geophysical Research Letters*, *21*(10), pp.903-906.

Zhang, X., Spiers, C.J. and Peach, C.J., 2010. Compaction creep of wet granular calcite by pressure solution at 28 C to 150 C. *Journal of Geophysical Research: Solid Earth*, *115*(B9).

Zheng, Z., Cook, N.G. and Myer, L.R., 1989, January. Stress induced microcrack geometry at failure in unconfined and confined axial compressive tests. In *The 30th US Symposium on Rock Mechanics (USRMS)*. American Rock Mechanics Association.

Zhang, X., Spiers, C.J. and Peach, C.J., 2010. Compaction creep of wet granular calcite by pressure solution at 28 C to 150 C. *Journal of Geophysical Research: Solid Earth*, *115*(B9).

Zhang, X. and Spiers, C.J., 2005. Compaction of granular calcite by pressure solution at room temperature and effects of pore fluid chemistry. *International Journal of Rock Mechanics and Mining Sciences*, *42*(7), pp.950-960.

Zhang, J., Wong, T.F. and Davis, D.M., 1990. Micromechanics of pressure-induced grain crushing in porous rocks. *Journal of Geophysical Research: Solid Earth*, *95*(B1), pp.341-352.

Zhu, W., Baud, P. and Wong, T.F., 2010. Micromechanics of cataclastic pore collapse in limestone. *Journal of Geophysical Research: Solid Earth*, *115*(B4).

Zhu, W. and Wong, T.F., 1997. The transition from brittle faulting to cataclastic flow: Permeability evolution. *Journal of Geophysical Research: Solid Earth*, *102*(B2), pp.3027-3041.

Zhu, W., Xiao, X. and Evans, B., 2006, December. The brittle-ductile transition in fine-grained carbonate rocks: Effect of water. In *AGU Fall Meeting Abstracts*.